OPTICAL PROPERTIES OF Si-Ge SUPERLATTICES AND WIDE BAND GAP II-VI SUPERLATTICES

Thesis by

Yasantha Nirmal Rajakarunanayake

In Partial Fulfillment of the Requirements
for the Degree of
Doctor of Philosophy

California Institute of Technology
Pasadena, California

1991

(Submitted June 12, 1990)

to my parents

Acknowledgements

First and foremost, I gratefully acknowledge my advisor Dr. T. C. McGill for providing me with unique opportunities for research and professional development. I have greatly benefited from his guidance and encouragement in academic matters, and profited from his mature advice concerning personal development. I am especially thankful to Dr. J. O. McCaldin for sharing his valuable experience in experimental physics with me, and for offering me sound advice during our interactions.

I thank Dr. Richard Miles, Dr. Matthew Johnson, Dr. Bob Hauenstein, Mike Jackson, Todd Rossi, Mark Phillips and Pete Zampardi for offering me help and expertise on several experimental issues. I am also thankful to Dr. George Wu, Dr. Alice Bonnefoi, Dr. Dave Ting, and Ed Yu for helping me on many theoretical issues. I thank Mike Jackson for showing great patience in explaining several experimental procedures to me. I have benefited a great deal from his knowledge. I enjoyed collaborating with Mark Phillips and Brian Cole on the II-VI projects. I am indebted to Ed Yu for his generous effort in carefully proofreading several of my papers and sections of this thesis. It has been a pleasure to interact with Dr. David Chow, Dr. Ted Woodward, Jan Soderstrom, Doug Collins, Ed Croke, Yixin Liu, Dr. Wesley Boudville, Ron Marquardt, Johanes Swenberg, Harold Levy, Rob Miles and Mike Wang. I will miss many of the stimulating conversations about physics and other topics I had with many of the McGill group members. I owe a special thanks to Marcia Hudson, Carol McCollum, and Vere Snell, who provided excellent administrative support during my stay in the McGill group.

It is a delight to acknowledge my friends Katherine Widdowson, John Miller, and Kathleen Kramer. Finally, I would like to thank my parents for providing me with love, encouragement, and support throughout my education.

Abstract

This thesis presents the investigation of semiconductor heterostructures for optoelectronic applications, with particular emphasis on band alignment considerations, strain effects, band structure calculations and characterization by optical spectroscopy. The purpose of the work described here is two-fold. The first part of this thesis is concerned with the study of novel optoelectronic properties exhibited by Si/Ge superlattices both in the near infrared (interband transitions) and far infrared (intersubband transitions) energy ranges. The second part of this thesis is concerned with establishing the merits of II-VI semiconductor heterostructures for producing visible light emitters, and investigating techniques to improve the dopability of II-VI semiconductors.

In the first part of this thesis we investigate the merits of Si/Ge superlattices for optical applications. Although Si and Ge are indirect band gap materials, Si/Ge superlattices can exhibit a direct band gap for certain layer thickness combinations. In Chapter 2, we show that the optical absorption/emission strengths for interband transitions in Si/Ge superlattices can be enhanced by six orders of magnitude over pure Si or Ge. However, these numbers are still three to four orders of magnitude lower than the optical absorption/emission strengths of direct band gap materials such as GaAs. These results are based on a full zone $\vec{k} \cdot \vec{p}$ formalism that we developed specifically to study the band structure of Si/Ge superlattices. In Chapter 3, we investigate the intersubband absorption coefficients in doped Si/Ge superlattices. Intersubband transitions in these superlattices make them interesting candidates for long-wavelength infrared detectors. Such infrared detectors are analogous to extrinsic Si detectors, with the additional advantage of tunability of the peak absorption wavelength. The intersubband absorption strengths of Si/Ge superlattices reported in this thesis are comparable to those for $Al_xGa_{1-x}As$/GaAs superlattices, with the additional benefits of the ability to detect normally incident light, and compatibility with the fabrication and processing technology of Si electronics.

In the second part of this thesis, we describe investigations of II-VI semiconductor heterostructures for visible light emitter applications. The wide band gap II-VI semiconductors are ideally suited for visible optoelectronics by virtue of their direct band gaps in the blue/green region of the spectrum. However, difficulties associated with doping these materials have severely limited their applications. Low-temperature, epitaxial-growth techniques such as molecular beam epitaxy have opened up new approaches for II-VI materials that show potential for overcoming some of these problems. In Chapter 4, we investigate minority carrier injection in II-VI semiconductors using heterojunctions. We also perform band structure calculations on II-VI strained layer superlattices to investigate the role of strain on the heterojunction band alignments. We experimentally determine the band offsets for CdTe/ZnTe and ZnSe/ZnTe heterojunctions using optical techniques, and remark on the merits of these heterojunctions for carrier injection. We theoretically extended our conclusions to II-VI quaternary alloys and show that there is great promise for visible light-emitter applications within quaternary heterostructures. In Chapter 5, we analyze the role of external electric fields applied during growth in suppressing self-compensation in II-VI semiconductors. This is a novel approach to achieve and control metastability in semiconductors. Our results indicate that II-VI doping efficiencies can be dramatically improved if substantial electric fields are applied during growth.

Parts of this thesis have been or will be published under the following titles:

Part I:

Band structure and optical properties of Si-$Si_{1-x}Ge_x$ superlattices

Y. Rajakarunanayake and T. C. McGill, *Phys. Rev. B.* **40**, 3054 (1989).

Strain effects and optical properties of $Si_{1-x}Ge_x$/Si superlattices

Y. Rajakarunanayake and T. C. McGill, *J. Vac. Sci. Technol.* **B7**, 799 (1989).

Intersubband absorption in n-type Si/Ge superlattices for long wavelength infrared detectors

Y. Rajakarunanayake and T. C. McGill, *J. Vac. Sci. Technol.* **B8**, to be published (1990).

Si/Ge n-type resonant tunnel structures

Y. Rajakarunanayake and T. C. McGill, *Appl. Phys. Lett* **55**, 1537 (1989).

Part II:

Application of electric fields during MBE growth to suppress self-compensation in semiconductors

Y. Rajakarunanayake, J. O. McCaldin, and T. C. McGill, *J. Cryst. Growth* , to be published (1990).

The role of electric fields in suppressing self-compensation

Y. Rajakarunanayake, J. O. McCaldin, and T. C. McGill, *J. Appl. Phys.* , to be published (1990).

Optical investigation of the band offset of $ZnTe_{1-x}Se_x$-ZnTe and $Zn_{1-x}Cd_xTe$-ZnTe superlattices

Y. Rajakarunanayake, M. C. Phillips, J. O. McCaldin, D. H. Chow, D. A. Collins, and T. C. McGill, *Mat. Res. Soc. Proc.* , accepted for publication, April (1990).

MBE growth and characterization of ZnTe and $ZnTe_{1-x}Se_x$-ZnTe superlattices

M. C. Phillips, Y. Rajakarunanayake, J. O. McCaldin, D. H. Chow, D. A. Collins, and T. C. McGill, *Mat. Res. Soc. Proc.* , accepted for publication, April (1990).

Band alignment in $ZnTe_{1-x}Se_x$-ZnTe and $Zn_{1-x}Cd_xTe$-ZnTe strained layer superlattices

Y. Rajakarunanayake, M. C. Phillips, J. O. McCaldin, D. H. Chow, D. A. Collins, and T. C. McGill, *Proc. SPIE* , accepted for publication, March (1990).

Growth of ZnTe and $ZnTe_{1-x}Se_x$ epilayers and superlattices

M. C. Phillips, Y. Rajakarunanayake, J. O. McCaldin, D. H. Chow, J. R. Soderstrom, D. A. Collins, and T. C. McGill, *Proc. SPIE* , accepted for publication, March (1990).

Growth and characterization of ZnTe, $ZnTe_{1-x}Se_x$-ZnTe epilayers, and $ZnTe_{1-x}Se_x$-ZnTe superlattices on GaSb substrates

M. C. Phillips, Y. Rajakarunanayake, J. O. McCaldin, D. H. Chow, D. A. Collins, J. R. Soderstrom, and T. C. McGill, *Bull. Am. Phys. Soc.* **35**, 636 (1990).

Growth and characterization of ZnTe films grown on GaAs, InAs, GaSb, and ZnTe

Y. Rajakarunanayake, B. H. Cole, J. O. McCaldin, D. H. Chow, J. R. Soderstrom, and T. C. McGill, *Appl. Phys. Lett.* **55**, 1217 (1989).

II-VI Heterostructures and multi-quantum wells

T. C. McGill, R. H. Miles, Y. Rajakarunanayake and J. O. McCaldin , in *Proceedings of the NATO advanced research workshop on growth and optical properties of wide gap II-VI semiconductors*, 53 (1988).

Band structure of ZnSe-ZnTe superlattice calculated by k.p theory

Y. Rajakarunanayake, R. H. Miles, G. Y. Wu, and T. C. McGill, *Proc. SPIE* **943**, 198 (1988).

Band offset of the ZnSe-ZnTe superlattices: A fit to photoluminescence data by k.p theory

Y. Rajakarunanayake, R. H. Miles, G. Y. Wu, and T. C. McGill, *J. Vac. Sci. Technol. B* **6**, 1354 (1988).

Band structure of ZnSe-ZnTe superlattices

Y. Rajakarunanayake, R. H. Miles, G. Y. Wu, and T. C. McGill, *Phys. Rev. B* **37**, 10212 (1988).

Contents

List of Figures

List of Tables

Chapter 1

Introduction

This thesis presents investigations of semiconductor heterostructures and superlattices for novel optoelectronic applications. Recent advances in semiconductor growth capabilities[1] have provided the ability to fabricate semiconductor heterostructures with small length scales ($< 100\,\text{Å}$). To the semiconductor device physicist, the ability to fabricate structures at small length scales provides a means to manipulate the quantum mechanical phenomena that exist at these length scales and utilize them in designs of future electronic and optoelectronic applications. Superlattices are classic examples of such manmade semiconductor structures that exhibit quantum effects, and have been widely used in device applications since they were first proposed in 1970.[2]

Superlattices based on nearly lattice-matched pairs of semiconductors such as GaAs/AlAs,[3] GaSb/InAs,[4] and HgTe/CdTe[5] have received the most attention during the early development in the 1970s. However, recent progress in crystal growth techniques such as molecular beam epitaxy (MBE), and metal-organic chemical vapor deposition (MOCVD) have opened up interesting possibilities for lattice-mismatched heteroepitaxy. The object of this thesis is the study of two interesting cases of lattice-mismatched semiconductor superlattices; the first case is Si/Ge superlattices, and the second case is wide band gap II-VI superlattices. Since the successful growth of these structures has been a quite recent development, much theoretical and experimental work needs to be done to further our understanding of these novel semiconductor materials.

1.1 Overview of Thesis

The work presented in this thesis falls under two major parts. The first part is the investigation of approaches to improve the optical properties of Si/Ge structures for infrared applications. The second part is the investigation of approaches to improve the electrical and optical properties of wide band gap II-VI semiconductor structures for blue/green light-emitter applications.

1.1.1 Si/Ge Structures

The first part of this thesis is devoted to reassessing the possibilities for optoelectronic applications based on silicon, given the possibility of fabricating Si/Ge superlattices. We investigate the merits of interband transitions in Si/Ge superlattices for near infrared applications, and intersubband transitions in Si/Ge superlattices for far infrared applications.

Optoelectronics in the near infrared 1.3-1.6 μm wavelength region is important because of the compatibility with the minimum loss band of fiber optic communication lines. It is possible to fabricate Si/Ge superlattices with band gaps in this wavelength region, making them very attractive for optoelectronic applications, provided that substantial optical matrix elements can be obtained. We show the intriguing possibility that Si/Ge superlattices can exhibit direct band gap behavior for certain layer thickness combinations, although Si and Ge are indirect band gap materials. We survey the optical absorption and emission strengths of Si/Ge superlattices, and evaluate their potential for optoelectronic applications. On the other hand, infrared detectors at 10μm and longer wavelengths are important for atmospheric and space-monitoring applications. We show that conduction bands of Si/Ge superlattices, grown along certain orientations, show interesting intersubband absorption properties that can be potentially useful for long-wavelength infrared detection. We investigate the intersubband transitions in Si/Ge superlattices and evaluate their merits for long-wavelength infrared detector applications.

1.1.2 Wide-Gap II-VI Structures

The second part of this thesis is devoted to reassessing the possibilities for blue/green semiconductor light-emitters employing wide band gap II-VI heterostructures and superlattices. The wide-gap II-VI materials are ideal candidates for producing blue/green light-emitters by virtue of their direct band gaps. However, difficulties associated with obtaining selective doping in both n- and p-type have limited the usefulness of these materials in semiconductor devices. In this thesis we have attempted to attack this difficult problem by two approaches.

The first is the heterojunction approach, where we have investigated the prospects for minority carrier injection in wide band gap II-VI p-n heterojunctions. We have investigated the band alignments between various II-VI wide band gap semiconductors by optical spectroscopy, in an attempt to determine the usefulness of these heterojunctions for minority carrier injection. We have used our analysis of ZnSe, ZnTe and CdTe band alignments to investigate the possibilities of carrier injection throughout the whole alloy composition range of $ZnTe_{1-x}Se_x$ and $Zn_{1-x}Cd_xTe$ ternaries. We also extend our analysis to several wide-gap II-VI quaternaries where opportunities may exist for wide band gaps in the blue/green region of the spectrum, and possibilities for efficient minority carrier injection, with the additional benefits of improved lattice-match. The second approach we consider for controlling the electrical properties of II-VI materials is the application of external electric fields to modify the thermodynamic equilibrium of self-compensation, and kinetically block the process of compensation. As a particular example, we theoretically analyze the influence of electric fields in suppressing self-compensation processes during crystal growth. We expect that such techniques for accessing and controlling thermodynamically metastable material regimes could enhance the opportunities for semiconductor applications in the future.

1.1.3 Outline of Chapter

The purpose of this chapter is to provide a broad introduction to the thesis, and an overview of the work presented in the following chapters. Section 1.2 is a summary of the major results obtained in this thesis. In Section 1.3, we provide the background and motivation for studying the optical properties of Si/Ge and II-VI structures. Sections 1.4, and 1.5 provide the general background on superlattices and strain effects, and develop important issues addressed throughout this thesis. In Section 1.6 important theoretical issues encountered in band structure calculations are reviewed. Section 1.7 concludes the chapter with an outline of the thesis.

1.2 Summary of Results

This section provides a chapter-by-chapter summary of the main results obtained in our investigations of the optical properties of Si/Ge superlattices and wide band gap II-VI semiconductors.

1.2.1 Interband Transitions in Si/Ge Superlattices

In Chapter 2 we investigate the band alignment, strain effects and optical matrix elements of $Si_{1-x}Ge_x$/Si superlattices. We demonstrate that quasi-direct band gap $Si_{1-x}Ge_x$/Si superlattices can be obtained by suitable choices of layer thicknesses. We calculate strain dependent conduction band offsets of coherently strained $Si_{1-x}Ge_x$ epilayers, as functions of the substrate alloy concentration, and of the epilayer alloy concentration. Optical matrix elements are computed as a function of the barrier and well layer thicknesses, for $Si_{1-x}Ge_x$/Si superlattices with favorable strain distributions. We find that optical absorption and emission strengths can vary by 3-4 orders of magnitude for layer thickness variations as small as 1-2 monolayers, suggesting that layer thicknesses must be controlled to within one monolayer accuracy to obtain enhanced optical absorption/emission properties. Typical optical matrix elements calculated for these $Si_{1-x}Ge_x$/Si superlattices are 3-4 orders of magnitude larger than for bulk Si or Ge, but are still 3 orders of magnitude smaller than for direct band gap materials such as GaAs limiting the usefulness of $Si_{1-x}Ge_x$/Si superlattices for optoelectronic applications.[6]

1.2.2 Intersubband Transitions in Si/Ge Superlattices

In Chapter 3 we calculate the absorption strengths for intersubband transitions in n-type $Si_{1-x}Ge_x$/Si superlattices. These structures can be used for the detection of long-wavelength infrared radiation in a manner analogous to extrinsic silicon detectors. Peak absorption strengths that we calculate for $Si_{1-x}Ge_x$/Si superlattices are 2000-6000 cm^{-1} for typical sheet-doping concentrations ($\approx 10^{12}$ cm^{-2}). To achieve intersubband absorption in $Al_xGa_{1-x}As$/GaAs superlattice detectors, the incident light must have a polarization component perpendicular to the plane of the superlattice layers. This limitation can be overcome by having $Si_{1-x}Ge_x$/Si superlattice infrared detectors grown on [111], and [110] oriented substrates.[7, 8] We present detailed results of the absorption coefficient, and the peak absorption wavelength of [100], [111] and [110] $Si_{1-x}Ge_x$/Si superlattices. Absorption comparable to $Al_xGa_{1-x}As$/GaAs superlattice detectors,[9] and compatibility with existing Si technology, with the additional benefits of the ability to detect normally incident light make these devices promising for future applications.[10]

1.2.3 Band Alignment of Wide Band Gap II-VI Heterostructures

Chapter 4 of this thesis is concerned with the determination of the band alignment between ZnTe, ZnSe and CdTe. We present photoluminescence spectra from $Zn_{1-x}Cd_xTe$-ZnTe and $ZnTe_{1-x}Se_x$-ZnTe superlattices grown by MBE, and analyze the band alignments and strain effects. Our results are based on fitting the dominant photoluminescence peaks to the superlattice band structure obtained by $\vec{k} \cdot \vec{p}$ theory. We have applied an 8-band $\vec{k} \cdot \vec{p}$ model to systematically treat the changes in the band structure that are due to strain effects, in strained-layer II-VI superlattices. We find that the valence band offset of the CdTe/ZnTe system is quite small (-50 ± 160 meV). In these superlattices, the electrons and heavy-holes are confined to the $Zn_{1-x}Cd_xTe$ layers (type I band alignment), while the light-holes are confined to the ZnTe layers (type II band alignment). On the other hand, the photoluminescence data from the $ZnTe_{1-x}Se_x$/ZnTe superlattices suggest that the band alignment between ZnSe/ZnTe is type II, with a large valence band offset (-907 ± 120 meV). We also investigate the band gap bowing in the $ZnTe_{1-x}Se_x$ alloys, and determine the components of the bowing in valence and conduction bands. Given our results for band alignments, we evaluate the prospects for minority carrier injection in wide band gap quaternary heterostructures.[11]

1.2.4 Role of Electric Fields in Suppressing Self-Compensation

In Chapter 5, we describe a technique to suppress self-compensation processes in semiconductors, by the application of external electric fields during crystal growth. We show that it is possible to adopt this technique to enhance the doping efficiency, and kinetically bury uncompensated material in non-equilibrium growth techniques such as molecular beam epitaxy (MBE). An obvious application of this technique is to improve the doping of wide band gap II-VI semiconductors, where selective doping in both n- and p-type is usually not possible to achieve because of extensive self-compensation. In our calculations, the self-compensating species are modeled as charged, mobile species that are free to drift and diffuse under electric fields. In the case of MBE growth, we solve for the equilibrium of these species in a moving coordinate frame, and show that two important dimensionless parameters determine the effectiveness of suppressing self-compensation. The first parameter that determines the doping profile is $D/\lambda v$, where D is the diffusion coefficient, λ is the Debye screening length, and v is the growth rate. The second parameter is $qE\lambda/kT$, where q is the electron charge, E is the electric field, k is the Boltzman constant, and T is the growth temperature. We have specifically applied our analysis to the n-type doping problem of ZnTe, where we have assumed the self-compensating species to be A-centers[12, 13, 14]. Our results indicate that it should be possible to achieve n-type doped ZnTe under the usual MBE growth conditions, with the application of substantial electric fields. Theoretical results are presented for doping concentrations as functions of the growth rate and the applied electric field. We expect that our analysis and the proposed electric field-assisted doping technique will play an important role in the effort to overcome self-compensation, and will achieve selective doping in wide band gap II-VI semiconductors.[15]

1.3 Background and Motivation

1.3.1 Background of Si/Ge Structures

The purpose of this section is to provide a general background of Si/Ge-based structures, and to motivate the work we present on the Si/Ge system, in the first part of this thesis.

Silicon has been the material of choice for semiconductor electronics since the 1950s. Although Si possesses only modest electron mobilities and an indirect band gap, there are many factors that have contributed to its success. Two of these factors are the excellent insulating qualities of its oxide SiO_2 which has made the planar processing technology viable, and the superior mechanical strength of silicon. Although throughout the 1960's and the 1970's the development of the Si-based devices was adequate for electronic applications, recently, alternatives have attracted a fair amount of attention.

The demand for high-speed electronics and optoelectronics has made III-V semiconductors such as GaAs, and InAs attractive alternatives to Si in the past decade. It is possible to achieve much higher carrier mobilities in the narrower band gap III-V materials than in Si, making them superior for high-speed applications; The longitudinal effective masses of InAs, GaAs, and Si are 0.023, 0.067 and 0.98, respectively. The direct band gap of GaAs is ideal for optoelectronic applications such as semiconductor lasers, while the indirect band gap Si remains a poor candidate for optoelectronics. However, much of the recent success of the III-Vs can be attributed not only to their intrinsic electronic and optical properties, but also to the heterojunction approach, and to the growth techniques such as MBE, and MOCVD.

In the early 1980s, it was argued that the application of the heterojunction approach and the growth techniques such as MBE to conventional Si-based devices could improve their characteristics. This was the major motivation for developing

Si/Ge heteroepitaxy and Si MBE in the mid 1980s.[16] The choice of Ge as the secondary material in Si heteroepitaxy was motivated by its chemical compatibility with Si, and the possibility of avoiding cross doping problems at the interfaces that occur in the case of III-V/Si heteroepitaxy. However, there is a large structural mismatch between these two materials ($\approx 4.2\%$), and this has led to interesting strain effects in Si/Ge heterostructures, while posing challenging growth issues.

Electrical Properties

Si/Ge heteroepitaxy has improved the electronic properties of Si-based devices as expected. Today, structures consisting of $Si_{1-x}Ge_x$ layers have shown considerable improvements in speed.[17, 18] Heterojunction bipolar transistors (HBTs) fabricated from coherently strained $Si_{1-x}Ge_x$ epilayers have displayed superior current gains.[17, 18] Modulation-doped, field-effect transistors (MODFETs) have also displayed improved carrier mobility with $Si_{1-x}Ge_x$ channels. These improvements in the speed and gain are related to the strain-induced splitting of the conduction band degeneracy; it is possible to split the six Δ conduction valleys of Si into two longitudinal and four transverse valleys separated in energy by the application of uniaxial stress. Thus, the effective masses can be lowered, leading to higher carrier mobility. Another important factor that can contribute to the speed of $Si_{1-x}Ge_x$ electronic devices is that strain-induced energy splitting of the conduction valleys can reduce intervalley scattering. If the strain-induced energy splitting is larger than a longitudinal optical phonon energy, then it becomes kinematically unfavorable for intervalley scattering events to occur, and this leads to superior mobility.

Optical Properties

While Si/Ge heteroepitaxy has significantly improved the electrical properties of several Si-based devices, Si/Ge superlattices have also stimulated research interest as potentially useful optical materials, as it is well-known that Si is a poor candidate for optical applications because of the indirect band gap. However, the interesting possibility of obtaining a direct band gap Si/Ge superlattice arises out of simple band-folding considerations as illustrated in Fig. 1.1. Although few researchers have claimed that intense photoluminescence could be observed from $Si_{1-x}Ge_x$ alloys, and superlattices,[19] the credibility of these claims are still under thorough investigation. It is also interesting to note that if the optical absorption of $Si_{1-x}Ge_x$ layers can be significantly improved, then it is possible to lower the band gap of $Si_{1-x}Ge_x$ alloys and superlattices into the 1.3-1.6 μm region (for compatibility with fiber optic communication lines) by strain-induced effects. It is certainly worthwhile investigating the prospects for improving the optical properties of Si by the heterojunction approach, and for surveying possibilities for optical devices based on Si/Ge.

In this thesis we have attempted the task of evaluating, theoretically the prospects of Si/Ge superlattices for optical applications. In Chapter 2 we calculate the optical matrix elements of Si/Ge superlattices. Our results indicate that it is possible to enhance the optical absorption/emission strengths by six-orders of magnitude due to zone folding effects. However, these numbers are still three-orders of magnitude less than in direct band gap materials such as GaAs. In Chapter 3, we have shown that it is possible to achieve a long-wavelength infrared detector from Si/Ge superlattices analogous to the extrinsic Si detectors, with the additional advantage of tunable wavelength response. The basic concept behind these types of infrared detectors is illustrated in Fig. 1.2. Although the aim of the work reported in the first part of this thesis was to illustrate two optical applications based on Si/Ge, we feel that Si/Ge heteroepitaxy is still in its infancy, and that there are many opportunities for future applications based on this system.

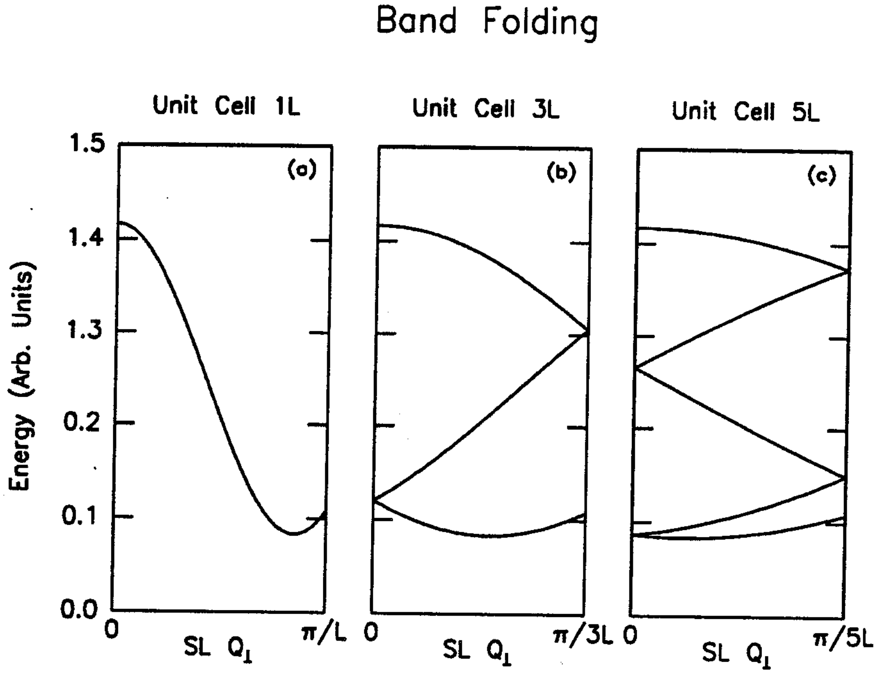

Figure 1.1: Schematic illustration of band-folding. We show the band structure of three superlattices where the unit cell sizes are 1L, 3L, and 5L, respectively. Correspondingly, the Brillouin zone edges are at $\frac{\pi}{L}$, $\frac{\pi}{3L}$, and $\frac{\pi}{5L}$. It is possible to fold the indirect minimum shown in Fig. 1.1(a) into the zone-center of the reduced Brillouin zone by a proper choice of layer thicknesses. This is the main idea behind obtaining direct band gap Si/Ge superlattices.

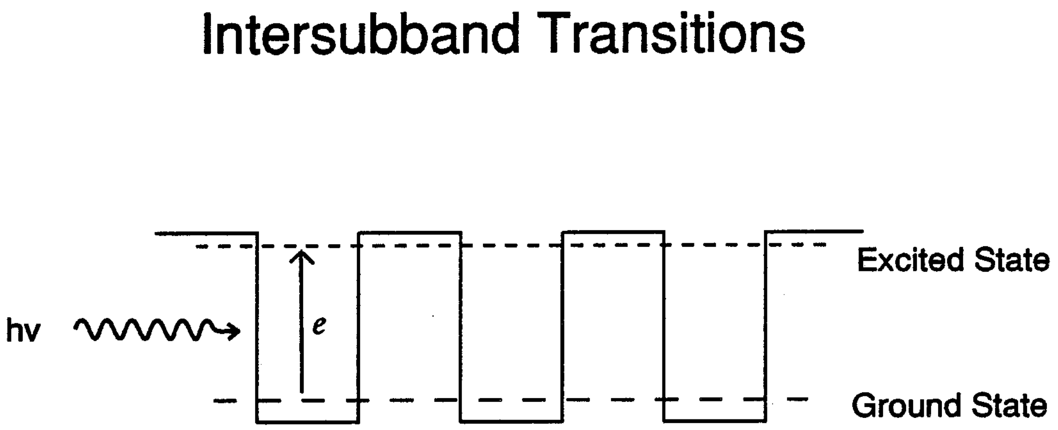

Figure 1.2: Schematic illustration of intersubband transitions in superlattices. An infrared photon can raise an electron from the ground state to an excited state that lies close in energy to the top of the barrier. The electron mobility in the higher subband is larger than in the ground state, and under a small applied bias this structure will produce an extra photo-generated current. This is the main idea behind superlattice infrared detectors.

1.3.2 Background of II-VI Structures

The purpose of this section is to provide a general background into wide band gap II-VI semiconductor structures, and motivate the work we present on these materials, in the second part of this thesis.

The II-VI semiconductors form a set of materials with band gaps in the wavelength region from far infrared (zero-band-gap HgTe), through the visible and well into the ultraviolet (ZnS with a 3.66 eV band gap). The applications of narrow band gap II-VI materials in infrared devices is well established. However, very little progress has been achieved in the wide band gap II-VI materials in terms of device applications, because of the inability to easily control their electrical properties. The purpose of this investigation is to make progress toward a blue/green semiconductor light-emitter based on the wide band gap II-VI materials. Although formally the II-VI's contain quite a large number of candidates suitable for this purpose, in this work we focus our attention on the compound semiconductors limited to Zn, Cd cations, and Te, Se anions. In Fig. 1.3, we show the band gaps of several wide-gap II-VI materials, and a plot of the human eye response, versus photon energy.

The reasons often quoted for explaining the inability to control the electrical properties of wide gap II-VI materials is two-fold. First it was suggested through the extensive work in the 1960s that self-compensation processes occur in these materials, through defect complexes[20] that have opposite charges to the incorporated dopants. It was postulated that under thermodynamic equilibrium conditions at high-temperature, these defect complexes and the original dopants were found roughly equal in number, such that the resulting material had very poor electrical properties. However, the actual degree of compensation depended on the choice of material as well as on the choice of dopant species. For instance, ZnTe could be easily doped p-type but not n-type, while ZnSe could be easily doped n-type but not p-type. Even when these materials can be successfully doped, it is hard to achieve high doping

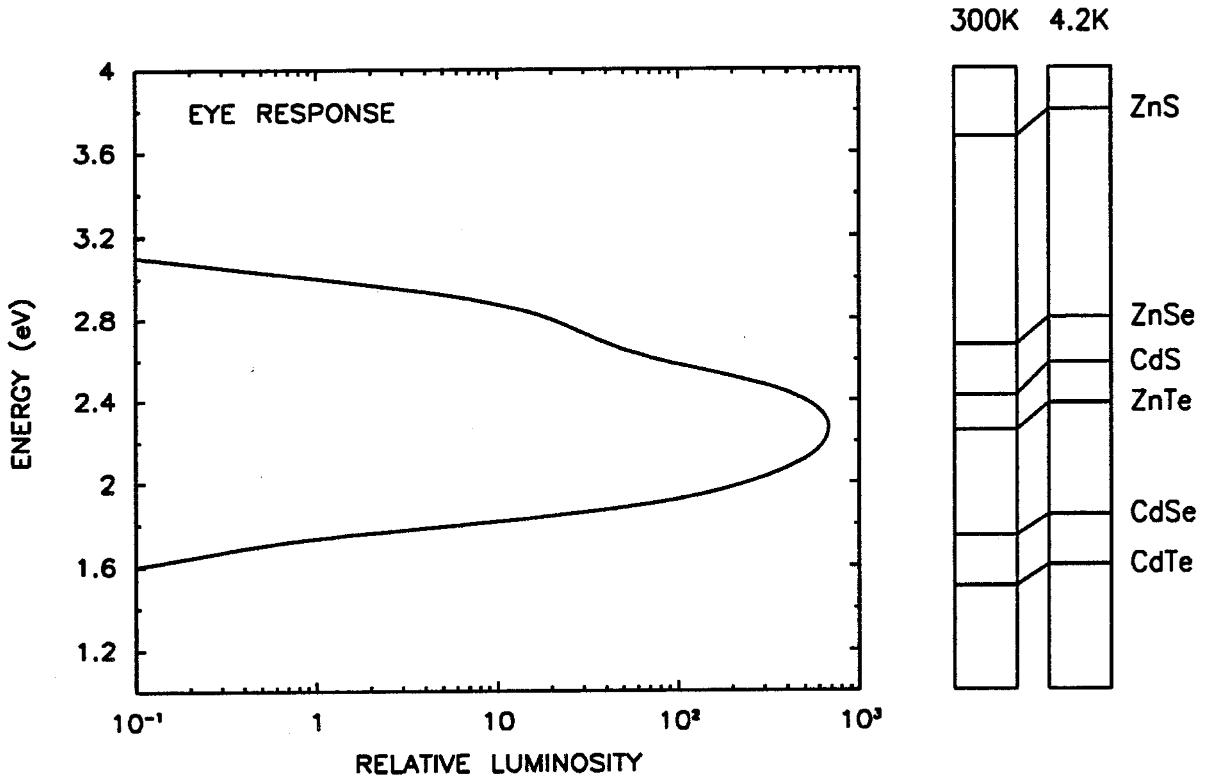

Figure 1.3: Wavelength response of the human eye, against the band gaps of wide-gap II-VI semiconductors. This diagram illustrates that ZnSe and ZnTe are ideal candidates for visible light-emitters.

concentrations (*e.g.* p-type ZnTe). Studies suggest that metastable regimes might exist at low-temperature, where the compensation processes associated with defect generation are frozen out and blocked by large kinetic barriers. Secondly, extensive work done in the 1970s suggested that extrinsic impurities in the wide-gap II-VI materials were responsible for the inability to dope them selectively. The impurities such as Cu were thought to be troublesome species that induce deep impurity states in the band gaps of these materials, severely limiting their useful electrical properties. There may be elements of truth to both these arguments as suggested by the extensive amount of experimental evidence available to support them, and it is reasonable to assume that both the extrinsic impurity problem and the intrinsic defect-associated compensation problem may have to be solved in some fashion before it is possible to achieve successful doping of these material in both n- and p-types.

Progress in heteroepitaxy in the 1980s has opened up several interesting possibilities that have positive bearings on the II-VI's. The II-VI MBE growth can be achieved at 200-300 °C , which is at a much lower temperature than the traditional bulk growth temperatures, which are usually in the range 1000-1200 °C . At these low growth temperatures, it may be possible to attain metastable material that would be unattainable by bulk growth techniques, which might show uncompensated electrical properties. It is well-known that metastability can be controlled under certain circumstances. For instance, under MBE growth conditions at low-temperature it is possible to achieve MnTe in the cubic zincblende structure, although the bulk grown crystals of MnTe exhibit the hexagonal NiAs crystal structure. Recent attempts to dope ZnSe with Li suggest that p-type ZnSe can be obtained, although it may be metastable. We hope that low-temperature growth techniques may prove the key to suppressing compensation phenomena in many of the wide band gap II-VI's. The process of formation of vacancies could be suppressed by techniques such as atomic layer epitaxy (ALE), where precise control of cation and anion compositions of each layer is achieved. Many other techniques such as photo-assisted molecular beam epitaxy (PAMBE) have been tried, in an attempt to control these metastable growth regimes with external perturbations. Furthermore, it is quite reasonable to assume that the growth under ultra high vacuum, from high purity source materials would also help to reduce the incorporation of extrinsic impurities into the wide band gap II-VI materials, thereby suppressing the extrinsic compensation mechanisms as well.

Another approach that goes hand in hand with the new low-temperature growth techniques is the heterojunction approach. The ability to achieve abrupt composition and doping profiles has contributed much to the success of the GaAs-based III-V electronics. The implementation of similar ideas in the II-VI's should be possible, with the growth techniques such as MBE and MOCVD. The heterojunction approach has opened up a variety of possibilities for engineering structures, with specific band-edge profiles and doping profiles. For instance, the basic II-VI doping problem of achieving both n-type, and p-type conductivity within a given bulk material can be easily circumvented by considering p-n heterojunctions. This opens up possibilities such as n-ZnSe/p-ZnTe and n-CdTe/p-ZnTe heterojunctions for light-emitters. The approach taken in this thesis has been to consider the important issues in the II-VI heterojunction approach, such as band alignments, dopability, availability of wide band gaps, and lattice-mismatch criteria, and evaluate the prospects for blue/green light-emission from heterojunctions based on the binaries, ternaries, and quaternaries of several II-VI compounds. The role of the band offset in determining the possibilities for minority carrier injection in heterojunctions is illustrated in Fig. 1.4.

We have also theoretically investigated the possibility of kinetically suppressing the self-compensation processes in semiconductors, by the application of an external electric field during the crystal growth process. The results we obtain show definite promise for controlling the compensation process. We feel that further development of II-VI heteroepitaxy, and techniques to control metastability by variation of external

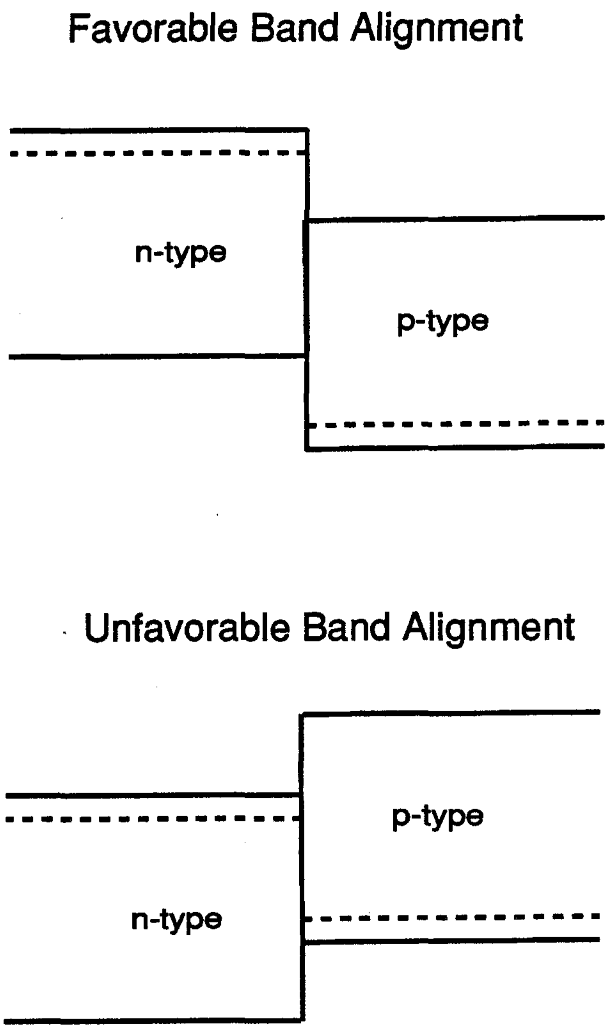

Figure 1.4: Figure shows two possible band alignments for a p-n heterjunction consisting of the same two semiconductors. In the top diagram, the n-type material is able to inject into the p-type material, and vice versa. However, in the second case, electron and hole injection is blocked by the band offsets.

perturbations such as electric fields could lead to success with the long-standing problems in II-VI's.

1.4 Semiconductor Superlattices

Superlattices play a central role in this thesis. This section is intended to serve as a general introduction to superlattices, and to show how they can be used in designs of semiconductor devices. For the most part of this thesis, we have manipulated the extra degree of flexibility offered by band offsets and strain effects to achieve the particular superlattice structures with desired optical properties.

Novel crystal growth techniques such as MBE have enabled the fabrication of semiconductor superlattices with novel electronic and optoelectronic properties. Since first proposed by Tsu and Esaki[2] in 1970, they have attracted a considerable amount of attention due to their ability to directly modify the electronic band structure by simple schemes such as variation of the layer thicknesses. The band gaps, effective masses, and densities of states of the superlattice can be significantly different from bulk values.[21] A schematic diagram of a superlattice is shown in Fig. 1.5 The superlattice itself is a set of alternating layers of two semiconductors. The layer thicknesses and the compositions of unit cells are controlled to achieve a periodic structure. Since the unit cell of the superlattice is large in the growth direction, consequently, the first Brillouin zone of the superlattice in the growth direction is restricted to a smaller volume in k-space than in the bulk. Thus, several minibands arise in the band structure as a result of the new periodicity of the superlattice potential. In this section we describe the role of buffer layers, advantages of superlattices, and optical properties of superlattices that concern the work reported in this thesis.

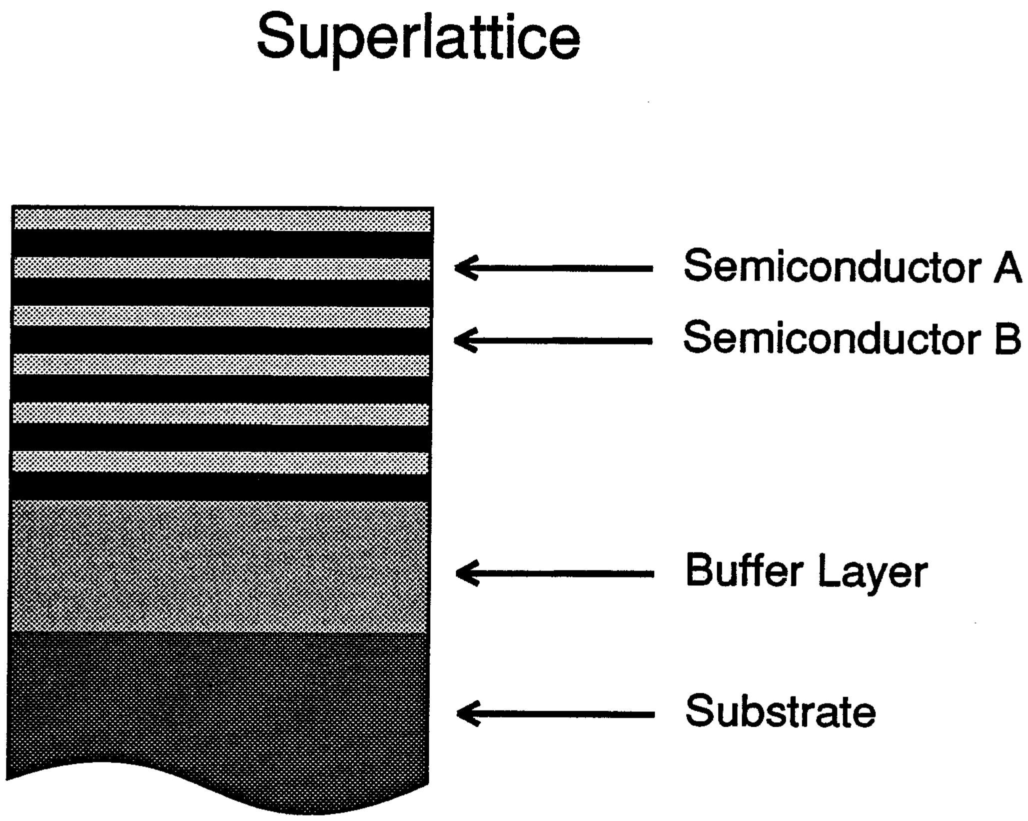

Figure 1.5: Schematic illustration of a semiconductor superlattice. The superlattice is a layered semiconductor structure that has a periodic layer sequence of two constituent semiconductors A and B. Usually, the superlattice is grown on a thick semiconductor substrate, with an intervening buffer layer.

1.4.1 Role of Buffer Layers

Typically, a superlattice is grown on a semiconductor substrate, with an intervening buffer layer. This buffer layer is indicated in Fig. 1.5. The correct choice of the buffer layer is important to achieve certain desired structural and electronic properties of the superlattice. For example, in the case of a coherently strained superlattice, the in-plane lattice constant of the buffer layer may determine the strain distribution in the subsequent superlattice overlayers.[22] Buffer layers could also play the important role of bending dislocations that thread through the substrate and prevent the propagation of dislocations into the superlattice overlayers. Experimental studies have shown that buffer layers with short-period superlattices could improve the structural quality of the subsequent overlayers in the manner described above.[23]

In this thesis, on several occasions we have employed the additional flexibility offered by the choice of buffer layers to customize the superlattice strain distributions. In the theoretical investigations of $Si_{1-x}Ge_x/Si$ superlattices, we have optimized the buffer layer compositions to provide an in-plane lattice constant that is favorable for obtaining increased intersubband absorption strengths.[10] We have also investigated the role of several III-V buffer layers on the optical properties of II-VI epilayers.[24]

1.4.2 Advantages of Superlattices

There are several advantages to superlattices over bulk semiconductor alloys. Because of the additional flexibility offered by superlattices, it is possible to vary several electronic properties independently of each other. For instance, it is possible to vary the energy gap and the effective masses perpendicular to the epilayers almost independently of each other, by variation of the layer thicknesses.[5] The energy gap will depend strongly on the well thicknesses since quantum-well energy levels are not sensitive to barrier thickness, and the effective mass will depend largely on the barrier thickness, since dispersion of the minibands are insensitive to the well thickness.[22] In situations where the composition is difficult to control accurately, as in $Hg_{1-x}Cd_xTe$ alloys with small Cd concentrations, it is easier to achieve better uniformity by controlling the layer thicknesses of a superlattice. These considerations have motivated the use of HgTe/CdTe superlattices over $Hg_{1-x}Cd_xTe$ alloys.[5]

Radiative efficiencies of superlattices have been observed to be much greater than for bulk alloys. Although the reason for this is not entirely understood, plausibility arguments have been proposed, attributed to improved carrier confinement, defect and impurity gettering at the interfaces, and reduction of surface recombination velocities. We have experimentally observed this remarkable increase of luminescence in superlattices over bulk alloys, and this fact has motivated our investigation of II-VI light-emitters based on superlattice radiators.[11]

1.4.3 Novel Properties of Superlattices

Often, certain superlattices exhibit properties that have no direct analogs with bulk alloys. In this thesis, we give two examples of such effects in Si/Ge superlattices. First, the superlattice could exhibit a direct band gap, although the bulk alloy is an indirect band gap material for all alloy compositions. This has led to the possibility of enhancing the optical matrix elements of superlattices by 3-4 orders of magnitude over bulk $Si_{1-x}Ge_x$ alloys. Second, it is possible to engineer a tensor electron effective mass in the ground state of $Si_{1-x}Ge_x/Si$ superlattices grown on certain orientations. Thus, it is possible to apply a force on the electrons in a given direction, and to obtain an electron motion orthogonal to that direction. We have engineered this effect to couple normally incident infrared radiation (electric field variation in the plane of the superlattice) to obtain intersubband transitions (electron motion perpendicular to the plane of the superlattice).

1.5 Strain Effects

An important degree of freedom that allows additional possibilities in semiconductor heterostructures is the control of strain effects.[25] In this section, we discuss important changes that occur in the electrical and optical properties of semiconductor epilayers and superlattices as a result of strain. Particular emphasis will be given to strain-induced effects on the band structure of heterostructures relevant for the work presented in this thesis.

In Fig. 1.6 we have shown a diagram of the band gaps of several semiconductors against their lattice constants. The restriction of lattice-match severely limits the number of interesting semiconductor pairs that can be employed in heterostructures. However, relaxation of the lattice-match condition for heterostructures and permitting a lattice-mismatch <6-7% will allow interesting combinations of materials.[25] The recent success of lattice-mismatched heteroepitaxy such as Si/Ge heterojunction bipolar transistors,[17, 18] has shown that strained-layer heterostructures have potential for future applications.

1.5.1 Strain-Induced Effects on the Band Structure

Strain effects change the band structure of semiconductors because of the lowering of symmetry from cubic to tetragonal ([100] strain), or trigonal ([111] strain). In most cases, the most significant effect of strain is the splitting of the degeneracy of the band structure at the critical points. For zincblende semiconductors, the valence band degeneracy at the zone-center Γ will be split. For instance, this splitting between the heavy-hole and the light-hole bands could change the transport properties of p-type semiconductors quite significantly. In this section we summarize the effect of strain on the band structure of direct band gap materials (ZnTe, ZnSe), and indirect band gap materials (Si, Ge). These considerations are important for much

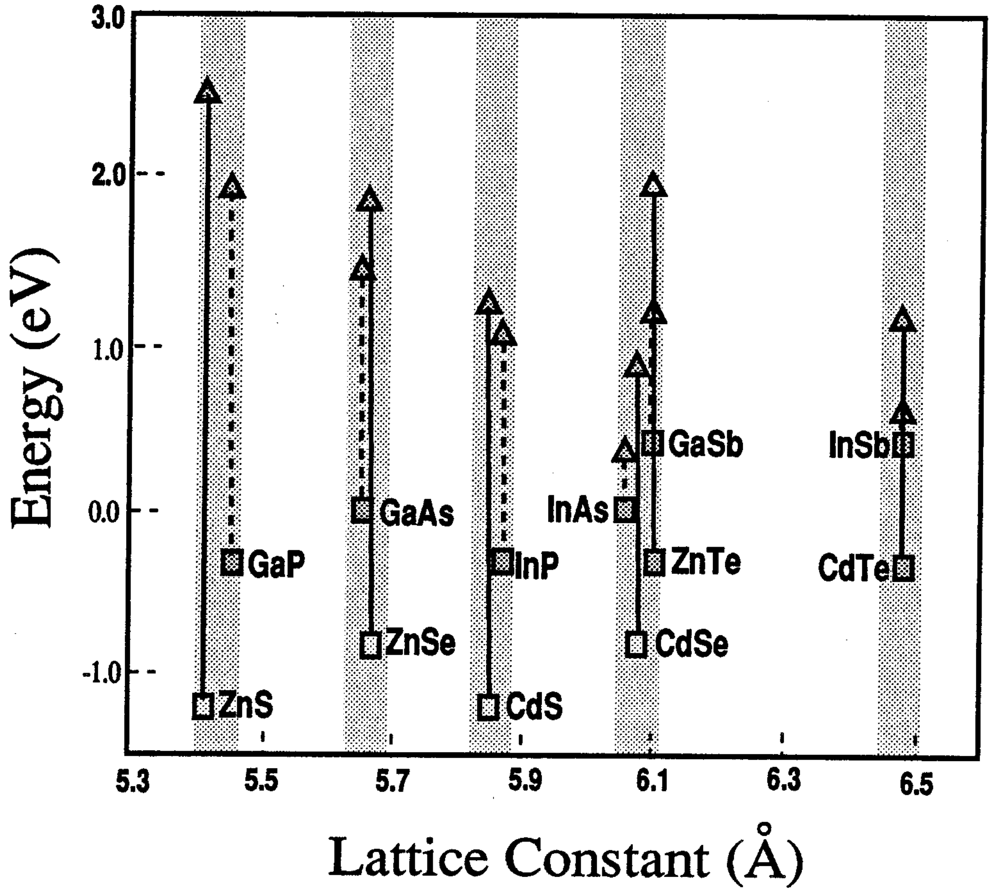

Figure 1.6: Semiconductor band alignment versus lattice constant. The positions of the band-edges have been determined, consistent with the band offset results of McCaldin et al.[26] The valence band-edges are denoted by squares, while conduction band-edges are denoted by triangles. The filled squares and triangles denote *p*- and *n*-type dopability, respectively. The shaded gray areas show the nearly lattice-matched semiconductor groups. The II-VIs are indicated by solid lines, while the III-Vs are indicated by dashed lines. Diagrams of this type are further discussed by McCaldin.[27]

of the work presented in the following chapters.

The interesting wide band gap II-VI heterostructures such as CdTe/ZnTe and ZnSe/ZnTe have lattice-mismatches of 6.2% and -7.1%, respectively. The minus sign on the lattice-mismatch indicates that ZnSe has a smaller lattice constant than ZnTe, while the opposite is true for CdTe. The formalism for the calculation of strain effects in these direct band gap semiconductors will be developed in Chapter 4. However, typical changes in the band structure that are due to strain effects corresponding to a $\approx$6-7 % lattice-mismatch can be 100-200 meV shifts in the direct band-edge positions. In the case of narrow band gap structures, or structures with small band offsets, these can be a very large percentage effects. Thus, it is necessary to treat the strain effects on the same footing as quantum confinement effects. For the purpose of executing this task, in this thesis we have used an eight-band $\vec{k} \cdot \vec{p}$ model that includes strain effects of direct band gap semiconductors systematically.

In Fig. 1.7 we show the band structure of strained ZnSe and ZnTe layers, each strained oppositely to lattice-match to a $ZnTe_{.5}Se_{.5}$ buffer layer. The purpose of this figure is to illustrate the relative movement of the bands that occurs as a result of strain. The original, unstrained band edge positions are shown as dotted lines. However, as a result of strain, the band-edge positions can shift, and split in energy.

For the purpose of this thesis, we calculate strain effects on the band structure by phenomenological deformation potentials. We use a four parameter deformation potential model that incorporates hydrostatic shifts in the valence bands, uniaxial splittings of the valence bands in [100] and [111] directions, and hydrostatic shifts in the conduction bands. In the presence of strain effects, the band offsets between the materials could change as shown in Fig. 1.7. However, if the unstrained offset is known, and the strain distribution in the structure is known, then it is always possible to calculate the band offset after the introduction of strain effects by the phenomenological deformation potential theory. So, for the purpose of this thesis, we will always refer to the unstrained offset (before strain effects are introduced) by the term "band offset". This approach eliminates the necessity for describing the band offset as a function of layer thicknesses.

In indirect band gap materials such as Si and Ge, strain effects will lift the conduction band degeneracy. These degenerate conduction valleys can split and shift in energy, altering the band alignments significantly. In the case of Si, uniaxial stress in the [100] direction will lift the six-fold degeneracy into two-fold longitudinal valleys and four-fold transverse valleys. It is possible to account for the strain effects in these materials with the phenomenological deformation potential model developed by Herring and Vogt.[28] Detailed description of this model is given in Chapter 2. The conduction band splitting of the indirect valleys is much bigger than in the direct gap case. It is possible to move the conduction band-edges by as much as 700 meV for a lattice-mismatch of only $\approx 4.2\%$ (as in Si/Ge case). Thus, strain effects offer an excellent range for manipulating the band-edge positions in these materials.

1.5.2 Strain Relaxation

Although strain effects that are due to elastically accommodated coherent strain are desirable and could be easily controlled, in real situations strain relaxation can occur via the formation of dislocations.[29]-[33] These dislocations can severely interfere with optical and electronic properties of strained-layer devices. However, there is usually a critical-thickness for pseudomorphic growth of dislocation-free, strained epitaxial layers on lattice-mismatched templates. Beyond this critical-thickness, it is thermodynamically favorable to form misfit dislocations and to accommodate the lattice-mismatch. Experimental evidence suggests that under low growth temperatures (as used in MBE), it may be possible to achieve dislocation-free epitaxial layers thicker than predicted by equilibrium critical-thickness models. The investigation of the degree of strain relaxation via dislocation formation, and the development

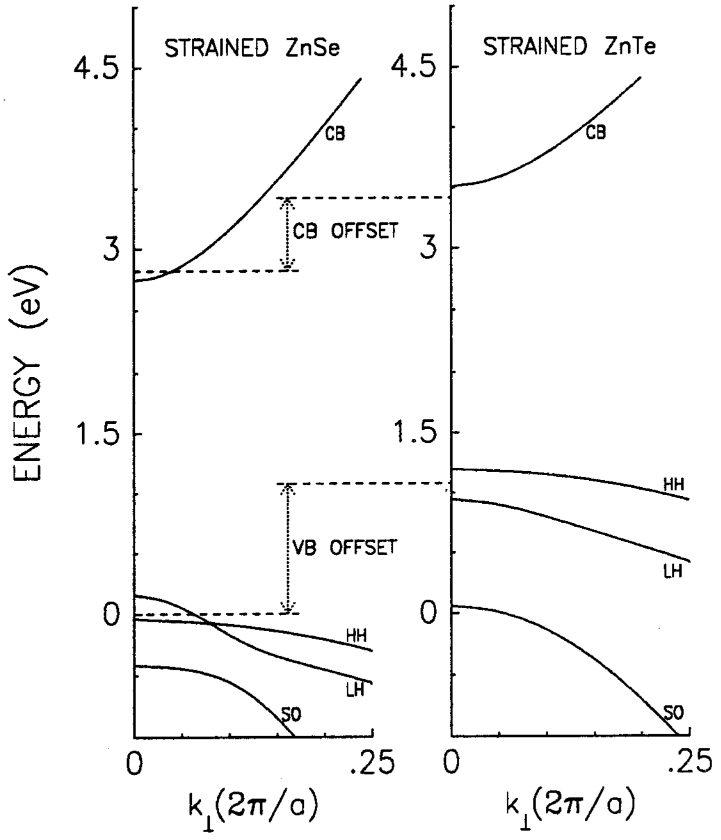

Figure 1.7: The band structure of strained ZnSe and ZnTe. The strain distributions are appropriate for a freestanding ZnSe-ZnTe superlattice with equal ZnSe and ZnTe layer thicknesses. This band structure was calculated with an eight-band $\vec{k}\cdot\vec{p}$ model.

of critical-thickness criteria that are applicable for MBE growth temperatures have been areas of intense investigation over the past few years.[34] However, these topics are not explicitly addressed in this thesis. In our analysis, we have made simplifying assumptions about strain relaxation consistent with recent experimental work of others.

There are two critical-thicknesses that are of interest in strained-layer superlattices. The first is the critical-thickness for individual layers of the superlattice. In this work, we have assumed that the individual layers are thin enough, or alternatively, the lattice-mismatch is not large enough to exceed this critical-thickness in the structures considered. Thus, we always consider that the superlattice layers are coherently strained within the superlattice unit cell. Secondly, there is another critical-thickness for the overall superlattice structure for growth on a lattice-mismatched buffer layer. Experimentally, it is found that if the superlattice thickness exceeds the critical-thickness for pseudomorphic growth on the buffer layer, then the superlattice layers break away from the buffer layer, into the freestanding configuration. The freestanding configuration is defined as the superlattice structure that minimizes the strain energy by accommodation of purely elastic strain. However, if the total thickness of the superlattice is not large enough to exceed this critical-thickness, we assume that the superlattice is coherently strained to the buffer layer. In this thesis, we have considered cases where it is appropriate to consider freestanding superlattices as well as superlattices lattice-matched to buffer layers. However, we have explicitly stated which type of superlattice is considered in the context.

1.5.3 Advantages of Coherent Strain

Certain effects that are due to strain can be used to our advantage in device design. For instance, some of our designs on the superlattice radiator layers were optimized to have the largest strain-induced, valence-band splitting to obtain significant barriers for holes in the $Zn_{1-x}Cd_xTe$-ZnTe system. In the Si/Ge system, heterojunction bipolar transistors have been proposed to take advantage of the fact that the electron mobility can be significantly altered as a result of strain.[17, 18] Another situation is the $In_xGa_{1-x}Sb$/InAs system, where strain-induced changes in the band structure have made the possibility of a novel IR detector.[35, 36] In our analysis of the intersubband absorption in Si/Ge superlattices, we have used strain effects to our advantage, to achieve favorable carrier confinement, and obtain large, intersubband optical matrix elements.[10] The [111] oriented, strained III-V superlattices have attracted attention as a system that exhibits strain-induced, internal electric fields that could be potentially useful in optoelectronic applications.[37]

The purpose of this brief discussion of strain effects in superlattices and heterostructures was to motivate our study of strained-layer structures. Throughout this thesis, we have utilized strain-induced band structure effects to enhance the optical properties under study. We feel that utilization of strain effects in future semiconductor applications show promise, although considerations such as the stability and reliability of these structures have yet to be addressed.

1.6 Theory of Superlattice Band Structure

A major portion of this thesis is concerned with the theoretical calculations of the band structure of semiconductor superlattices. The method of choice for our calculations is the complex band structure $\vec{k} \cdot \vec{p}$ method. We have used this technique to obtain electronic and optical properties of wide-gap II-VI materials and Si/Ge structures. In the case of the III-V materials and narrow-gap II-VI materials, the theoretical $\vec{k} \cdot \vec{p}$ formalism was already worked out in the previous theses by Wu[38] and Mailhiot[39]. However, we have applied these techniques to wide-gap II-VI semiconductors to guide our designs of novel heterostructures and estimate the band alignments based on experimental data. The details of the band structure calculations on the II-VI materials are given in Chapter 4. In the case of the Si/Ge superlattices, we developed a new formalism for calculating the band structure of indirect gap Si/Ge superlattices within a full-zone $\vec{k} \cdot \vec{p}$ scheme. The details of these calculations are given in Chapter 2.

We use the $\vec{k} \cdot \vec{p}$ method because it is quite easy to implement for superlattices with only a modest computational effort, and it provides excellent results in agreement with experiments. It is easy to use empirical parameters such as effective masses in the calculations, and thus provides an accurate description of the band structure near the regions of interest. It is straightforward to include perturbations such as spin-orbit interaction, strain effects, electric and magnetic fields into the Hamiltonian. It is well suited for the calculation of optical properties, because the optical matrix elements are readily available through the $\vec{k} \cdot \vec{p}$ parameters. Furthermore, it is quite easy to extend to thick layer superlattices, since the problem size is independent of the layer thicknesses. Despite these advantages, this technique has several drawbacks, and for the rest of this section we will outline several theories of superlattice band structure, and critically compare them with our method of choice, the complex band structure $\vec{k} \cdot \vec{p}$ method.

1.6.1 Envelope Function Approximation

Unless the layers are ultrathin, (few monolayers thick), it is very difficult to calculate the band structure of superlattices by microscopic, first-principles calculations. This is because it is necessary to include a large a number of atoms in the basis, which makes the calculations prohibitively time-consuming. The usual approach is first to solve for the band structure of the constituent layers by some microscopic technique such as empirical pseudopotentials, tight binding or a detailed $\vec{k} \cdot \vec{p}$ model, and then to impose the envelope function approximation. If proper boundary conditions at the interfaces could be specified, the envelope function approximation proves quite adequate for solving the band structure of superlattices between fairly similar semiconductors. Another criterion for the validity of the envelope function approach is that constituent layer thicknesses should be substantially larger than the bulk unit cell size. Luttinger and Kohn[40], who pioneered the envelope function formalism have shown that the error introduced in making the envelope function approximation scales like $(a/L)^2$, where a is the unit cell size, and L is the length scale of the envelope function potential (in the case of superlattices, this length scale would be the well thickness). However, studies on $Al_xGa_{1-x}As$/GaAs superlattices have shown that, even in the case of ultrathin layers $L \approx a$, the predictions based on the envelope function approximation still prove to be in reasonable agreement with experimental results.

Among the more important calculational techniques for the superlattice band structure are the envelope function method, complex $\vec{k} \cdot \vec{p}$ method,[37] complex $\vec{k}$ tight binding method,[41] and the mini-zone pseudopotential method.[42] We will briefly review the main concepts of each of these techniques, and will discuss the potential advantages and disadvantages in each case. In the following discussion we have expressed all equations in atomic units in which the unit of length is the Bohr radius (0.529 Å), $\hbar$ is the unit of action, and the Rydberg (1 Ryd. = 13.6 eV) is the unit of energy. In these fundamental units, the unit of mass becomes $\frac{1}{2}$ times the electron rest mass and the charge of an electron $\sqrt{2}$.

The first step in the envelope function technique is to approximate the bulk band structure with the $\vec{k} \cdot \vec{p}$ method (usually at the center of the zone). For the case of III-V or II-VI materials with direct band gaps, it is usually adequate to consider the eight-band $\vec{k} \cdot \vec{p}$ model (usually known as the Kane model).[43] This method includes two Γ_6 (conduction) bands, four Γ_8 (heavy-hole and light-hole) bands, and two Γ_7 (spin-orbit) bands explicitly in the basis set. However, further simplifications in appropriate cases could reduce the size of the matrices. A particularly simple form that is appropriate for the conduction bands and light-hole bands of narrow band gap semiconductors is the two-band model.[44]

The $\vec{k} \cdot \vec{p}$ procedure, which includes terms up to second-order in k yields an expression of the following form, for the Hamiltonian

$$H_{ij}(\vec{k}) = E_i \delta_i + P_{ij}^{\alpha} k_\alpha + Q_{ij}^{\alpha\beta} k_\alpha k_\beta, \tag{1.1}$$

where i, j denote the bands in the Hamiltonian, and α, β denote the directions x, y and z. Repeated indices are summed in the usual fashion. All the symmetry requirements of the host crystals are hidden in the quantities P_{ij}^{α} and $Q_{ij}^{\alpha\beta}$. The energy bands can be obtained by the solution of the following determinant,

$$\left\| H_{ij}(\vec{k}) - E \right\| = 0. \tag{1.2}$$

We approximate the potential of the superlattice by a multicomponent Schrödinger equation where the appropriate band discontinuities at the interfaces are added to the constant term in Equation 1.1. In the case of superlattices, $k_{||}$ is conserved across the structure since there is no transverse variation of the potential. The kinetic energy would be given by substituting $k_z = -i\nabla_z$ in Equation 1.1, where we have assumed the growth direction to be the z-axis. Then, we obtain the following set of coupled differential equations,

$$\sum_j H_{ij}(k_{||}, -i\nabla_z) F_j(z) = E F_i(z). \tag{1.3}$$

The multicomponent envelope functions $F_i(z)$ are different in each bulk region. To obtain the superlattice band structure, it is necessary to match these envelope functions across the interfaces, and to impose periodic boundary conditions, over the whole superlattice unit cell. The specific boundary conditions such as the microscopic Bloch functions being equal in the two materials, can be adopted, and then appropriate current conservation conditions could be derived by considering the first integral of the set of Equations 1.3 given above. For the case of $Al_xGa_{1-x}As/GaAs$, the boundary condition about the similarity of the Bloch functions in the two materials has proven to be quite good. In the case of II-VI's this approximation should also be quite good considering the similarity of the band structure of all wide band gap II-VI materials. In the case of Si, and Ge, we find that the band structure in the [100] direction is very similar to each other, and this boundary condition should be valid. The major shortcoming of this technique is the fact that it is not possible to derive the interface matching conditions for microscopic Bloch functions within the scope of the theory, but rather they have to be inferred from more detailed microscopic calculations or simplifying approximations. Despite its limitations with the boundary conditions, the envelope function method has contributed to the progress and understanding of a large number of superlattices. A convenient feature of this method is the possibility of including external perturbations such as strain effects, magnetic fields, and electric fields quite systematically.

1.6.2 The Complex $\vec{k} \cdot \vec{p}$ Method

This method is formally very similar to the envelope function strategy explained in the previous section. However, the implementation can be quite different. In this method, instead of replacing the $k_z = -i\nabla$, and solving the second-order differential equations as in the previous method, one determines the multicomponent plane wave solutions. Then the envelope functions are constructed by a linear combination of multicomponent plane waves. Usually, propagating (real k_z) and evanescent (imaginary k_z) solutions are included for the description of the envelope functions. The microscopic boundary conditions have to be imposed at the interfaces, and finally the Bloch condition has to be imposed to obtain the band structure of the superlattice. This is a very straightforward scheme for finding the superlattice band structure in the flat band case. In the cases where band-bending is present, transfer matrix techniques can be employed to obtain the superlattice band structure.

However, the formal simplicity of this method is counterbalanced by the problem of spurious solutions. These are solutions that occur beyond the first Brillouin zone. The occurrence of spurious solutions is related to the fact that the $\vec{k} \cdot \vec{p}$ Hamiltonian is not periodic in k-space, and does not contain information about the Brillouin zone edges, thus leading to solutions outside the zone boundary. In general, these spurious solutions could alter the superlattice band structure considerably, leading to erroneous results. The other problem with the complex band structure technique is that it is susceptible to numerical instabilities when the layer thickness of the superlattice is increased. This is because in the case of bands with large imaginary parts, it is necessary to evaluate quantities such as $e^{-\kappa d}$ and $e^{+\kappa d}$, and take numerical differences. If the numerical difference is less than the finite precision of the computer, numerically unstable results are obtained.

However, in practice there are cases when one can consider only the bands of interest, and neglect the troublesome imaginary bands that give rise to numerical problems and the spurious bands outside the zone. In the eight-band $\vec{k} \cdot \vec{p}$ model employed to solve the band structure of wide band gap II-VI materials, spurious solutions beyond the first Brillouin zone do not arise, and the pure imaginary bands can be neglected without altering the numerical results. We have checked the answers with and without the contributions from these bands, and have found that their effects are very small (smaller than $\approx .01$ meV) on the final superlattice band structure. In the case of Si/Ge, the full-zone formalism developed in this thesis gives rise to several spurious bands outside the first Brillouin zone. However, for the lowest conduction band in the [100] direction, it is possible to neglect the spurious solutions as illustrated in the work of Sterke and Hall.[45] This simple-minded approach of neglecting the troublesome bands is not satisfactory in a formal sense, and cannot be applied in a general situation. Recently, Smith and Mailhiot[46] have worked out a formalism for full-zone $\vec{k} \cdot \vec{p}$ that is periodic in the repeated zone scheme, which shows promise for systematic description of interfaces between dissimilar materials.

1.6.3 Comparison with Other Methods

Superlattice Tight Binding Method

The basic idea behind this technique is to replace the linear and quadratic expressions of k in the $\vec{k} \cdot \vec{p}$ Hamiltonian by band structure that is periodic in k, and valid over the repeated zone scheme. One possible way to achieve such a Hamiltonian is the tight binding method. In principle it is then possible to obtain the band structure of superlattices using the envelope function approximation based on the complex-k tight binding Hamiltonian. The other approach is to consider a basis set that spans the whole superlattice unit cell, and then diagonalize the resulting tight binding Hamiltonian. Both these tight binding techniques can be applied successfully[47] with the advantage of systematic boundary conditions, since these techniques use microscopic localized orbitals. The actual implementation of these techniques is quite involved, and will not be discussed here.[41] Despite its advantages, the tight binding method suffers from the drawback that it is not as well suited for studying optical and strain-induced effects in comparison with the $\vec{k} \cdot \vec{p}$ technique.

Superlattice Pseudo Potential Method

The empirical pseudopotential method has been very successful at describing the overall band structure of zincblende semiconductors.[48] In the superlattice band structure calculations, the band structure of an ''auxiliary medium'' is found first, and then this band structure is folded into the reduced zone of the superlattice. This auxiliary medium could be either one of the constituent materials, or an average bulk between them. Next, the difference between the real superlattice potential and the auxiliary medium is expanded in the basis set of the mini bands of the auxiliary crystal, and added to the Hamiltonian. The resulting Hamiltonian is diagonalized to give the band structure of the superlattice. However, the disadvantage of this method is the fact that the size of the matrix necessary to diagonalize increases linearly in size with superlattice layer thickness. Despite its advantages, the superlattice pseudopotential method suffers from the drawback that it is difficult to include external perturbations in comparison with the $\vec{k} \cdot \vec{p}$ technique.

This brief discussion of the status of current superlattice band structure techniques was presented to sumarize the advantages and disadvantages of various approaches. Although we have used exclusively the complex band structure $\vec{k} \cdot \vec{p}$ technique in this thesis because it provides an adequate description of the band structure of the first few subbands and the optical properties of superlattices, it is necessary to keep in mind its limitations.

1.7 Outline of Thesis

In this chapter, we introduced the general subject matter covered in this thesis. The main concepts introduced are: superlattices, strain effects, and band structure calculations. The key issues addressed in this thesis are, optical properties of Si/Ge superlattices, band alignments and doping of II-VI semiconductors. In Chapter 2 we analyze the interband transitions in Si/Ge superlattices, and evaluate their merits for optoelectronic applications. In Chapter 3 we analyze the intersubband absorption in Si/Ge superlattices for long-wavelength infrared detectors. In Chapter 4 we investigate the band alignment of II-VI heterostructures for visible light-emitter applications. In Chapter 5 we investigate the role of electric fields in suppressing self-compensation.

References

[1] L. Esaki, in *The Technology and Physics of Molecular Beam Epitaxy*, edited by E. H. C. Parker, Plenum, New York (1985).

[2] R. Tsu and L. Esaki, *IBM J. Res. Dev.* **14**, 61 (1970).

[3] L. L. Chang, L. Esaki, W. E. Howard and R. Ludeke, *J. Vac. Sci. Technol.* **10**, 11 (1973).

[4] H. Sakaki, L. L. Chang, R. Ludeke, C. A. Chang, G. A. Sai-Halasz, and L. Esaki, *Appl. Phys. Lett* **31**, 211 (1977).

[5] J. N. Schulman and T. C. McGill, *Appl. Phys. Lett.* **34**, 663 (1979).

[6] Y. Rajakarunanayake and T. C. McGill, *Phys. Rev. B* **40**, 3054 (1989).

[7] C. I. Yang, D. S. Pan, and R. Somoano, *J. Appl. Phys.* **65**, 3253 (1989).

[8] E. R. Brown and S. J. Eglash, *Phys. Rev. B* **41**, 7559 (1990).

[9] B. F. Levine, K. K. Choi, C. G. Bethea, J. Walker, and R. J. Malik, *Appl. Phys. Lett.* **51**, 934 (1987).

[10] Y. Rajakarunanayake and T. C. McGill, *J. Vac. Sci. Technol.* , to appear in (1990).

[11] Y. Rajakarunanayake and T. C. McGill, *Proc. SPIE* , to appear in (1990).

[12] M. Aven and B. Segall, *Phys. Rev.* **130**, 81 (1963).

[13] R. S. Title, G. Mandel, and F. F. Morehead, *Phys. Rev.* **136**, A300 (1964).

[14] R. S. Title, in *Physics and Chemistry of II-VI Compounds*, edited by M. Aven and J. S. Prener, North Holland, Amsterdam (1967).

[15] Y. Rajakarunanayake, J. O. McCaldin and T. C. McGill, *J. Cryst. Growth* , to be published (1990).

[16] E. Kasper and J. C. Bean, in *Silicon Molecular Beam Epitaxy*, Chemical Rubber, Boca Raton, FL (1987).

[17] T. Tatsumi, H. Hirayama, and N. Aizaki, *Appl. Phys. Lett.* **52**, 895 (1988).

[18] H. Temkin, J. C. Bean, A. Antreasyan, and R. Leibenguth, *Appl. Phys. Lett.* **52**, 1089 (1988).

[19] T. P. Pearsall, J. Bevk, L. C. Feldman, J. M. Bonar, J. P. Manaerts, and A. Ourmazd, *Phys. Rev. Lett.* **58**, 729 (1987).

[20] F. A. Kroger, in *The Chemistry of Imperfect Crystals*, North Holland, Amsterdam (1973).

[21] D. L. Smith, T. C. McGill, and J. N. Schilman, *Appl. Phys. Lett.* **43**, 180 (1983).

[22] R. H. Miles, in *Structural and Optical Properties of Strained-layer Superlattices*, Thesis, California Institute of Technology (1988).

[23] S. Kalem, J. I. Chyi and H. Markoc, *Appl. Phys. Lett.* **53**, 1648 (1988).

[24] Y. Rajakarunanayake, B. H. Cole, J. O. McCaldin, D. H. Chow, J. R. Söderström and T. C. McGill, *Appl. Phys. Lett.* **55**, 1217 (1989).

[25] G. C. Osbourn, *Phys. Rev. B* **27**, 5126 (1983).

[26] J. O. McCaldin, T. C. McGill and C. A. Mead, *Phys. Rev. Lett.* **36**, 56 (1976).

[27] J. O. McCaldin, *J. Vac. Sci. Technol* , to be published (1990).

[28] C. Herring, and E. Vogt, *Phys. Rev.* **101**, 944 (1956).

[29] J. H. Van der Merwe, *J. Appl. Phys.* **34**, 123 (1963).

[30] C. A. B. Ball and J. H. Van der Merwe, in *Dislocations in Solids*, edited by F. R. N. Nabarro, North Holland, Amsterdam (1983).

[31] J. W. Matthews, in *Epitaxial Growth*, edited by J. W. Matthews, Academic Press, New York (1968).

[32] J. W. Matthews and A. E. Blakeslee, *J. Cryst. Growth* **27**, 118 (1974).

[33] R. People and J. C. Bean, *Appl. Phys. Lett.* **47**, 332 (1985).

[34] B. W. Dodson and J. Y. Tsao, *Appl. Phys. Lett.* **51**, 1325 (1987).

[35] D. L. Smith and C. Mailhiot, *J. Appl. Phys.* **62**, 2545 (1987).

[36] C. Mailhiot and D. L. Smith, *J. Vac. Sci. Technol. A* **7**, 445 (1989).

[37] D. L. Smith and C. Mailhiot, *Phys. Rev. B.* **33**, 8345 (1986).

[38] G. Y. Wu, in *Electronic Properties of II-VI Superlattices and III-V Tunnel Structures*, Thesis, California Institute of Technology (1988).

[39] C. Mailhiot, in *Theoretical Investigations of Electronic States in Small-Scale Semiconductor Structures*, Thesis, California Institute of Technology (1984).

[40] J. M. Luttinger and W. Kohn, *Phys. Rev.* **97**, 869 (1955).

[41] Y. C. Chang and J. N. Schulman, *Phys. Rev. B* **25**, 3975 (1982).

[42] D. Ninno, K. B. Wong, M. A. Gell and M. Jaros, *Phys. Rev. B* **32**, 2700 (1985).

[43] G. L. Bir and G. E. Pikus, in *Symmetry and Strain-Induced Effects in Semiconductors*, Keter, Jerusalem (1974).

[44] G. Bastard, *Phys. Rev. B* **24**, 5693 (1981).

[45] C. M. Sterke and D. G. Hall, *Phys. Rev. B* **35**, 1380 (1987).

[46] D. L. Smith and C. Mailhiot, *Rev. Mod. Phys.* **62**, 173 (1990).

[47] Y. C. Chang and J. N. Schulman, *Phys. Rev. B* **33**, 2594 (1986).

[48] M.L. Cohen and T.K. Bergstresser, *Phys. Rev.* **141**, 789 (1966).

Part I

Si/Ge Structures

Chapter 2

Interband Transitions in Si/Ge Superlattices

2.1 Introduction

This chapter presents calculations of band structure, strain effects, and optical matrix elements in $Si_{1-x}Ge_x$/Si superlattices. The purpose of this study was to investigate the possibility of utilizing interband optical transitions in $Si_{1-x}Ge_x$/Si superlattices for near infrared applications. The results presented here provide a prime example of how bulk semiconductor properties can be modified and customized in superlattices to achieve novel physical properties absent in the bulk constituent materials; for example, $Si_{1-x}Ge_x$/Si superlattices can be engineered to be direct band gap materials, although Si and Ge are each indirect band gap materials.

2.1.1 Background and Motivation

Silicon and germanium have been extremely important materials in the field of semiconductor electronics for the past few decades.[1] However, because of their indirect band gaps, Si and Ge have been considered unsuitable for optoelectronic applications; the optical absorption strengths of pure Si and Ge are several orders of magnitude lower than a typical optoelectronic material such as GaAs.[2] However, recent advances in crystal-growth techniques such as MBE (molecular beam epitaxy) have made possible the fabrication of layered epitaxial structures known as superlattices.[3] $Si_{1-x}Ge_x/Si$ superlattices seem to offer the intriguing possibility of greatly enhanced optical properties compared to pure Si or Ge.[4]-[14] If substantial optical emission/absorption strengths can be obtained in $Si_{1-x}Ge_x/Si$ superlattices, the resulting optoelectronic applications could, in principle, advance the optical communications industry. In particular, compatibility with Si electronics would be a great advantage. Furthermore, the strain-induced lowering of the band gap of $Si_{1-x}Ge_x/Si$ superlattices could be utilized to yield band gaps in the 1.3 - 1.5 μm range (the region of minimum loss in glass optical fibers), making them compatible with fiber optic communication lines.[8] The purpose of this study was to determine the merits of $Si_{1-x}Ge_x/Si$ superlattices for such optoelectronic applications.

The following argument illustrates how direct band gap $Si_{1-x}Ge_x/Si$ superlattices can be obtained, despite the indirect band gaps of bulk Si and Ge. A typical $Si_{1-x}Ge_x/Si$ superlattice grown in the [100] direction can be considered as a crystal with an extended unit cell along the growth axis. Thus, superlattices have reduced Brillouin zones in the growth direction, and qualitatively the bulk energy bands are folded into the reduced zone as shown in Fig. 1.1. For materials such as Si and Ge, it is possible to tailor the folding of the indirect conduction band. If the folded indirect minimum can be brought to the zone-center Γ, the resulting band structure will be direct.[9] In such a case, there will be optical transitions allowed between the top of the folded valence band and the bottom of the folded direct conduction band. A major issue of interest then is whether such $Si_{1-x}Ge_x/Si$ superlattices are useful for optoelectronic devices. To determine the answer to this question, we have calculated the optical matrix elements of $Si_{1-x}Ge_x/Si$ superlattices.

2.1.2 Summary of Results

The aim of this chapter is the calculation of interband optical matrix elements of $\mathrm{Si}_{1-x}\mathrm{Ge}_x$/Si superlattices, for evaluating the merits of $\mathrm{Si}_{1-x}\mathrm{Ge}_x$/Si superlattices for near infrared optoelectronic applications. However, we have also concentrated heavily on the band structure effects and strain-induced effects in Si/Ge superlattices.

Results on Band Structure

We employ the full-zone $\vec{k} \cdot \vec{p}$ method (a 15 band Hamiltonian) for calculating the band structure of $\mathrm{Si}_{1-x}\mathrm{Ge}_x$ alloys, and extend this technique for the calculation of the complex band structure of thin epilayers. We show that in the [100] direction, the lowest conduction band and the heavy-hole band are described by 3×3 Hamiltonian matrices. From the results of our band structure calculations, we show that the one-band model is more appropriate for calculating the complex wavevector of indirect conduction valley electrons. This is in contrast to the situation in direct band gap materials, where a two-band model is more appropriate for calculating the complex wavevector.[15] We have also developed a complex band structure technique to calculate the band structure of $\mathrm{Si}_{1-x}\mathrm{Ge}_x$/Si superlattices employing the envelope function approximation.

We have demonstrated that direct band gap $\mathrm{Si}_{1-x}\mathrm{Ge}_x$/Si superlattices can be achieved for particular layer thickness combinations, and we derive a simple criterion based on the layer thicknesses for obtaining a direct band structure. Furthermore, we find that since the effective masses of the longitudinal X-point electrons in Si and Ge are quite large ($0.98m$), the dispersion in the superlattice band structure is quite small. Thus it is possible for optical transitions to occur from every point in the zone folded valence band to the zone-folded conduction band at near band gap energies; it is not necessary to obtain precisely direct band gap superlattices to achieve optical absorption/emission.

In this chapter, we also describe a novel band structure effect called the intervalley interference effect that exists in superlattices composed of materials with indirect conduction valleys. We find that as a consequence of the intervalley interference effect, the lowest conduction band splits into a doublet. The interference effect is intimately related to the direct/indirect character of $Si_{1-x}Ge_x$/Si superlattices.

Results on Strain Effects

We calculate the position of the strain-dependent conduction band positions of $Si_{1-x}Ge_x$ epilayers as a function of the buffer-layer alloy compositions. We find that for [100] oriented superlattices, the lowest conduction states are the two-fold states if the superlattice consists of Si-rich well layers and Ge-rich barrier layers, grown coherently strained to a buffer-layer with a larger lattice constant than the well layer. This is the required configuration for obtaining strong optical properties that are due to zone-folding. Using a novel theoretical technique to consider the strain effects explicitly in the zone-center basis set, we find that the positions of the conduction minima in k-space do not shift very much as a function of strain, although they move significantly higher or lower in energy as a result of strain. We also show that it is possible to achieve a strain-induced type I/ type II transition in $Si_{1-x}Ge_x$/Si superlattices.

Results on Optical Properties

Our calculations indicate that in $Si_{1-x}Ge_x$/Si superlattices the optical absorption strengths can vary by 3-4 orders of magnitude even for layer-thickness variations as small as 1-2 monolayers. Thus, it is important to control the layer thicknesses to a monolayer accuracy to obtain the enhanced optical absorption strengths predicted in this work. This occurs because the relative phases of the conduction band electron wavefunction at the interfaces play an important role in determining the optical properties. In principle, this situation can be thought of as an example where the phase of the wavefunction can be controlled by changing the layer thicknesses. Recently, this type of flexibility to change the phase of the wavefunctions has been referred to as ''wavefunction engineering'',[16] in the same spirit as the familiar term ''band gap engineering'' that denotes the ability to change the band-edge positions of semiconductors in artificial structures such as superlattices. Although the optical absorption strengths calculated are 3-4 orders of magnitude larger than in bulk Si or Ge, they are still 3 orders of magnitude smaller than the absorption strengths because of direct transitions in materials such as GaAs, limiting the usefulness of $Si_{1-x}Ge_x$/Si superlattices in optical applications.

2.1.3 Outline of Chapter

Section 2.2 presents a detailed derivation of the full-zone $\vec{k} \cdot \vec{p}$ Hamiltonian, and a discussion of the method for calculating the superlattice band structure within the envelope function approximation. Section 2.3 describes the effects of strain on the conduction and valence band-edges of Si and Ge epilayers; explicit equations for the calculation of strain shifts based on phenomenological deformation potential models are also derived. In Section 2.4 we discuss the band offsets in the $Si_{1-x}Ge_x$/Si system. In Section 2.5, we present the results of the band structure calculations of $Si_{1-x}Ge_x$/Si superlattices, and illustrate the novel interference effect. In Section 2.6, we calculate the optical matrix elements of $Si_{1-x}Ge_x$/Si superlattices. Finally, the conclusions of this chapter are summarized in Section 2.7.

2.2 Theory

2.2.1 Full Zone $\vec{k} \cdot \vec{p}$ Theory

The $\vec{k}\cdot\vec{p}$ method is particularly suitable for the calculation of the optical properties because of the ability to directly calculate various optical matrix elements. We have used the full-zone $\vec{k}\cdot\vec{p}$ theory introduced by Cardona and Pollack[17] to calculate the bulk band structure of Si and Ge. In the following discussion we have expressed all equations in atomic units in which the unit of length is the Bohr radius (0.529 Å), $\hbar$ is the unit of action, and the Rydberg (1 Ryd. = 13.6 eV) is the unit of energy. In these fundamental units, the unit of mass becomes $\frac{1}{2}$ times the electron rest mass and the charge of an electron $\sqrt{2}$. One must be careful in evaluating expressions based on atomic units, because there is another type of atomic units where the unit of length is the Bohr radius (0.529 Å), $\hbar$ is the unit of action, but the third quantity is the unit of mass equal to the electron rest mass. In these fundamental units, the unit of energy is the Hartree (1 Hartree = 2 Ryd. = 27.6 eV), and the electron charge is unity.

Consider the one-electron Schrödinger equation for a crystal, written in the first set of atomic units (these units will be used throughout this chapter)

$$\left[-\nabla^2 + V(\vec{r})\right] \Psi = E\Psi, \tag{2.1}$$

where $V(\vec{r})$ is the potential having the periodicity of the lattice. The solution to Equation 2.1 are Bloch functions of the form

$$\Psi = e^{i\vec{k}\cdot\vec{r}} u_{n,\vec{k}}(\vec{r}), \tag{2.2}$$

where n is the band index and $\vec{k}$ denotes the wavevector within the first Brillouin zone; the wavefunctions $u_{n,\vec{k}}(\vec{r})$ have the periodicity of the crystal lattice. By sub-

Zone center state	Si	Ge
Γ^{l}_{25}	.0000	.0000
$\Gamma^{l}_{2'}$	.2650	.0728
Γ_{15}	.2520	.2320
Γ^{u}_{1}	.5200	.5710
Γ^{l}_{1}	-.9500	-.9660
$\Gamma_{12'}$	.7100	.7700
$\Gamma^{u}_{25'}$	.9400	1.2500
$\Gamma^{u}_{2'}$	.9900	1.3500

Table 2.1: Zone center energies (in Rydbergs) used in the full-zone $\vec{k}\cdot\vec{p}$ calculations. The alloy properties are calculated by averaging Si and Ge values. These values were obtained from Reference[17] .

stituting the Bloch functions of Eq. 2.2 in Eq. 2.1, we obtain

$$\left[H_0 + 2\vec{k}\cdot\vec{p} + k^2\right] u_{n,\vec{k}}(\vec{r}) = E_n(\vec{k}) u_{n,\vec{k}}(\vec{r}). \tag{2.3}$$

Here, H_0 is the Hamiltonian at $\vec{k} = 0$. The terms k^2 and H_0 have only diagonal terms, and the $\vec{k}\cdot\vec{p}$ term has only off-diagonal terms (this is true only in a crystal with inversion symmetry, such as Si or Ge).

It is well-known that the wavefunctions at an arbitrary point in the Brillouin zone can be expanded as a linear combination of the zone-center basis set.[18] We have kept the lowest 15 zone-center basis states corresponding to the [000], the eight $2\pi/a[111]$ and the six $2\pi/a[200]$ plane waves of an empty F.C.C. reciprocal lattice. In the context of group theory, the irreducible representations of these fifteen states correspond to the three three-fold degenerate representations $\Gamma_{15}, \Gamma^{u}_{25'}, \Gamma^{l}_{25'}$,

$\vec{p}$-Matrix Elements		Si	Ge
P	$(2i\langle\Gamma^l_{25'} \mid \vec{p} \mid \Gamma^l_{2'}\rangle)$	1.20	1.36
P'	$(2i\langle\Gamma^u_{25'} \mid \vec{p} \mid \Gamma^l_{2'}\rangle)$	-.090	.1715
P''	$(2i\langle\Gamma^l_{25'} \mid \vec{p} \mid \Gamma^u_{2'}\rangle)$	.100	.100
P'''	$(2i\langle\Gamma^u_{25'} \mid \vec{p} \mid \Gamma^u_{2'}\rangle)$	1.32	1.6231
Q	$(2i\langle\Gamma^l_{25'} \mid \vec{p} \mid \Gamma_{15}\rangle)$	1.05	1.07
Q'	$(2i\langle\Gamma^u_{25'} \mid \vec{p} \mid \Gamma_{15}\rangle)$	-.807	-.752
R	$(2i\langle\Gamma^l_{25'} \mid \vec{p} \mid \Gamma_{12'}\rangle)$	.830	.8049
R'	$(2i\langle\Gamma^u_{25'} \mid \vec{p} \mid \Gamma_{12'}\rangle)$	1.210	1.4357
T	$(2i\langle\Gamma^u_{1} \mid \vec{p} \mid \Gamma_{15}\rangle)$	1.08	1.2003
T'	$(2i\langle\Gamma^l_{1} \mid \vec{p} \mid \Gamma_{15}\rangle)$	.206	.5323

Table 2.2: Matrix elements of the momentum operator $\vec{p}$ (in atomic units) used in the full-zone $\vec{k} \cdot \vec{p}$ calculations. The alloy properties are calculated by averaging the Si and Ge values. These values were obtained from Reference[17] .

one two-fold representation Γ_{12} and four one-fold representations $\Gamma^u_1, \Gamma^l_1, \Gamma^l_{2'}, \Gamma^u_{2'}$. In Table 2.1 we have given the values used for the zone-center energies in our calculations. The momentum operator $\vec{p} = -i\vec{\nabla}$ is a vector operator and thus belongs to the Γ_{15} irreducible representation of the O^7_h space group (diamond structure). Group theoretical arguments may be used to show that there are only 10 independent momentum matrix elements between the 15 zone-center basis states. In Table 2.2, we have enumerated the values of the momentum matrix elements appropriate for bulk Si and Ge. To represent the strained band structures of Si and Ge accurately, we have slightly modified the zone-center energies given by Cardona and Pollack.[17] The properties of $\mathrm{Si}_{1-x}\mathrm{Ge}_x$ alloys were determined by a linear interpolation of the

$\vec{p}$- matrix elements and the zone-center energies of Si and Ge. In the [001] direction, the 15 × 15 $\vec{k} \cdot \vec{p}$ Hamiltonian can be block-diagonalized into one 5 × 5, three 3 × 3 and one 1 × 1 submatrices. The bottom of the conduction band in the [001] direction (Δ_1^{lc}) is then given by the second largest eigenvalue of the following 3 × 3 matrix

$$\begin{pmatrix} E_{15} + k_z^2 & k_z T & k_z T' \\ k_z T & E_1^u + k_z^2 & 0 \\ k_z T' & 0 & E_1^l + k_z^2 \end{pmatrix} . \tag{2.4}$$

The top of the valence band in the [001] direction (Δ_5^v) is given by the second largest eigenvalue of the following 3 × 3 matrix

$$\begin{pmatrix} E_{25'}^l + k_z^2 & k_z Q & 0 \\ k_z Q & E_{15} + k_z^2 & k_z Q' \\ 0 & k_z Q' & E_{25'}^u + k_z^2 \end{pmatrix} . \tag{2.5}$$

Including the spin-orbit interaction complicates the situation by doubling the size of the Hamiltonian matrix from 15 × 15 to 30 × 30. The spin-orbit interaction in atomic units is given by

$$\frac{\alpha^2}{4} \left(\vec{\nabla} V \times \vec{p} \right) \cdot \sigma, \tag{2.6}$$

where, α is the fine structure constant. When added to the Hamiltonian of Eq. 2.3, this generates two new terms given by

$$\frac{\alpha^2}{4} \left[\left(\vec{\nabla} V \times \vec{p} \right) \cdot \sigma + \left(\vec{\nabla} V \times \vec{k} \right) \cdot \sigma \right] . \tag{2.7}$$

The second term is much smaller than the first term, and will be neglected for the purpose of the present discussion. However, the main effect of the k-independent part of the spin-orbit interaction is to couple one Δ_5^v heavy particle and the $\Delta_{2'}^v$ light particle from the 3 fold degenerate $\Gamma_{25'}^l$ valence band-edge to give the conventional light-hole and spin-orbit bands. The form of the other Δ_5^v heavy particle band remains the same even in the presence of the spin-orbit interaction, and gives rise to the conventional heavy-hole band. This identification of the heavy-hole band with the Δ_5^v band can be made even in the presence of tetragonal strain effects. For most of this work, we have focused our attention on only the heavy-hole band and the longitudinal Δ_1^{lc} ellipsoids of the lowermost conduction bands, since they are the relevant bands for near band gap optical transitions. We have denoted the longitudinal conduction band Δ_1^{lc} by $\mid \Psi_C \rangle$ and the heavy-hole bands Δ_5^v by $\mid \Psi_V \rangle$. In the zone-center representation, both these states are column vectors of 15 elements with only three nonzero components. It is fairly easy to work out the optical matrix elements in this basis set, because the matrix elements of the 15 × 15 momentum operator are known (given in Table 2.2). Our calculations indicate that for [001] superlattices, $\langle \Psi_C \mid \mathrm{p}_z \mid \Psi_V \rangle = 0$, but $\langle \Psi_C \mid \mathrm{p}_x \mid \Psi_V \rangle = \langle \Psi_C \mid \mathrm{p}_y \mid \Psi_V \rangle \neq 0$. Thus, only light polarized in a plane perpendicular to the superlattice growth axis is allowed to induce optical transitions in $Si_{1-x}Ge_x/Si$ superlattices.

2.2.2 Complex Band Structure

To study the band structure of $Si_{1-x}Ge_x/Si$ superlattices, it is necessary to work out the complex band structure of the constituent bulk materials. The bulk Hamiltonian of Equation 2.3 can be viewed as a quadratic function of a scalar parameter k_z involving 15 × 15 matrices. It can be shown that one can recast the problem of finding k_z as an eigenvalue problem with the size of the original Hamiltonian doubled when E and $\vec{k}_{||}$ are specified.[19, 20]

Equation 2.3 can be rewritten as follows,

$$\left[D_0(\vec{k}_{||}, E) + D_1 k_z + k_z^2\right] u_{nk} = 0, \tag{2.8}$$

where

$$D_0 = \left[H_0 + 2\vec{p}_{||} \cdot \vec{k}_{||} + k_{||}^2 - E\right], \tag{2.9}$$

and

$$D_1 = [2p_z]\,. \tag{2.10}$$

We can recast 2.8 into a matrix form

$$\begin{pmatrix} [0] & [I] \\ -[D_0] & -[D_1] \end{pmatrix} \begin{pmatrix} u_{nk} \\ k_z u_{nk} \end{pmatrix} = k_z \begin{pmatrix} u_{nk} \\ k_z u_{nk} \end{pmatrix}, \tag{2.11}$$

where $[I]$ is the 15×15 unit matrix. If we treat the quantities u_{nk} and $k_z u_{nk}$ independently (equivalent to treating Ψ, and $\nabla\Psi$ independently in the Schrödinger equation), then we can solve for the plane wave solutions by diagonalizing the matrix in Equation 2.11.

Our solutions for Equation 2.11 generate 30 bands. Because of the inherent limitations of the $\vec{k} \cdot \vec{p}$ approximation, the bulk band structure is not limited to the first Brillouin zone. In the forbidden energy regions (*e.g.*, band gaps) complex wavevectors are generated. In Figs. 2.1 and 2.2 we show the complex band structure (without spin-orbit interaction) of Si and Ge, in the [100] direction. In the figures, the zero of energy is taken to be the valence band maximum of each material and are denoted by Γ, while the indirect conduction band minima in the [100] direction are denoted Δ. These two figures illustrate that the complex wavevectors of the indirect electrons are described fairly accurately by the one-band model, and that in the forbidden energy regions the complex wavevector has both real and imaginary parts. For complex wavevectors with a nonzero real component, the envelope functions are multiplied by a rapidly varying carrier wavefunction. This rapid oscillation is a characteristic feature of indirect envelope functions, as opposed to smoothly varying envelope functions of Γ electrons in materials such as GaAs.

2.2.3 Superlattice Band Structure

The superlattice band structure is calculated in the multicomponent envelope function approximation. The eigenstates derived from $\vec{k} \cdot \vec{p}$ theory can be propagated from one interface to the other within a given bulk layer. However, to match the wavefunctions across the interface, we need to impose boundary conditions on the

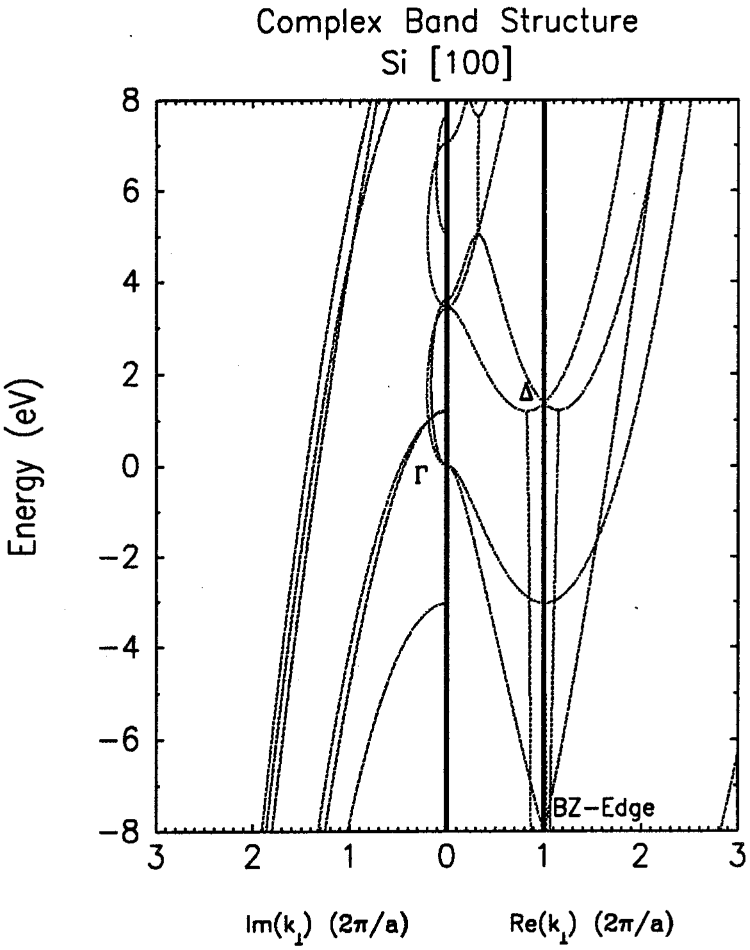

Figure 2.1: Complex band structure of Si in the [100] direction. The zero of energy is at the valence band maximum of Si denoted by Γ. The band structure is obtained using the full-zone $\vec{k}\cdot\vec{p}$ method. The left half of the graph shows the imaginary part of the complex wavevector, while the right half shows the real part. The edge of the first Brillouin zone is at $2\pi/a$. The conduction band minimum in the [100] direction is denoted by Δ.

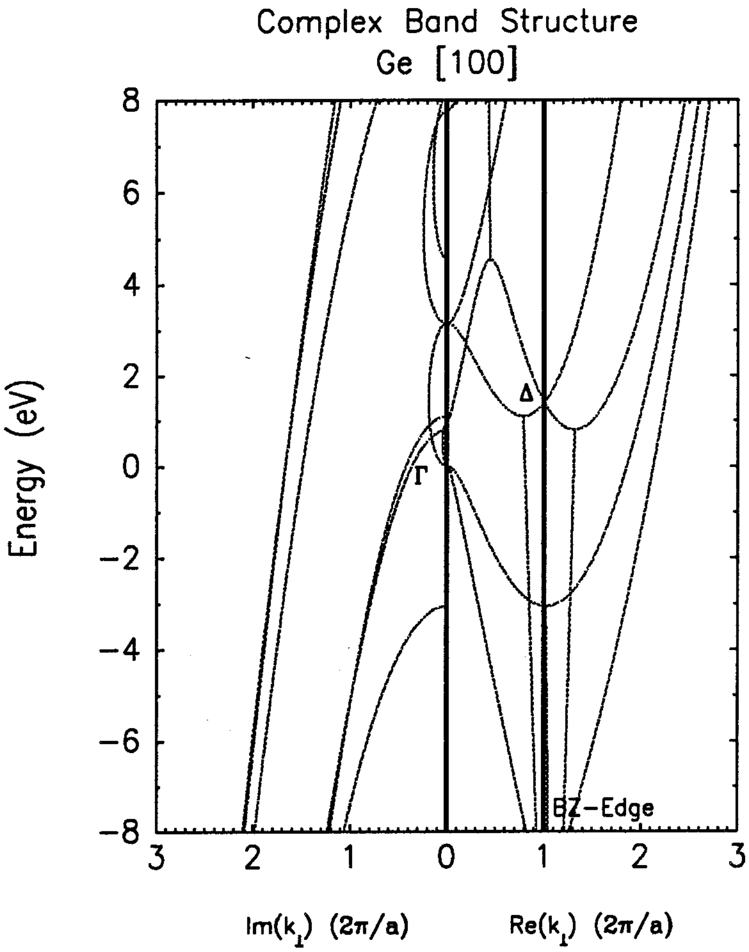

Figure 2.2: Complex band structure of Ge in the [100] direction. The zero of energy is at the valence band maximum of Ge denoted by Γ. The band structure is obtained using the full-zone $\vec{k} \cdot \vec{p}$ method. The left half of the graph shows the imaginary part of the complex wavevector, while the right half shows the real part. The edge of the first Brillouin zone is at $2\pi/a$. The conduction band minimum in the [100] direction is denoted by Δ.

wavefunctions and their normal derivatives. The first matching condition we used was that for each wavefunction, the zone-center components are required to be the same across the interface. This assumption can be justified by the observation that a perfect interface cannot change the symmetry of a zone-center wavefunction; each symmetry component has an equal magnitude on both sides of the interface.[19] However, it is not possible to derive microscopic boundary conditions within the scope of $\vec{k} \cdot \vec{p}$ theory, as described in Section 1.6. The second condition is to require the current carried by each wavefunction to be the same on both sides of the interface. This condition must be satisfied to ensure charge conservation at the interfaces. Finally, we impose the Bloch condition that relates the amplitude of the wave function at a given point in a superlattice unit cell to the amplitude in an adjacent cell at the same corresponding point by a phase factor of the form $e^{iQ(d_1+d_2)}$, where d_1 and d_2 are layer thicknesses within a single period of the superlattice, and Q denotes the superlattice wavevector within the reduced Brillouin zone. The Bloch condition can be cast into an eigenvalue problem whose solution gives the values of the allowed superlattice wavevectors Q, where

$$e^{iQ(d_1+d_2)}\Phi_{nk} = \left[T^{-1}\right]\left[e^{ik_2d_2}\right]\left[T^{1}\right]\left[e^{ik_1d_1}\right]\Phi_{nk}. \tag{2.12}$$

The operator T is the transfer matrix that describes the change in the wavefunction from one semiconductor to the other, and Φ_{nk} is the envelope function composed of linear combinations of plane waves.

It is important to note that in typical calculations of the complex band structure by the $\vec{k}\cdot\vec{p}$ method, the physical solutions are usually accompanied by several unphysical solutions that must be discarded.[19, 20, 21] We identify these unphysical solutions as the energy bands that are purely imaginary or complex in the energy range of interest (-5 eV to +5 eV centered around the top of the valence band-edge). Smith and Mailhiot[19] have shown that the correction terms from these bands are quite small and on the order of 10^{-6} of the leading order terms; we have consistently neglected the contributions to the band structure from these purely imaginary bands. There are other bands that have to be discarded because their real parts do not lie within the first Brillouin zone. These spurious bands result from the inability of the $\vec{k} \cdot \vec{p}$ method to mimic correctly the periodic band structure in the repeated zone scheme with only a finite order polynomial in k_z (30th order polynomial in this case). In our calculations, we neglect these bands based on the analysis by Sterke and Hall[22]. However, in a general situation it is not possible to neglect these bands as discussed in 1.6. Comparisons of calculations done with the tight-binding method and the envelope function method based on GaAs system has shown that the latter is fairly accurate even for ultrathin superlattices.[23] This justifies our application of the envelope function approximation for the study of $Si_{1-x}Ge_x$/Si superlattices with thin layers.

2.3 Strain Effects

Although Si and Ge surfaces are chemically compatible, there is a lattice mismatch between them of $\approx 4.2\%$. Strain therefore plays an important role in determining the relevant band alignments between these two materials. In this section we show how strain effects on the bulk band structure can be calculated by the introduction of phenomenological deformation potentials. If we assume that the epilayers are coherently strained to the buffer-layer, the in-plane lattice constant of the epilayer is constrained to the value set by the buffer, and we can calculate the strain components using macroscopic elasticity theory.

2.3.1 Valence Bands

Kane has shown that the band structure at a three-fold degenerate Γ point can be described by a Hamiltonian

$$H(k_ik_j) = \begin{pmatrix} Lk_x^2 + M(k_y^2 + k_z^2) & Nk_xk_y & Nk_xk_z \\ Nk_xk_y & Lk_y^2 + M(k_x^2 + k_z^2) & Nk_yk_z \\ Nk_xk_z & Nk_yk_z & Lk_z^2 + M(k_x^2 + k_y^2) \end{pmatrix}, \tag{2.13}$$

where L, M and N are reciprocal effective mass parameters. Bir and Pikus[24] have shown that strain effects on the band structure of crystals can be described within the $\vec{k} \cdot \vec{p}$ basis, if a strain-dependent perturbation Hamiltonian that has the same symmetry properties as the quadratic terms in k is added to the unstrained Hamiltonian. If we define the strain tensor ϵ_{ij}, then substituting ϵ_{ij} for k_ik_j, and replacing the reciprocal effective mass parameters by suitable deformation potentials in Equation 2.13 provides an adequate description (to second-order in perturbation theory) of the strain effects in the band structure near degenerate critical points. This procedure yields the strain Hamiltonian

$$H(\epsilon_{ij}) = \begin{pmatrix} l\epsilon_{xx} + m(\epsilon_{yy} + \epsilon_{zz}) & n\epsilon_{xy} & n\epsilon_{xz} \\ n\epsilon_{xy} & l\epsilon_{yy} + m(\epsilon_{xx} + \epsilon_{zz}) & n\epsilon_{yz} \\ n\epsilon_{xz} & n\epsilon_{yz} & l\epsilon_{zz} + m(\epsilon_{xx} + \epsilon_{yy}) \end{pmatrix}, \tag{2.14}$$

where l, m and n are phenomenological deformation potentials. They are related to the familiar deformation potentals[25] a (hydrostatic), b (uniaxial in [100]), and d (uniaxial in [111]) by

$$a = \frac{l + 2m}{3}, \tag{2.15}$$

$$b = \frac{l - m}{3}, \tag{2.16}$$

$$d = \frac{n}{\sqrt{3}}. \tag{2.17}$$

2.3.2 Conduction Bands

Herring and Vogt[29] have shown that the energy shift and splittings of indirect valleys that are due to strain can be described by a uniaxial splitting Ξ_u, and a hydrostatic shift Ξ_d with respect to the unstrained position of the conduction band-edge.[30, 31] The shift in the average energy of the conduction and valence band-extrema is given by

$$\begin{aligned} \Delta E_C^0 &= \left(\Xi_d + \frac{1}{3}\Xi_u\right)(\epsilon_{xx} + \epsilon_{yy} + \epsilon_{zz}), && (2.18) \\ \Delta E_V^0 &= a(\epsilon_{xx} + \epsilon_{yy} + \epsilon_{zz}). && (2.19) \end{aligned}$$

From the above equations, the mean energy gap is obtained to be

$$\Delta E_{Gap}^0 = \left(\Xi_d + \frac{1}{3}\Xi_u - a\right)(\epsilon_{xx} + \epsilon_{yy} + \epsilon_{zz}). \qquad (2.20)$$

For the six-fold degenerate Δ conduction bands of Si, uniaxial strain leaves the degeneracy unchanged. However, under uniaxial strain along [001] and [110] directions, the six-fold degeneracy splits. The splitting with respect to the mean energy of the conduction band is given by

$$\begin{aligned} \{[001], [00\bar{1}]\} &\rightarrow +\frac{2}{3}\Xi_u^\Delta\ (e_{zz} - e_{xx}), && (2.21) \\ \{[100], [\bar{1}00], [010], [0\bar{1}0]\} &\rightarrow -\frac{1}{3}\Xi_u^\Delta\ (e_{zz} - e_{xx}). && (2.22) \end{aligned}$$

For the conduction band minima at the L-point, uniaxial strain along the [001] direction leaves the four-fold degeneracy unchanged. However, under uniaxial strain along the [111] and [110] directions, the four-fold degeneracy will be lifted. The splitting with respect to the mean energy of the conduction band for [111] strain is given by

$$\begin{aligned} \{[111]\} &\rightarrow +2\Xi_u^L e_{xy}, && (2.23) \\ \{[\bar{1}11], [1\bar{1}1], [11\bar{1}]\} &\rightarrow -\frac{2}{3}\Xi_u^L e_{xy}, && (2.24) \end{aligned}$$

Deformation potentials	Si	Ge
$\left(\Xi_d + \frac{1}{3}\Xi_u - a\right)^\Delta$	1.72	1.31
$\left(\Xi_d + \frac{1}{3}\Xi_u - a\right)^L$	-3.12	-2.78
b	-2.35	-2.55
d	-5.32	-5.50
Ξ_u^Δ	9.16	9.42
Ξ_u^L	16.14	15.13

Table 2.3: The table of deformation potentials (in eV) for Si and Ge. The conduction band parameters were obtained from Reference[26] . The valence band parameters were obtained from Reference[28] . Alloy properties were calculated by averaging the Si and Ge values.

and for [110] strain is given by

$$\{[111],[11\bar{1}]\} \rightarrow \frac{2}{3}\Xi_u^L e_{xy}, \tag{2.25}$$

$$\{[\bar{1}11],[1\bar{1}1]\} \rightarrow -\frac{2}{3}\Xi_u^L e_{xy}. \tag{2.26}$$

The values of the deformation potentials used in this work are given in Table2.3.

We have also performed calculations to characterize the strain effects of the (Δ_1^{lc}) conduction bands by introducing deformation potentials for the shifts and the splittings of the zone-center states, $\Gamma_{15}, \Gamma_{2'}^u$, and $\Gamma_{2'}^l$ that constitute the Δ_1^{lc} states as shown in Equation 2.4. We find that it is sufficient to introduce only a uniaxial and a hydrostatic deformation potential for the Γ_{15} triplet, to describe adequately the motion of the six-fold Δ_1^{lc} valleys as a function of strain. Since we have transferred all strain effects into deformation potentials associated with the three-fold degenerate Γ_{15} zone-center states (for the conduction band), with this technique we are able to predict the variation of k_{min} (the minimum of the Δ_1^{lc} band in k-space) as a function of strain. Our calculations indicate that strain does not change k_{min} of the indirect valleys by more than 2-3% of its unstrained value. However, the energies of the Δ_1^{lc} minima are altered substantially by strain effects, as we have discussed.

2.3.3 Structural Effects

Whenever strained epilayers are grown beyond the critical thickness for pseudomorphic growth, it becomes energetically favorable for strain relaxation to occur via formation of misfit dislocations. When this occurs, the in-plane lattice constant of the superlattice will not be constrained to the in-plane lattice constant set by the buffer-layer. It is quite difficult to predict accurately the critical thicknesses, or the degree of strain relaxation in the epilayer. However, experimental studies[32] show that coherently strained epilayers can be grown well beyond the critical thicknesses predicted by equilibrium theories.[33]-[37]

An important case of strain relaxation occurs when the superlattice layers are free to adjust their in-plane lattice constant to the value that minimizes the elastic strain in the superlattice layers. Such a superlattice is called a freestanding superlattice. This situation is quite common and is known to occur when the total thickness of the superlattice exceeds the critical thickness for pseudomorphic growth on the buffer-layer. Experimental studies[32] have shown that in a freestanding superlattice, the lattice-mismatch between the buffer-layer and the in-plane lattice constant of the freestanding superlattice are accommodated by a region rich with misfit dislocations. Beyond a certain distance from the buffer-layer, however, the superlattice has a much lower density of misfit dislocations and exhibits properties related to coherent elastic strain.

The freestanding superlattice in-plane lattice constant is given by

$$a_{\|} = \frac{a_i G_i h_i + a_j G_j h_j}{a_i G_i + a_j G_j}, \tag{2.27}$$

where a_i, and a_j are the cubic lattice constants of the constituents, h_i, and h_j are the layer thicknesses within a single period of the superlattice, and G_i, and G_j are the shear moduli given by

$$G_i = 2(C_{11} + 2C_{12})(1 - D_i/2), \tag{2.28}$$

where D_i are given for the [100],[111], and [110] orientation by

$$D_{100} = \frac{2C_{12}}{C_{11}}, \tag{2.29}$$

$$D_{111} = \frac{2(C_{11} + 2C_{12} - 2C_{44})}{C_{11} + 2C_{12} + 4C_{44}}, \tag{2.30}$$

$$D_{110} = \frac{C_{11} + 3C_{12} - 2C_{44}}{C_{11} + C_{12} + 2C_{44}}. \tag{2.31}$$

The above equations were taken from Van de Walle and Martin[26].

2.4 Band Offsets

The heterojunction band offset for Si/Ge interfaces has been investigated by several groups. Keuch et al.[38] estimated a band offset from reverse bias capacitance measurements of, $\Delta E_V = 0.39 \pm .04$eV. Margaritondo et al.[39] report a valence band offset of 0.2 eV based on photo-emission studies. Mahowald et al.[40] obtain 0.4 ± .1 eV based on the same technique. The theoretical prediction of Harrison[41] places the valence band offset for Si/Ge at 0.38 eV. Tersoff's theory[42] predicts a value of 0.18 eV. The more recent predictions of Harrison and Tersoff[43] sets the valence band offset at 0.29 eV. The above predictions can be in substantial error because there has been no provision for the effects of strain.

However, recent *ab initio* density functional calculations by Van de Walle and Martin[26, 27] have considered the effects of strain on the valence band offsets explicitly. They find that the average positions of the valence band-edges of Si and Ge have an offset independent of strain, $\Delta E_V^{av} \approx 0.54 \pm 0.04$ eV. These values are in agreement with the recent *in situ* measurements by Yu et al.[44] using x-ray photoelectron spectroscopy, explicitly taking into account the effects of strain. Their measurements yielded valence band offset values of 0.83 ± 0.11 eV and 0.22 ± 0.13 eV for Ge on Si (100) and Si on Ge (100), respectively. The value for the average valence band offset between Si and Ge according to the results of Yu et al. is 0.49 ± 0.13 eV.

2.4.1 Conduction Band Offsets

To calculate whether $Si_{1-x}Ge_x$/Si superlattices are direct or indirect, it is necessary to know the conduction band alignments. These can be determined by applying the deformation potential theory developed in the earlier section. In general, the strain distribution in the superlattice will depend on whether the layers are thin enough to be strained coherently to the in-plane lattice constant of the buffer-layer, or whether they will relax to the freestanding superlattice configuration. In this work we have assumed that the epitaxial layers are coherently strained to the in-plane lattice constant set by the buffer-layer.

For epilayers coherently strained to the buffer-layers, the conduction band alignment will depend on both the alloy concentration of the buffer-layer and that of the epilayer. In Figs. 2.3 and 2.4, we show the calculated conduction band offsets for pseudomorphic growth of strained $Si_{1-x}Ge_x$ epitaxial layers on cubic $Si_{1-y}Ge_y$ buffer-layers. The contour plots of 2.3 and 2.4 show the conduction band offset for the 2-fold and 4-fold conduction minima relative to the conduction band minimum of the unstrained buffer-layer. The 4-fold band offsets are relatively small (typically less than 100 meV) for most compositions, while the 2-fold band offsets can be considerably larger (up to approx. 500 meV). The values shown for the conduction band offsets are applicable only for the X-valleys of $Si_{1-x}Ge_x$ alloys. The L-point minima also have a characteristic splitting and a dependence on the alloy composition; these minima are the lowest conduction valleys in alloys with Ge concentrations in excess of $\approx 85\%$.

2.4.2 Type I / Type II Band Alignment

It is possible to achieve both type I and type II band alignments in $Si_{1-x}Ge_x$/Si superlattices, depending on the strain distribution in the epilayers and the layer thicknesses. By a type I band alignment, we mean a situation in which electrons and holes are both confined in the same layer, while in a type II band alignment, electrons and holes are confined in different layers. In a $Si_{1-x}Ge_x$/Si superlattice, the valence bands of the Ge-rich alloy layer will always lie higher in energy than those of the Si alloy layer, and the holes will therefore be confined to the Ge-rich layer. It is not possible to transfer the holes from the Ge-rich layer to the Si-rich layer by strain effects, because the valence band offsets are usually larger than the strain splittings. On the other hand, it is possible to confine electrons in either layer. There is a steady rise of the average conduction band position as the alloy composition is changed from Si to Ge. Thus, electrons can be easily confined in the Si-rich layer, and the usual band alignment of $Si_{1-x}Ge_x$/Si superlattices would be type II. However, it is possible to compressively strain the Ge-rich layer substantially, thereby lowering the strain split conduction band, and transferring the electrons from the Si-rich layer to the Ge-rich layer. This type of band alignment would be type I.

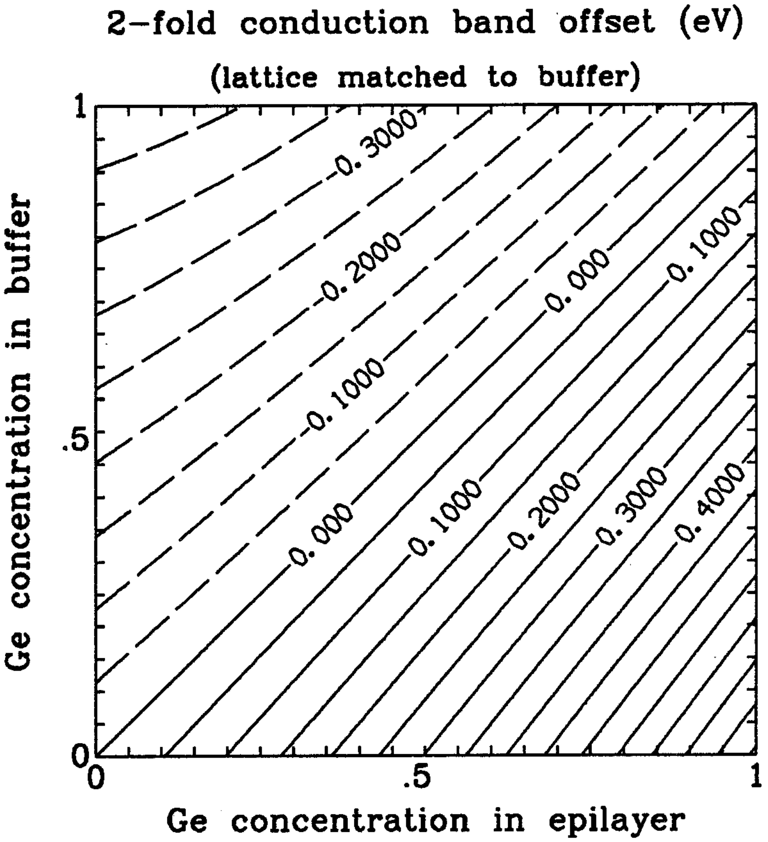

Figure 2.3: The 2-fold conduction band position of a strained $Si_{1-x}Ge_x$ epitaxial layer grown pseudomorphically on an unstrained $Si_{1-y}Ge_y$ buffer-layer. The two-fold bands are the longitudinal ellipsoids of the six Δ-conduction valleys of $Si_{1-x}Ge_x$ alloys. The conduction band offset is measured with respect to the conduction band position of the buffer-layer. The dashed lines mean negative offsets, while the solid lines mean positive offsets.

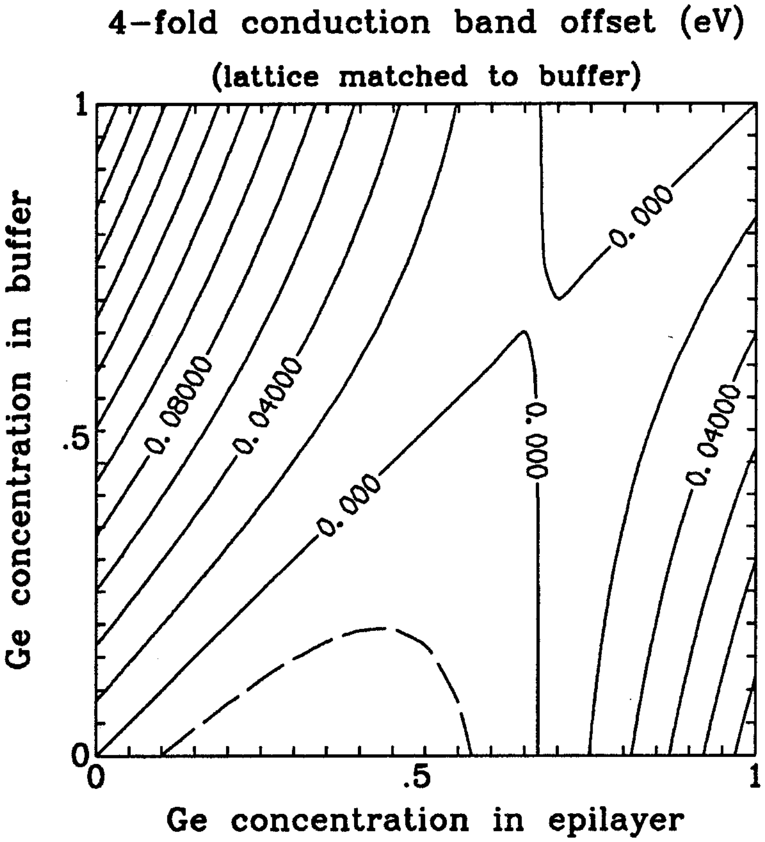

Figure 2.4: The 4-fold conduction band position of a strained $Si_{1-x}Ge_x$ epitaxial layer grown pseudomorphically on an unstrained $Si_{1-y}Ge_y$ buffer-layer. The four-fold bands are the transverse ellipsoids of the six Δ-conduction valleys of $Si_{1-x}Ge_x$ alloys. The conduction band offset is measured with respect to the conduction band position of the buffer-layer. The dashed lines mean negative offsets, while the solid lines mean positive offsets.

2.5 Band Structure of $\mathrm{Si}_{1-x}\mathrm{Ge}_x$/Si Superlattices

The band structure of the lowest conduction band of Si-$\mathrm{Si}_{.5}\mathrm{Ge}_{.5}$ superlattices was calculated using the four bulk states corresponding to $\pm k_{min}\pm\Delta k$; k_{min} is the position of the indirect minimum of the longitudinal conduction band. In our calculations of the superlattice conduction bands, we have neglected the two unphysical bands that arise from the diagonalization of the 6×6 companion matrix constructed as in Equation 2.11, corresponding to the 3×3 Hamiltonian matrix given in Equation 2.4. Similarly, only two bands have been retained for the calculation of the superlattice valence bands, since four of the six complex bands that are generated from the 6×6 companion matrix related to the 3×3 Hamiltonian given in Equation 2.5 are unphysical solutions.

2.5.1 Band Diagram

In Fig. 2.5, we show the conduction and valence band alignments of a Si-$\mathrm{Si}_{.5}\mathrm{Ge}_{.5}$ superlattice grown coherently strained to a $\mathrm{Si}_{.75}\mathrm{Ge}_{.25}$ buffer-layer. This superlattice is the representative case for our band structure and optical matrix element calculations. The positions of the strain-split, conduction band-edges are labeled as two-fold and four-fold conduction bands. The two-fold bands are the longitudinal valleys with large effective masses along the growth direction and $\vec{k}_{||} = 0$. The four-fold bands are the transverse ellipsoids in the x-y plane with $\vec{k}_{||} \neq 0$. The electrons are confined in the Si-rich layer, and the holes are confined in the Ge-rich layer of the superlattice. It is necessary to have tensile strain in the Si-rich layer for the conduction band ground state to be the two-fold states. This can be achieved by growing the superlattice layer coherently strained to a buffer-layer with a larger in-plane lattice constant than the Si-rich well layer. For the case shown in Fig. 2.5, the barrier layers have four-fold electrons as the lowest state, and the two-fold electrons lie higher in energy than the four-fold electrons, because the strain distribution in the barrier layer is opposite to that of the well layer.

We expect no coupling between the two-fold and the four-fold conduction valleys since $\vec{k}_{||}$ is conserved across the interface. Thus, the barrier seen by the two-fold states in going from Si to $Si_{.5}Ge_{.5}$ layers is $\approx$ 300 meV, although the lowest conduction state in the barrier is the four-fold minimum that is only a 150 meV above the Si two-fold states.[27] The heavy longitudinal mass of the two-fold bands result in a confinement energy for the superlattice states of typically less than 100 meV above the bulk band-edge. The four-fold states have smaller effective masses, and the superlattice states that are due to the four-fold states lie higher in energy than the two-fold superlattice states. Thus, we can neglect the presence of the folded four-fold minima for near band gap optical properties, because they correspond to higher conduction band states. Furthermore, one does not expect optical transitions from the four-fold electron states since their $\vec{k}_{||}$ component is not zone-folded to the Γ point.

The heavy-hole, valence band states are confined in the Ge-rich layers. This is because the Ge valence bands on the average lie higher than the Si valence bands. We have shown only the heavy-hole bands, because the light hole bands lie lower in energy than the heavy-hole bands, and do not play a significant role in the near band gap optical absorption.

2.5.2 Intervalley Interference Effect

An interesting feature of the conduction bands of indirect superlattices is that because of the presence of the two longitudinal indirect valleys, the number of allowed solutions is doubled, compared to the conduction band of a direct superlattice such as $Al_xGa_{1-x}As/GaAs$ ($x \leq .4$). Because of the interference between the electrons from the two longitudinal valleys, this additional degeneracy can be split and the lowest

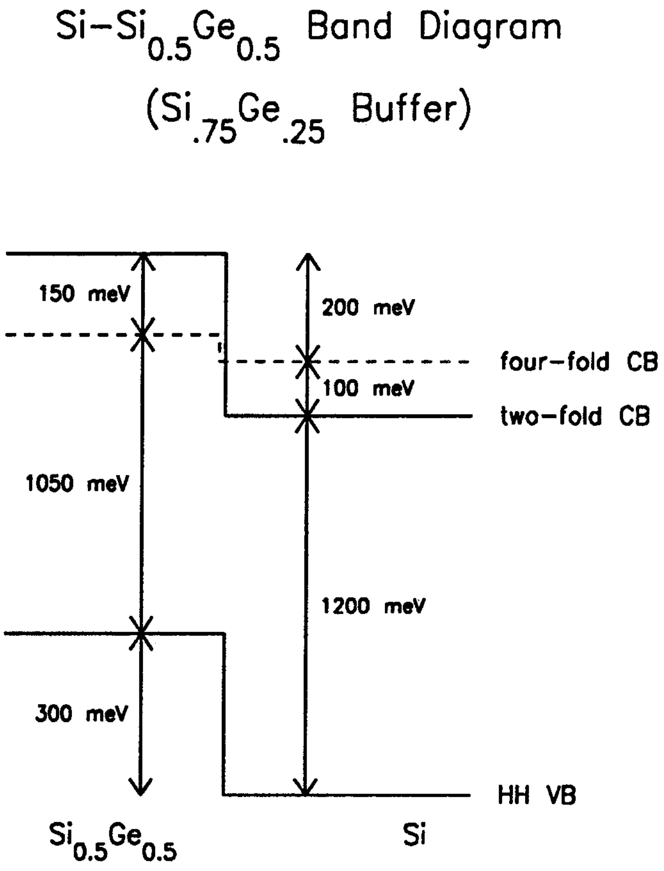

Figure 2.5: Schematic band diagram of a Si-Si$_{.5}$Ge$_{.5}$ heterostructure indicating the relative positions of the two-fold and four-fold conduction bands and the heavy-hole valence bands. Strain distribution is calculated appropriate for pseudomorphic growth on a Si$_{.75}$Ge$_{.25}$ buffer-layer. These band alignments are based on the valence band offset results of Van de Walle and Martin.[26]

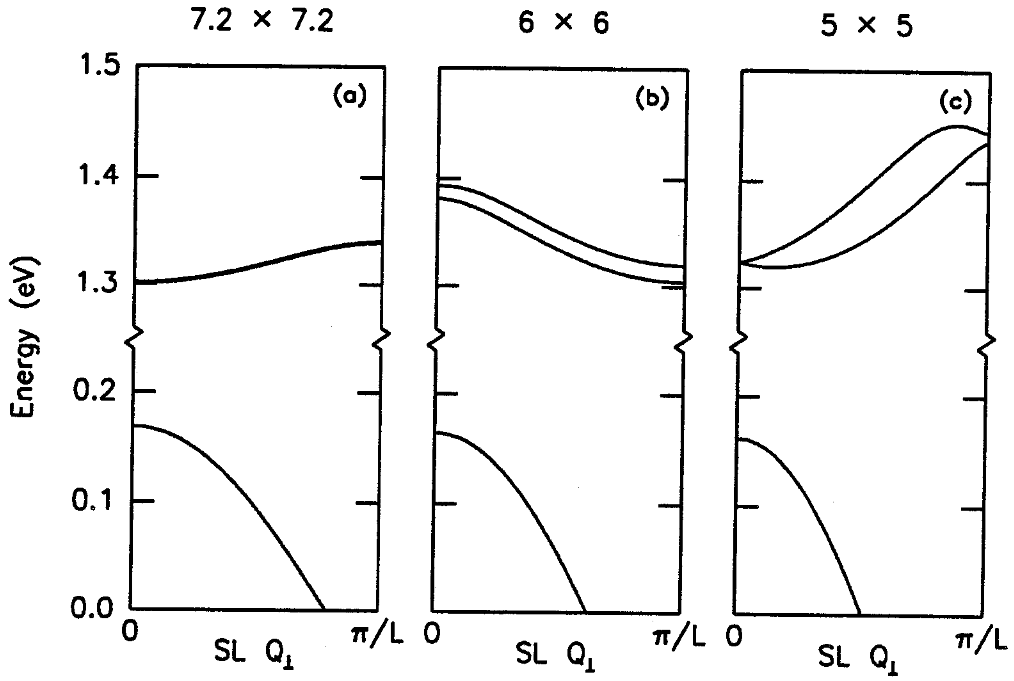

Figure 2.6: Band structure of Si-Si$_{.5}$Ge$_{.5}$ superlattices for three illustrative layer thicknesses. The upper bands correspond to the longitudinal two-fold conduction electrons, and the lower bands correspond to the heavy-holes. Here, SL $Q_\perp$ denotes the superlattice wavevector in the growth direction, and π/L denotes the edge of the reduced Brillouin zone. Notice that a small variation in the layer thicknesses can result in a large variation of the conduction band structure. The conduction band is split into a doublet because of the intervalley interference effect.

lowest conduction band can then become a doublet with a small energy splitting. The actual splitting that is due to the interference effect is quite small (typically less than 10 meV). However, the magnitude of this splitting is a sensitive function of the layer thicknesses and the details of the matching conditions used; the envelope function calculations give smaller interference effects than tight binding calculations.[45] The interference effect in multivalley quantum well structures has been studied by many investigators[45]-[48]. Our predictions of the interference effect in $Si_{1-x}Ge_x$/Si superlattices are in qualitative agreement with the work of Chang and Ting.[45]

The character of the lowest conduction band in $Si_{1-x}Ge_x$/Si superlattices can undergo significant changes for a layer thickness variation of 1-2 monolayers. To illustrate this, in Figs. 2.6(a) 2.6(b), and 2.6(c) we show the superlattice band structure change from a direct gap in Fig. 2.6(a), to an indirect position where the lowest point of the conduction band is pinned at the reduced Brillouin zone edge in Fig. 2.6(b). The superlattices shown in Fig. 2.6 are assumed to be grown along the [001] direction. Our notation of the $n \times m$ superlattice defines a structure with n monolayers of Si, and m monolayers of $Si_{.5}Ge_{.5}$ within a single period. In Fig. 2.6(a) we have shown how a direct superlattice can be achieved with a 7.2 monolayer × 7.2 monolayer superlattice; since a 7×7 superlattice is only approximately direct, it was necessary to use fractional monolayers to achieve an illustrative case of a direct superlattice. However, if the interference effect can be neglected as in a direct material with the same effective mass, then the corresponding superlattice band structure would be a single conduction band at the average position of the lowest two conduction bands shown. In all three sections of Fig. 2.6, we have also shown the band structure of the corresponding heavy-hole state. The dispersion is less for the conduction bands ($\approx$ 100 meV) because of their higher effective masses. However, it should be noted that even when varying the layer thicknesses by a small amount as from 5 to 7 monolayers, the band structure of the superlattice conduction band changes quite significantly, in contrast to the valence band that stays almost the same. This shows that to achieve a given band structure, it is important to control the layer thicknesses to roughly within a monolayer.

2.5.3 Quantum Confinement Effects

The band gap of $Si_{1-x}Ge_x/Si$ superlattices depend on the positions of the heavy-hole state and the lowest conduction state. In Fig. 2.7 we present the the heavy-hole valence band position as a function of the Si and $Si_{.5}Ge_{.5}$ layer thicknesses to illustrate the quantum confinement effects in the valence band. We have assumed that the in-plane lattice constant is that of the $Si_{.75}Ge_{.25}$ buffer-layers. The valence band offset for Fig. 2.7 is $E_V^{Si_{.5}Ge_{.5}}$ - E_V^{Si} = 300 meV. Since the Si layers act as the barrier material for the heavy-hole band, the effect that the Si layer thickness has on the position of the heavy hole band is quite small. Thus the motion of the valence band-edge position is due mainly to the variation of the layer thicknesses of the $Si_{.5}Ge_{.5}$ layers. The zero of energy for the contour lines of Fig. 2.7 is the position of the heavy-hole band of unstrained silicon.

Fig. 2.8 shows the energy of the lowest superlattice conduction band state as a function of the layer thicknesses. The conduction band offset for Fig. 2.8 is $E_C^{Si_{.5}Ge_{.5}}$ - E_C^{Si} = 300 meV. This corresponds to the band offset between the two-fold minima. The zero of energy for the contours of Fig. 2.8 is still the position of the heavy-hole band of unstrained silicon. The bottom of the well (conduction band of Si) lies at 1.2 eV, and the top of the barrier (conduction band of $Si_{.5}Ge_{.5}$) lies at 1.5 eV. Since $Si_{.5}Ge_{.5}$ layers act as the barrier material for the conduction band, the effect of the $Si_{1-x}Ge_x$ layer thickness on the position of the conduction band is quite small; the motion of the conduction band-edge position is due predominantly to the layer-thickness variations of the Si layer. However, notice that the variation in energy for the conduction band states is considerably less than in the case of the valence band

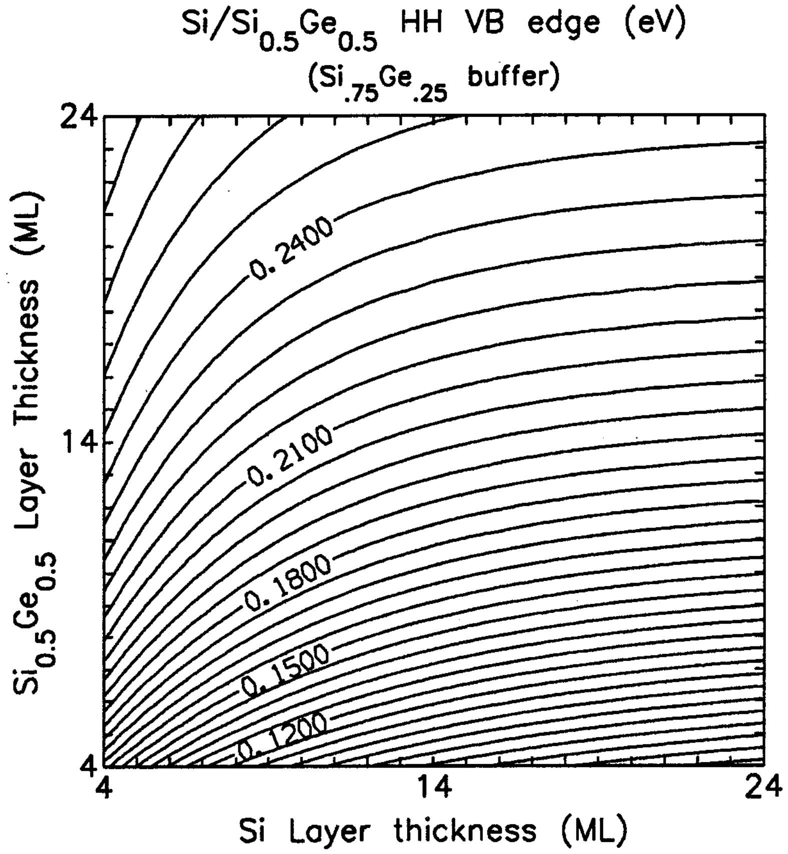

Figure 2.7: Contour plot of the Si-Si$_{.5}$Ge$_{.5}$ superlattice valence band-edge (heavy-hole) position as a function of the layer thicknesses of Si and Si$_{.5}$Ge$_{.5}$ within a single superlattice period. The valence band offset seen by the heavy-holes is assumed to be 300 meV. The strain distribution corresponds to a Si-Si$_{.5}$Ge$_{.5}$ superlattice grown pseudomorphically on a Si$_{.75}$Ge$_{.25}$ buffer-layer. The zero of energy corresponds to the unstrained position of the heavy-hole band-edge of pure Si. (see Fig. 2.5).

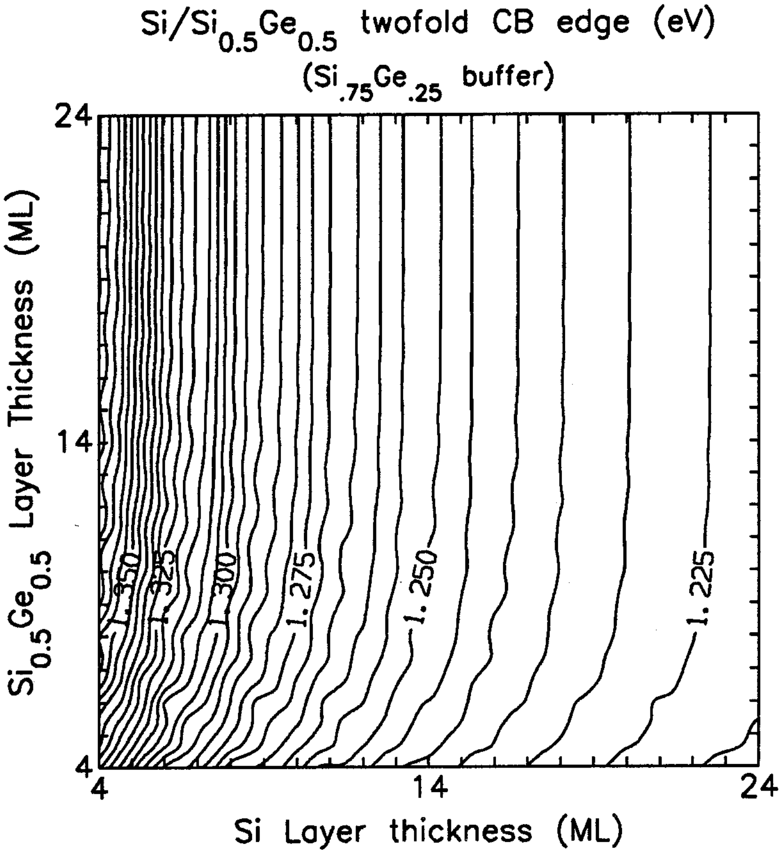

Figure 2.8: Contour plot of the $Si\text{-}Si_{.5}Ge_{.5}$ superlattice conduction band (two-fold) edge as a function of the layer thicknesses of Si and $Si_{.5}Ge_{.5}$ within a single superlattice period. The valence band offset seen by the two-fold states is assumed to be 300 meV. The strain distribution corresponds to a $Si\text{-}Si_{.5}Ge_{.5}$ superlattice grown pseudomorphically on a $Si_{.75}Ge_{.25}$ buffer-layer. The zero of energy corresponds to the unstrained position of the heavy-hole band-edge of pure Si. (see Fig. 2.5).

states of Fig. 2.7. This is because of the larger effective mass associated with the conduction band.

Because of the interference effect, the actual minimum of the lowest conduction band gets shifted up or down in energy depending on the layer thicknesses. This can be seen from Fig. 2.8 as the small oscillations in the contour curves roughly parallel to the lines of constant $k_{min}^{Si}d^{Si} + k_{min}^{Si_{1-x}Ge_x}d^{Si_{1-x}Ge_x}$ (at -45 °C to the axes). It should be noted that as the well (Si layer) width increases, the effects that are due to the interference effect also become smaller. The actual shift in energy that is due to the interference effect typically does not exceed 10 meV, and decreases with the increase in well width as $1/L_W^3$[22], where L_W is the well width within a single repeat of the superlattice.

2.5.4 Direct Gap Superlattices

In a typical situation, the band structure of the $Si_{1-x}Ge_x$/Si superlattice is expected to be indirect. For superlattices to be quasi-direct, a special condition on the layer thicknesses must be satisfied. To a crude approximation, we can derive the condition for quasi-directness by considering the conduction band of the $Si_{1-x}Ge_x$/Si superlattice to be composed of a slowly varying envelope function of the Kronig-Penney form, superimposed on top of a rapidly varying carrier wavefunction that oscillates with wavevector k_{min}^{Si} or $k_{min}^{Si_{1-x}Ge_x}$ in the appropriate layer. To achieve a quasi-direct superlattice, the phase shift of the carrier wave across one SL period should be roughly a multiple of 2π; more precisely, the phase of the carrier wave should cancel with the phase of the envelope function at the end of a superlattice period. Thus we arrive at the approximate relation

$$k_{min}^{Si}d^{Si} + k_{min}^{Si_{1-x}Ge_x}d^{Si_{1-x}Ge_x} \approx 2n\pi, \tag{2.32}$$

as the criterion for direct superlattices. The quantities d^{Si} and $d^{Si_{1-x}Ge_x}$ denote the layer thicknesses, and n is an integer. This simple relation agrees remarkably well with the results of a more complicated analysis based on imposing the Bloch condition on the multicomponent envelope functions.

Although the interference effect leads to only small shifts in energy, it dominates the determination of the position in k-space where the minimum of the folded conduction band occurs. On a contour plot of d^{Si} and $d^{Si_{.5}Ge_{.5}}$, the domain for obtaining quasi-direct superlattices can be expected to be a family of lines obeying Equation 2.32. However, in our model the interference effect gives rise to a width in these lines, thus expanding the domain for obtaining quasi-direct superlattices to a two dimensional subspace of layer thickness space rather than a set of lines. Theoretically, it is possible to achieve an exactly direct superlattice by tailoring the layer thicknesses to lie within one of these two dimensional domains. Precise width of the strips that give rise to direct band structure on a contour plot of d^{Si} and $d^{Si_{1-x}Ge_x}$ is a sensitive function of the matching condition. The problem of achieving exactly direct band structure is only of academic interest. However, in reality, it is adequate to achieve approximately direct superlattices, since transitions are allowed from each point along the folded valence band to the corresponding point in the conduction band. The contour plot of Fig. 2.9 shows the wavevector for the minimum position of the conduction band, based on the matching of the zone-center components across the interface. The lighter regions correspond to approximately direct superlattices. The darker regions correspond to situations when the minimum of the conduction band occurs closer to the reduced zone edge. Fig. 2.9 clearly shows that one obtains quasi-direct superlattices in strips of the layer thickness space as predicted by Equation 2.32. It should also be noted that the superlattice wavevector shown in Fig. 2.9 is in atomic units (1/Bohr). The wavevectors get smaller as the layer thicknesses are increased, since the size of the Brillouin zone is proportional to $\pi/(d^{Si} + d^{Si_{.5}Ge_{.5}})$.

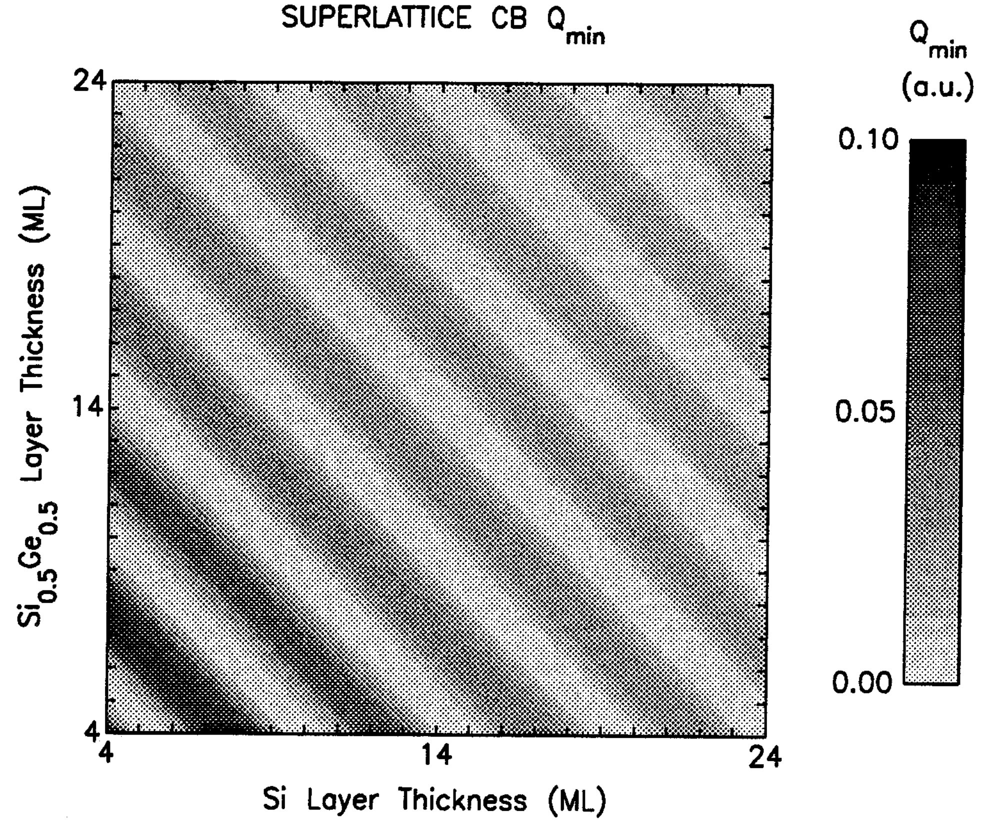

Figure 2.9: Gray-scale plot of Q_{min} (wavevector of the lowest conduction state) as a function of the layer thicknesses of Si and $Si_{.5}Ge_{.5}$ within a single period of the superlattice. Here, Q_{min} is in atomic units. For comparison, the Brillouin zone edges of Si and $Si_{.5}Ge_{.5}$ in the [001] direction have wavevectors 0.612 and 0.587 in atomic units (1/Bohr). The series of light strips correspond to roughly direct band structure, while the darker regions correspond to indirect band structure. This figure shows excellent agreement with the qualitative prediction of Equation 2.32.

2.6 Optical Properties

While a direct band gap is necessary for good optical absorption, it is not sufficient. We also need a finite value for the optical matrix element. In this section, we review the theory of optical absorption for bulk semiconductors and superlattices to illustrate the role of the optical matrix element in optical absorption and emission processes.

The effect of an electromagnetic radiation field on the electronic states of a crystal can be described by a change in the momentum $\vec{p}$ of the electrons according to

$$\vec{p} \rightarrow \left(\vec{p} + \frac{e}{c}\vec{A}\right), \tag{2.33}$$

where e is the absolute value of the electron charge, c is the speed of light, and $\vec{A}$ is the vector potential. The scalar potential can be chosen to be zero without loss of generality, because of the arbitrariness of the gauge. Substituting this result in the kinetic energy term of the Schrödinger equation, and retaining terms to first-order in perturbation theory, we can describe optical interactions by the Hamiltonian

$$H_{op} = \frac{e}{mc}\vec{A} \cdot \vec{p}. \tag{2.34}$$

Here, m is the free-electron mass. In deriving the above expression, we have assumed the Coulomb gauge $\vec{\nabla} \cdot \vec{A} = 0$, and have neglected A^2 terms.[49] Then, we can use Fermi's golden rule to calculate the optical transition rates. If we further ignore the photon momentum ($\vec{k}_{photon} \approx 0$ compared to the electron momentum), and assume a band structure for the semiconductor, then we can write the transition rate as

$$T_{V \rightarrow C} = \frac{2\pi}{\hbar}\left(\frac{eA}{mc}\right)^2 |\langle \Psi_C | \hat{e} \cdot \vec{p} | \Psi_V \rangle|^2 \, \delta(E_C(k_C) - E_V(k_V) - \hbar\omega). \tag{2.35}$$

To obtain the number of transitions per unit time, per unit volume, induced by the radiation field, we must integrate 2.35 over the entire Brillouin zone, sum over the spin degeneracy, sum over all filled bands (V), and sum over all empty bands (C) that can contribute to transitions at energy $\hbar\omega$. The usual expression for the absorption coefficient is the energy absorbed per unit time, per unit volume, divided by the incident energy flux. Using the results of Equation 2.35, we obtain the following form for the absorption coefficient:

$$\alpha(\omega) = \frac{4\pi^2 e^2}{ncm^2\omega} \sum_{C,k_C;V,k_V} |\langle\Psi_C|\hat{e}\cdot\vec{p}|\Psi_V\rangle|^2\, \delta(E_C(k_C) - E_V(k_V) - \hbar\omega), \tag{2.36}$$

where, n is the dielectric constant, and ω is the angular frequency of incident light.

2.6.1 Optical Matrix Element: Bulk

The optical absorption is proportional to the square of the momentum matrix element between the conduction and the valence bands as shown in Equation 2.36. The optical matrix element M_{op} between a valence state of k_V and a conduction state of k_C can be written as

$$M_{op} = \int_L \langle u_C \mid \hat{e}\cdot\vec{p} \mid u_V\rangle \times e^{i(k_V - k_C)z} dz. \tag{2.37}$$

In Equation 2.35, u_C and u_V are the periodic parts of the Bloch functions corresponding to the conduction and valence states. They are cell periodic functions that vary rapidly on a scale smaller than a monolayer, and can be expanded in terms of the zone-center $\vec{k}\cdot\vec{p}$ basis set. Since the representation for the momentum operator in the zone-center basis set is known, the matrix element $\langle u_C \mid \hat{e}\cdot\vec{p} \mid u_V\rangle$ over a unit cell can be easily evaluated. Here u_V and u_C are wavefunctions normalized over a unit cell of the bulk. The resulting expression can then be written as

$$M_{op} = \bar{M}_{op} \int e^{i(k_V - k_C)z} dz, \tag{2.38}$$

where we have taken the rapidly varying $\langle u_C \mid \hat{e}\cdot\vec{p} \mid u_V\rangle$ part outside the integral, and replaced it with its average over a unit cell

$$\bar{M}_{op} = \langle u_C \mid \hat{e}\cdot\vec{p} \mid u_V\rangle. \tag{2.39}$$

The integral in Equation 2.38 becomes a delta function of $(k_V - k_C)$ when integrated over the length of the crystal. This is the familiar k conservation condition for optical transitions between different bands (assuming that photons have negligible k). In bulk Si and Ge, the matrix element between the periodic parts of the Bloch functions $\langle u_C \mid \hat{e} \cdot \vec{p} \mid u_V \rangle$ is nonzero for x and y polarizations for transitions from the top of the valence bands to the [001] conduction valleys. However, the k conservation condition $(k_C = k_V)$ of Equation 2.38 is not satisfied; thus, optical transitions are not allowed in bulk Si and Ge. The motivation for using $Si_{1-x}Ge_x$/Si superlattices is to obtain a direct band structure where this k conservation condition can be modified.

2.6.2 Optical Matrix Element: Superlattice

In a superlattice, Equation 2.37 can be rewritten as

$$M_{op}^{SL} = \int_L \langle U_V(z) \mid \hat{e} \cdot \vec{p}(z) \mid U_C(z) \rangle \times e^{i(k_V^{SL} - k_C^{SL})z} dz, \tag{2.40}$$

where $U_C(z)$ and $U_V(z)$ are the envelope functions that are periodic on the scale of a superlattice unit cell. We can first perform the integral over a unit cell of the superlattice to obtain

$$M_{op}^{SL} = \bar{M}_{op}^{SL} \int_L e^{i(k_V^{SL} - k_C^{SL})z} dz, \tag{2.41}$$

where

$$\bar{M}_{op}^{SL} = \langle U_C(z) \mid \hat{e} \cdot \vec{p}(z) \mid U_V(z) \rangle. \tag{2.42}$$

The envelope functions are normalized to a single unit cell of the superlattice. It is possible to satisfy the $k_V^{SL} = k_C^{SL}$ condition at energies fairly close to the band-edges.

2.6.3 Superlattice Wavefunctions

In Fig. 2.10(a) we have shown the charge density of the wavefunction at the conduction band-edge from the indirect band-edge of a 6 × 6 superlattice. The

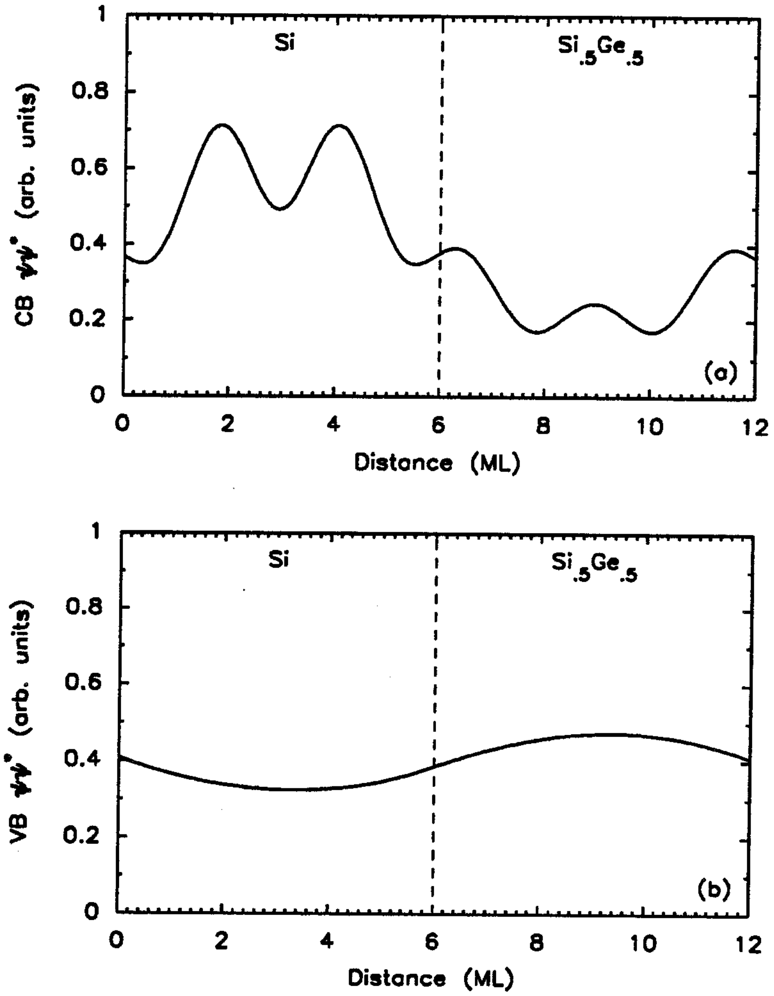

Figure 2.10: The charge density of the superlattice envelope functions corresponding to a 6 × 6 $Si_{.5}Ge_{.5}$ structure. $\Psi\Psi^*$ in the conduction band can have rapid oscillations compared to the valence band. The charge densities were normalized over a superlattice unit cell. The $\vec{p}$ matrix elements between the conduction and valence band wavefunctions can be expected to be quite small, since they have different Fourier components.

conduction band wavefunction is composed of a rapidly varying carrier wave that is superimposed on top of a slowly varying envelope function. The rapid oscillation in the charge density is due to the interference effect between the two longitudinal valleys. On the other hand, the valence band wavefunction is a slowly varying envelope function, as shown in Fig. 2.10(b). Thus, the coupling between these states through the momentum matrix element is quite small. These two wavefunctions have different Fourier components and are still almost orthogonal. Thus, in spite of the band-folding, it is not possible to obtain a large overlap between the conduction and valence wave functions in k-space. In a typical situation, $\bar{M}_{op}^{SL}$ is less than 10^{-2} (atomic units). In comparison to the square of the optical matrix element of bulk GaAs, $| M_{op} |^2 \approx 1.8$ (atomic units)[50], the direct absorption strengths of $Si_{1-x}Ge_x/Si$ superlattices would be expected to be 3-4 orders of magnitude smaller.

2.6.4 Results for $Si_{1-x}Ge_x/Si$ Superlattices

In Fig. 2.11 we have shown the square of the optical matrix element versus the layer thicknesses for the transition from the lowest conduction band state to the corresponding valence band state. The expected matrix elements are quite small, as explained in the previous section. However, the major contribution to the optical matrix element integral comes from the interfaces. Thus, the phase of the conduction band wavefunction at each interface plays an important role in determining this quantity. As seen in Fig. 2.11, we see that changing the layer thickness of either layer by approximately 2-3 monolayers (phase change of π in the wavefunction) can change the absorption strength from the minimum to the maximum value, or vice versa. Thus, the optical absorption strength of $Si_{1-x}Ge_x/Si$ superlattices is a very sensitive function of the layer thicknesses. The maximum optical matrix elements occur for small layer thicknesses, where a large interface-to-volume ratio exists. As the layer thicknesses are increased, the optical matrix elements decrease because the

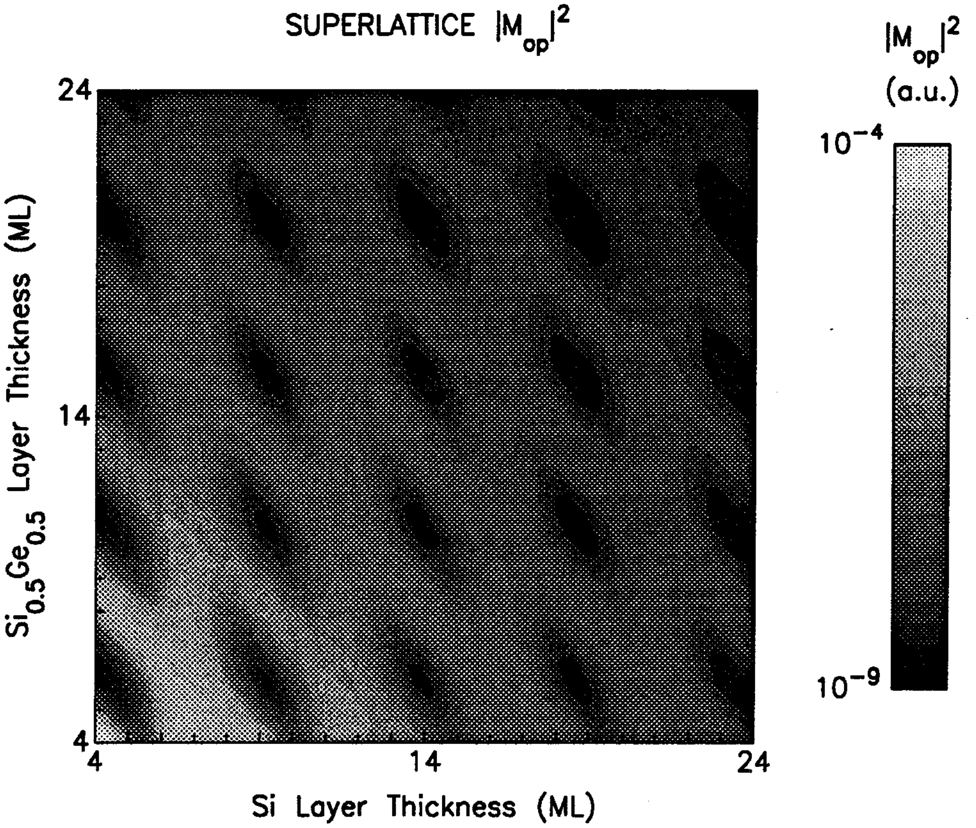

Figure 2.11: Grey-scale plot of $|\bar{M}_{op}|^2$ (square of the optical matrix element) as a function of the layer thicknesses of Si and $Si_{.5}Ge_{.5}$ within a single period of the superlattice. Here, $|\bar{M}_{op}|^2$ is in atomic units. For comparison, bulk GaAs has a $|\bar{M}_{op}|^2$ of 1.86. The darker regions have the enhanced optical matrix elements. In this figure it is clearly seen that layer thickness variations of 1-2 monolayers can change the optical matrix elements by 3-4 orders of magnitude.

interface-to-volume ratio in the superlattice decreases. In the parameter space of 4-24 monolayers, the maximum optical absorption strengths occur near the 7 × 7 $Si_{1-x}Ge_x/Si$ superlattice.

2.7 Conclusions

We have presented a theory for calculating the band structure and optical properties of the $Si_{1-x}Ge_x/Si$ superlattices based on the envelope function approximation. We have shown how the band structure of indirect superlattices such as $Si_{1-x}Ge_x/Si$ can be tailored to obtain roughly direct band gaps by following a simple prescription such as Equation 2.32. The optical absorption strengths associated with these interband transitions can be 3-4 orders of magnitude larger than the phonon-assisted absorption strengths of pure Si or Ge. However, the band-folded states have much weaker optical absorption properties compared to the absorption from direct materials (≈ 3 orders of magnitude lower). It is important to control the layer thicknesses fairly accurately (up to a single monolayer accuracy) to achieve the enhanced optical absorption. Thus, according to our calculations, the usefulness of interband transitions in $Si_{1-x}Ge_x/Si$ superlattices for near infrared applications is rather limited.

References

[1] K. E. Peterson, *Proc. IEEE* **70**, 420 (1982).

[2] S. M. Sze, in *Physics of Semiconductor Devices*, Wiley, New York (1981).

[3] L. Esaki and R. Tsu, *IBM. J. Res. Develop.* **40**, 61 (1970).

[4] R. Hull, J. M. Gibson, and J. C. Bean, *Appl. Phys. Lett.* **46**, 179 (1985).

[5] R. People, J. C. Bean, D. V. Lang, A. M. Sergent, H. L. Stormer, K. W. Wecht, R. T. Lynch and K. Baldwin, *Appl. Phys. Lett* **45**, 1231 (1984).

[6] J. C. Bean, L. C. Feldman, A. T. Fiory, S. Nakahara, and I. K. Robinson,, *J. Vac. Sci. Technol.* **A2**, 434 (1984).

[7] H. M. Manasevit, I. S. Gergis and A. B. Jones, *Appl. Phys. Lett.* **41**, 464 (1982).

[8] E. Kasper and J. C. Bean, in, *Silicon Molecular Beam Epitaxy* , Chemical Rubber, Boca Raton FL (1987).

[9] S. A. Jackson and R. People, *Mat. Res. Soc. Symp. Proc* **56**, 365 (1986).

[10] J. C. Bean, *Mat. Res. Soc. Symp. Proc* **37**, 245 (1985).

[11] M. S. Hybertsen and M. Schluter, *Phys. Rev. B* **36**, 9683 (1987).

[12] S. Satpathy, R. M. Martin, and C. G. Van de Walle, *Phys. Rev. B* **38**, 13237 (1988).

[13] S. Ciraci and T. P. Batra, *Phys. Rev. B* **38**, 1835 (1988).

[14] S. Froyen, D. M. Wood and A. Zunger, *Phys. Rev. B* **37**, 6893 (1988).

[15] G. Bastard, *Phys. Rev. B* **24**, 5693 (1981).

[16] T. P. Pearsall, J. Bevk, L. C. Feldman, J. M. Bonar, J. P. Manaerts, and A. Ourmazd, *Phys. Rev. Lett.* **58**, 729 (1987).

[17] M. Cardona and F. H. Pollack, *Phys. Rev.* **142**, 530 (1966).

[18] J. M. Luttinger and W. Kohn, *Phys. Rev.* **97**, 869 (1955).

[19] D. L. Smith and C. Mailhiot, *Phys. Rev. B* **33**, 8345 (1986).

[20] Y. C. Chang and J. N. Schulman, *Phys. Rev B* **25**, 3975 (1982).

[21] M. F. H. Schuuraman, G. W. 't Hooft, *Phys. Rev. B* **31**, 8041 (1985).

[22] C. M. Sterke and D. G. Hall, *Phys. Rev. B* **35**, 1380 (1987).

[23] J. N. Schulman and Y. C. Chang, *Phys. Rev B* **24**, 4445 (1981).

[24] G. L. Bir and G. E. Pikus, in *Symmetry and Strain-Induced Effects in Semiconductors*, Keter, Jerusalem (1974).

[25] E. O. Kane, *Phys. Rev.* **178**, 1368 (1969).

[26] C. G. Van de Walle and R. M. Martin, *Phys. Rev. B* **34**, 5621 (1986).

[27] C. G. Van de Walle and R. M. Martin, *J. Vac. Sci. Technol. B* **3**, 1256 (1985).

[28] I. Balslev, *Phys. Rev.* **143**, 636 (1966).

[29] C. Herring, and E. Vogt, *Phys. Rev.* **101**, 944 (1956).

[30] H. Hesagawa, *Phys. Rev.* **129**, 1029 (1963).

[31] J. C. Hensel and G. Feher, *Phys. Rev.* **129**, 1041 (1963).

[32] R. H. Miles, T. C. McGill, S. Sivananthan, X. Chu, and J. P. Faurie, *J. Vac. Sci. Technol. B* **5**, 1263 (1987).

[33] J. H. Van der Merwe, *J. Appl. Phys.* **34**, 123 (1963).

[34] C. A. B. Ball and J. H. Van der Merwe, in *Dislocations in Solids*, edited by F. R. N. Nabarro, North Holland, Amsterdam (1983).

[35] J. W. Matthews, in *Epitaxial Growth*, edited by J. W. Matthews, Academic Press, New York (1968).

[36] J. W. Matthews and A. E. Blakeslee, *J. Cryst. Growth* **27**, 118 (1974).

[37] R. People and J. C. Bean, *Appl. Phys. Lett.* **47**, 332 (1985).

[38] T. F. Keuch, M. Mäenpää and S. S. Lau, *Appl. Phys. Lett.* **39**, 245 (1981).

[39] G. Margaritondo, A. D. Katnani, N. G. Stoffel, R. R. Daniels and Te-Xiu Zhao, *Solid State Commun.* **43**, 163 (1982).

[40] P. H. Mahowald, R. S. List, W. E. Spicer and P. Pianetta, *J. Vac. Sci. Technol. B* **3**, 1252 (1985).

[41] W. A. Harrison, in *Electronic Structure and Properties of Solids*, Freeman, San Francisco CA (1980).

[42] J. Tersoff, *Phys. Rev. B* **30**, 4874 (1984).

[43] W. A. Harrison and J. Tersoff, *J. Vac. Sci. Technol.* **4**, 1068 (1986).

[44] E. T. Yu, E. T. Croke, T. C. McGill, and R. H. Miles, *Appl. Phys. Lett.* **56**, 569 (1990).

[45] Y. C. Chang and D. Z. Ting, *J. Vac. Sci. Technol. B* **1**, 435 (1983).

[46] M. Nakayama and L. J. Sham, *Solid State Commun.* **26**, 6 (1978).

[47] L. J. Sham and M. Nakayama, *Surf. Sci.* **73**, 272 (1978).

[48] L. J. Sham and M. Nakayama, *Phys. Rev. B* **20**, 734 (1979).

[49] L. I. Schiff, in *Quantum Mechanics*, McGraw Hill, New York (1955).

[50] C. W. Higginbotham, in *Band Structure and Optical Properties of Semiconductors: The* $\vec{k} \cdot \vec{p}$ *Method*, Thesis, Brown University, RI (1970).

Chapter 3

Intersubband Transitions in Si/Ge Superlattices

3.1 Introduction

In this chapter, we present the theory of intersubband transitions in $Si_{1-x}Ge_x$/Si superlattices. The intent of this study was to investigate the possibility of utilizing intersubband transitions in $Si_{1-x}Ge_x$/Si superlattices for long-wavelength, infrared detection. We make use of the effective mass tensor of $Si_{1-x}Ge_x$/Si superlattices grown along certain orientations to obtain attractive intersubband absorption properties.

3.1.1 Background and Motivation

Infrared detector arrays in the (8-14 μm) region of the spectrum are in great demand for thermal imaging applications. The importance of this wavelength region can be attributed to two reasons. First, this wavelength region is an atmospheric transmission window. Second, the peak of the black-body radiation spectrum from room temperature objects occurs in this wavelength region. The conventional materials of choice for long-wavelength infrared detection have been narrow band gap semiconductors (typically $Hg_{1-x}Cd_xTe$ alloys) and doped semiconductors (extrinsic Si and Ge detectors). Although devices based on $Hg_{1-x}Cd_xTe$ alloys have performed quite well as individual detectors, it has proved difficult to achieve cheap detector arrays with good uniformity and reliability suitable for large array applications. To overcome certain limitations of $Hg_{1-x}Cd_xTe$ alloys, recently, novel structures such as HgTe/CdTe[1] superlattices, $InAs_{1-x}Sb_x$/InSb[2] and InAs/$Ga_{1-x}In_xSb$[3, 4] strained-layer superlattices have been proposed as alternatives.

The infrared detection in the longer wavelength region ($\lambda > 14\mu m$ region) is also of importance for space-monitoring applications, and the conventional detectors of choice at these larger wavelengths have been extrinsic silicon and germanium detectors. However, the extrinsic detectors suffer from the limitation that detection wavelengths are fixed by the positions of the impurity levels in semiconductors. The intersubband approach to infrared detection opens up possibilities for overcomming these limitations and provides an alternative method of detection at these larger wavelengths.[5]-[12] The aim of this chapter is to study the intersubband absorption in $Si_{1-x}Ge_x$/Si superlattices, and to investigate the merits of n-type $Si_{1-x}Ge_x$/Si superlattice infrared detectors.

Superlattice Quantum Well Infrared Detectors

The method of infrared detection with intersubband transitions in doped superlattices as an alternative to the method of interband transitions (across band gap) in narrow band gap semiconductors was proposed by Esaki and Sakaki in 1977.[12] The detection scheme is based on the excitation of an electron from the conduction band ground state to a higher subband, where it can be swept away by a small, applied electric field. It easy to achieve a subband separation energy in the range of 80-160 meV (corresponding to 8-14 μm wavelength region) in the conduction subbands of many semiconductor superlattices. Although this principle of operation is quite similar to that of extrinsic detectors, however, there is the additional advantage of being able to customize the wavelength response by changing the well thicknesses.

To date, the growth technology of choice for such superlattice detectors has been the $Al_xGa_{1-x}As$/GaAs system. These detectors have demonstrated promising quantum efficiencies,[11] and are suitable for large area detector array applications in the 8-14 μm range[7], since planar growth processes such as $Al_xGa_{1-x}As$/GaAs molecular beam epitaxy (MBE) can insure good uniformity over a large area.[13] Because detection is based on intersubband transitions, these structures are efficient at absorbing radiation in a narrow energy band centered around the subband separation energy. Thus, even with moderate doping concentrations ($\sim 10^{12}$ cm^{-2}), large absorption coefficients of 5-10 $\times 10^3$ cm^{-1} can be achieved.[11]

Despite the advantages mentioned above, there are some fundamental limitations to these intersubband infrared detectors, such as poor detectivity. These aspects are analyzed by Kinch and Yariv[14] A serious shortcoming of the $Al_xGa_{1-x}As$/GaAs superlattice infrared detector is that the matrix element for absorption of waves incident normal to the interface (polarization parallel to the plane of the quantum wells) is zero.[5] Although several researchers on $Al_xGa_{1-x}As$/GaAs superlattice detectors have made use of various schemes such as the use of diffraction gratings, fabricating 45 ° facets, etc. to improve the coupling efficiency of normal illumination,[15] however, the usefulness of these detectors could be enhanced by the ability to detect normally incident light. In Fig. 3.1 we illustrate the difference between the two configurations, normal incidence and parallel incidence.

Si based Superlattice Infrared Detectors

The $Si_{1-x}Ge_x$/Si system was proposed by Yang and Pan[16, 17] to overcome the difficulties in $Al_xGa_{1-x}As$/GaAs superlattices associated with the inability to detect

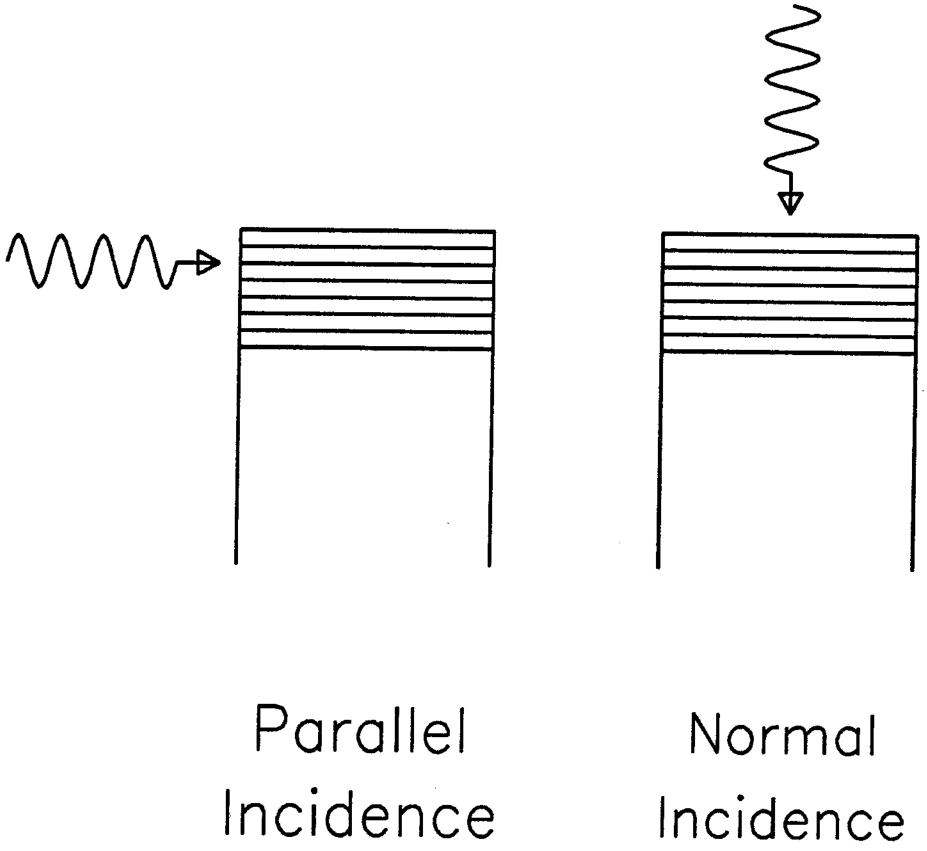

Figure 3.1: This diagram illustrates the configurations of normal incidence and parallel incidence for intersubband absorption in superlattices. One of the advantages of $Si_{1-x}Ge_x/Si$ superlattices is their ability to absorb normally incident light.

normally incident light. This idea is based on the fact that in superlattices composed of indirect materials where the lowest conduction band minima are not oriented along the growth direction, nonzero optical matrix elements can be found for intersubband transitions at normal incidence.[17, 18] To utilize these effects in the $Si_{1-x}Ge_x/Si$ system, however, one must investigate growth in the [111], and [110] directions. In this work, we have investigated the band alignments, optical matrix elements, and absorption strengths of $Si_{1-x}Ge_x/Si$ superlattices, and have quantitatively evaluated their merits for long-wavelength infrared detection.

A $Si_{1-x}Ge_x/Si$ based detector technology would have the additional advantage, compared to the $Al_xGa_{1-x}As/GaAs$ system, of compatibility with existing Si-based read-out devices. In recent years, advances in strained-layer $Si_{1-x}Ge_x/Si$ heteroepitaxy by MBE have shown that high-quality $Si_{1-x}Ge_x/Si$ superlattices can be grown with good uniformity.[19] In principle, it is easy to extend the $Al_xGa_{1-x}As/GaAs$ superlattice infrared detector concept to apply to the $Si_{1-x}Ge_x/Si$ system.

3.1.2 Summary of Results

The main result of this chapter is the calculation of the absorption coefficients for intersubband transitions in $Si_{1-x}Ge_x/Si$ superlattices grown in the [100], [111], and [110] directions to evaluate quantitatively the merits of this system for detection of infrared radiation. We calculate the intersubband absorption in $Si_{1-x}Ge_x/Si$ superlattices, adequately accounting for the strain effects,[20, 21] and using realistic conduction band offsets.[22] We find that finite-barrier heights and strain effects can significantly alter the character of the intersubband absorption. The motivation for studying [100] oriented $Si_{1-x}Ge_x/Si$ superlattices was to compare absorption strengths directly with those of [100] $Al_xGa_{1-x}As/GaAs$ superlattices. $Si_{1-x}Ge_x/Si$ superlattices grown on [111] and [110] orientations were studied because they offer the possibility of obtaining large optical absorption strengths for normal, as well as parallel incidence, making their intersubband absorption properties superior to those of $Al_xGa_{1-x}As/GaAs$ superlattices.

3.1.3 Outline of Chapter

In Section 3.2 of this chapter, we discuss the theory of intersubband absorption in superlattices. We analyze the specific dependence of the optical absorption coefficient on the reciprocal effective mass tensor, and the polarization of the incident radiation. In Section 3.3, we analyze the conduction band alignment of $Si_{1-x}Ge_x/Si$ superlattices for favorable intersubband absorption. We have used the extra degree of freedom offered by strain effects to vary the strain-dependent, conduction band positions, thereby obtaining attractive band lineups for intersubband transitions. We have also selected four cases for detailed study. In Section 3.4, we present absorption coefficients and peak-absorption wavelengths for the four selected cases, as functions of well and barrier thicknesses. Section 3.5 concludes the chapter.

3.2 Theory of Intersubband Transitions

In this section, we outline the basic elements of the theory of intersubband transitions in semiconductor superlattices. We have focussed on the intersubband absorption properties that allow absorption at normal incidence, because of the tensor-effective mass in $Si_{1-x}Ge_x/Si$ superlattices. Several other issues intimately related with the calculations of absorption coefficients, such as band offsets and strain effects, have been treated in depth in Section 2.3; these topics will receive little attention in this chapter.

3.2.1 Absorption

In this section we analyze the optical absorption in a superlattice that is due to electron transitions between the first and the second conduction subbands. The absorption coefficient is given by[23]

$$\alpha(\omega) = \frac{4\pi^2 e^2}{n_o m^2 c\omega} \sum_{n'k',nk} |\langle \psi_{n'k'}|\hat{e}\cdot\vec{p}|\psi_{nk}\rangle|^2 \delta(E_1 - E_2 + \hbar\omega). \qquad (3.1)$$

Here, m is the free-electron mass, e is the electron charge, ω is the angular frequency of the incident light, n_o is the refractive index at the wavelength of incident light, and ψ_{nk} and $\psi_{n'k'}$ are the initial-state and final-state electron wavefunctions, respectively. We have denoted the bulk band indices by the labels n and n', and the electron wavevectors by k and k'. Thus, intersubband transitions occur when n=n'. This expression must be summed over all the bands that contribute to the transition. The vector $\hat{e}$ denotes the polarization direction of the incident radiation, and $\vec{p}$ denotes the momentum operator. If the above matrix element is evaluated by writing each of the wavefunctions as a product of a periodic Bloch function and a slowly varying envelope function, one then, by taking into account the change in the Bloch function away from the center of the critical point (the Δ-minimum in the case of Si) and restricting the analysis to intersubband transitions, recovers a simple expression for the matrix element based on the effective mass. The derivation of this result is quite similar to the proof of the effective mass theorem given by Luttinger and Kohn.[24]

For the rest of this chapter, we assume without loss of generality that the growth axis is always denoted by the z axis. We can then rewrite the matrix element for intersubband transitions as

$$\langle \psi_{nk'}|\hat{e}\cdot\vec{p}|\psi_{nk}\rangle = \left\langle F_{k'}(z)|\hat{e}_i \left(\frac{1}{m^*}\right)_{iz} p_z|F_k(z)\right\rangle. \qquad (3.2)$$

In Equation 3.2, $(1/m^*)_{ij}$ are the components of the dimensionless, reciprocal, effective mass tensor. Summation over repeated indices is assumed in the usual fashion.

$F_k(z)$ and $F_{k'}(z)$ denote the envelope functions of the first and second conduction subbands, respectively. Using Equation 3.2, we can rewrite Equation 3.1 as

$$\alpha(\omega) = \frac{4\pi^2 e^2 \hbar^2}{n_o m^2 c\omega} \int |\langle F_{k'}(z) \nabla_z F_k(z) \rangle|^2 \left(\frac{\hat{e}_x}{m^*_{xz}} + \frac{\hat{e}_y}{m^*_{yz}} + \frac{\hat{e}_z}{m^*_{zz}}\right)^2 \frac{d^3k}{4\pi^2} \delta(E_1 - E_2 + \hbar\omega). \tag{3.3}$$

From Equation 3.3, it is easy to see that nonzero absorption strengths for normal incidence ($\hat{e}_x,\ \hat{e}_y \neq 0; \hat{e}_z = 0$) can be achieved only when $(1/m^*)_{xz}$ or $(1/m^*)_{yz}$ are nonzero. This occurs when the growth direction is misaligned with respect to the principal axes of the ellipsoidal valleys.

If we denote the sheet-doping concentration per superlattice layer by N_S, then, assuming a zero temperature, two-dimensional Fermi distribution and assuming that the envelope function matrix element is independent of $\vec{k}_{||}$ and $\vec{k}_{\perp}$, we can evaluate the integral over $dk_x dk_y$ (parallel to the superlattice planes). We can also write the delta function in the above Equation 3.3 as a normalized Lorentzian with a broadening parameter Γ, to account for the excited state lifetime τ (given by $\Gamma = \hbar/\tau$). The expression for $\alpha(\omega)$ then becomes

$$\begin{aligned} \alpha(\omega) &= \frac{4\pi e^2 \hbar^2}{n_o m^2 c\omega} |\langle F_2(z) \nabla_z F_1(z) \rangle|^2 \left(\frac{\hat{e}_x}{m^*_{xz}} + \frac{\hat{e}_y}{m^*_{yz}} + \frac{\hat{e}_z}{m^*_{zz}}\right)^2 N_S \\ &\quad \times \int_0^{\pi/L} \frac{(\Gamma/2\pi) dk_z}{(\hbar\omega - E_{12}(k_z))^2 + \Gamma^2/4}. \end{aligned} \tag{3.4}$$

Here, L is the length of a period of the superlattice, and $E_{12}(k_z)$ is the subband separation energy. Equation 3.4 shows that absorption is proportional to the sheet-doping concentration N_S. Furthermore, if there is only a very small amount of dispersion in $E_{12}(k_z)$, then $\alpha(\omega)$ is inversely proportional to the bandwidth Γ and superlattice period L. In the actual calculations reported in this chapter, we have retained the dependence of the matrix element on $k_{||}$ and $k_{\perp}$, as in Equation 3.3. However, we have assumed a zero-temperature Fermi distribution, and a broadening parameter Γ of 8 meV. We have also assumed a sheet-doping concentration of 10^{12} cm^{-2} in our calculations. In Fig. 3.2 we show the intersubband absorption coefficient for normally incident light in a [110] oriented superlattice as a function of wavelength. The purpose of this figure is to illustrate that intersubband absorption occurs in a narrow energy band.

An interesting fact of the intersubband absorption in superlattices is that absorption coefficients can increase as a function of peak wavelength for certain layer thickness regions. The intersubband matrix element can increase as the well thickness is increased because of the possible improvement in the confinement of the second excited state. However, as the well thickness is increased, the separation between the ground state and the excited state decreases, resulting in a peak absorption at longer wavelengths. Thus, the net effect is to produce an increase in the absorption coefficient at larger peak wavelengths.

This behavior is qualitatively different from the interband absorption situation in narrow band gap semiconductors, and can be quoted as a potential advantage of the intersubband absorption for longer-wavelength infrared detection. This fact is illustrated in Fig. 3.3. For the purpose of the figure, we have selected the parallel absorption of $Si_{0.7}Ge_{0.3}$ /$Si_{0.2}Ge_{0.8}$ superlattices grown coherently strained to a $Si_{0.7}Ge_{0.3}$ buffer-layer. This particular case will be discussed in detail later in Section 3.4.2. The curve in Fig. 3.3 was generated by keeping the barrier thickness constant at 50 monolayers, and varying the well thickness. In Fig. 3.3 we assumed a doping concentration equivalent to 10^{18} cm^{-3} in the bulk. This figure clearly indicates that the absorption coefficient increases as the peak wavelength is increased in the range 20-27 μm.

3.2.2 Band Structure Calculations

In our calculations, we first study the band structure of the $Si_{1-x}Ge_x$ host layers using full-zone $\vec{k}\cdot\vec{p}$ theory.[25, 26] We obtain alloy parameters by averaging the input $\vec{k}\cdot\vec{p}$ parameters for Si and Ge. A more detailed description of the band structure

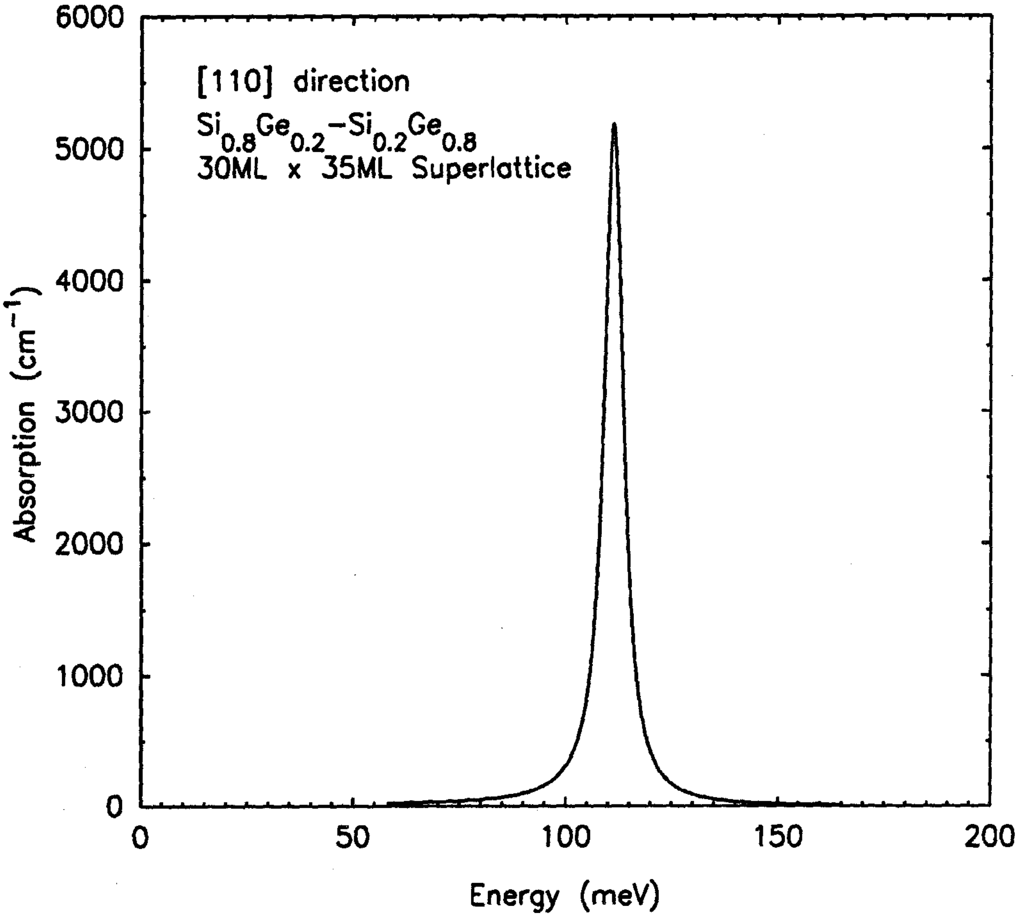

Figure 3.2: This figure shows the intersubband absorption coefficient at normal incidence in a [110] oriented $Si_{1-x}Ge_x$/Si superlattice as a function of wavelength. The layer thicknesses were picked to give a peak in the absorption near 11 microns. The width of the peak is determined by the broadening parameter Γ defined in the text.

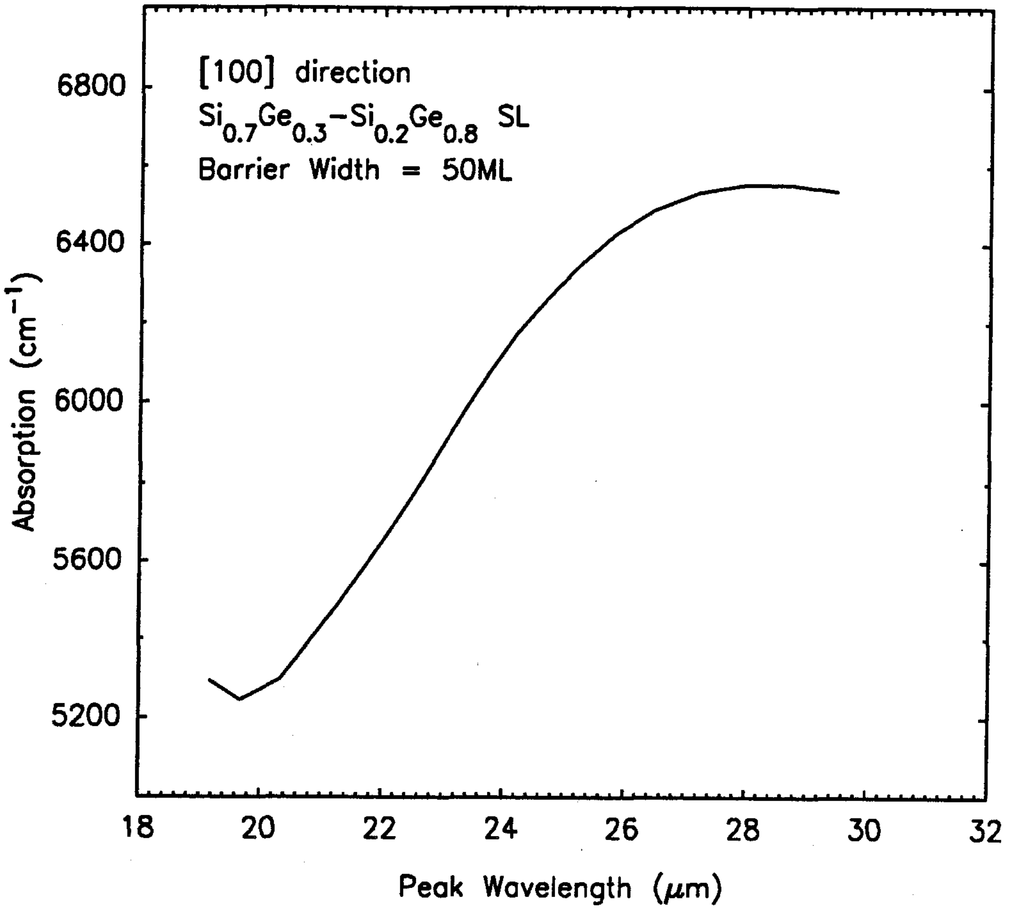

Figure 3.3: This figure shows the peak intersubband absorption coefficient at parallel incidence in [100] oriented $Si_{0.7}Ge_{0.3}$ /$Si_{0.2}Ge_{0.8}$ superlattices as a function of peak wavelength. The purpose of the figure is to illustrate that under certain situations, it is possible to obtain an increase in the intersubband absorption coefficient versus the of peak wavelength. We have assumed that the barrier thickness is fixed at 50 monolayers, while the well thickness is varied. The results are based on a doping concentration equivalent to 10^{18} cm^{-3} in the bulk.

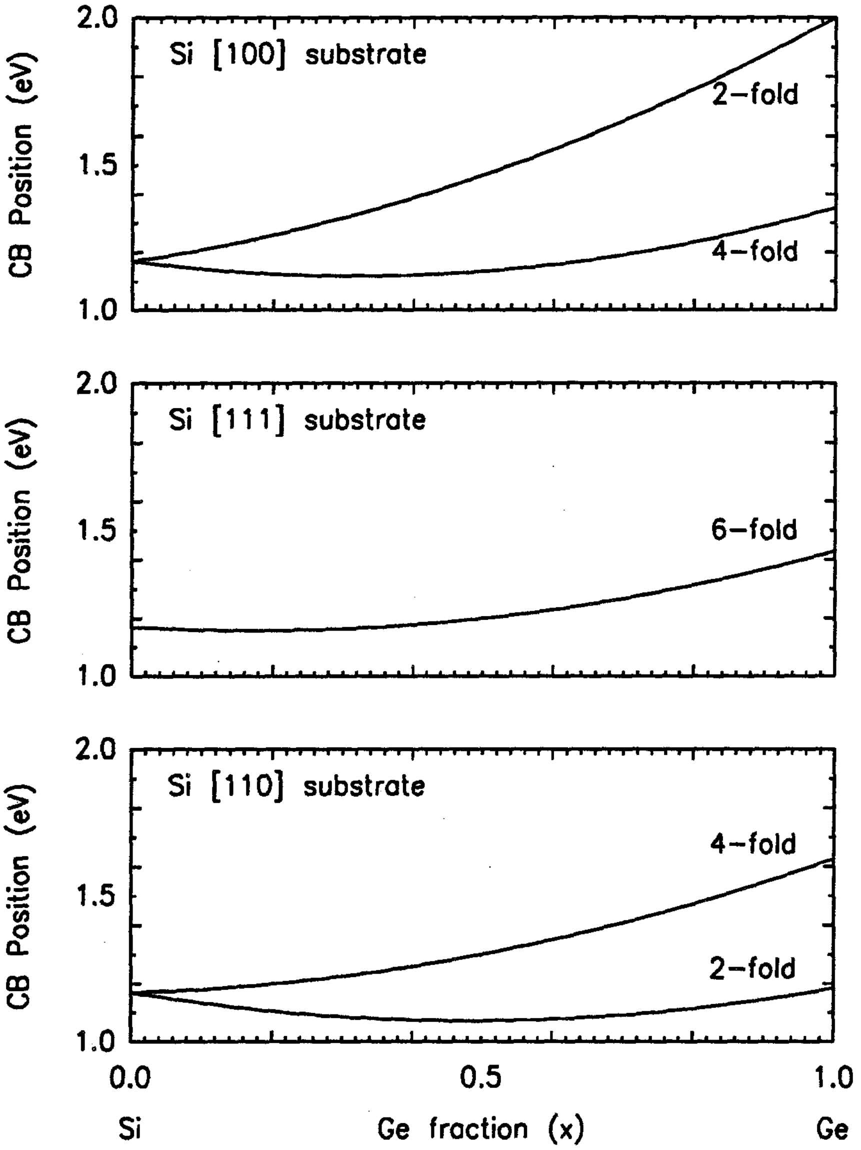

Figure 3.4: The variation of the conduction band positions of the strain split Δ conduction valleys of coherently strained $Si_{1-x}Ge_x$ epilayers grown on Si buffer-layers. The results are presented for [100], [111], and [110] growth orientations.

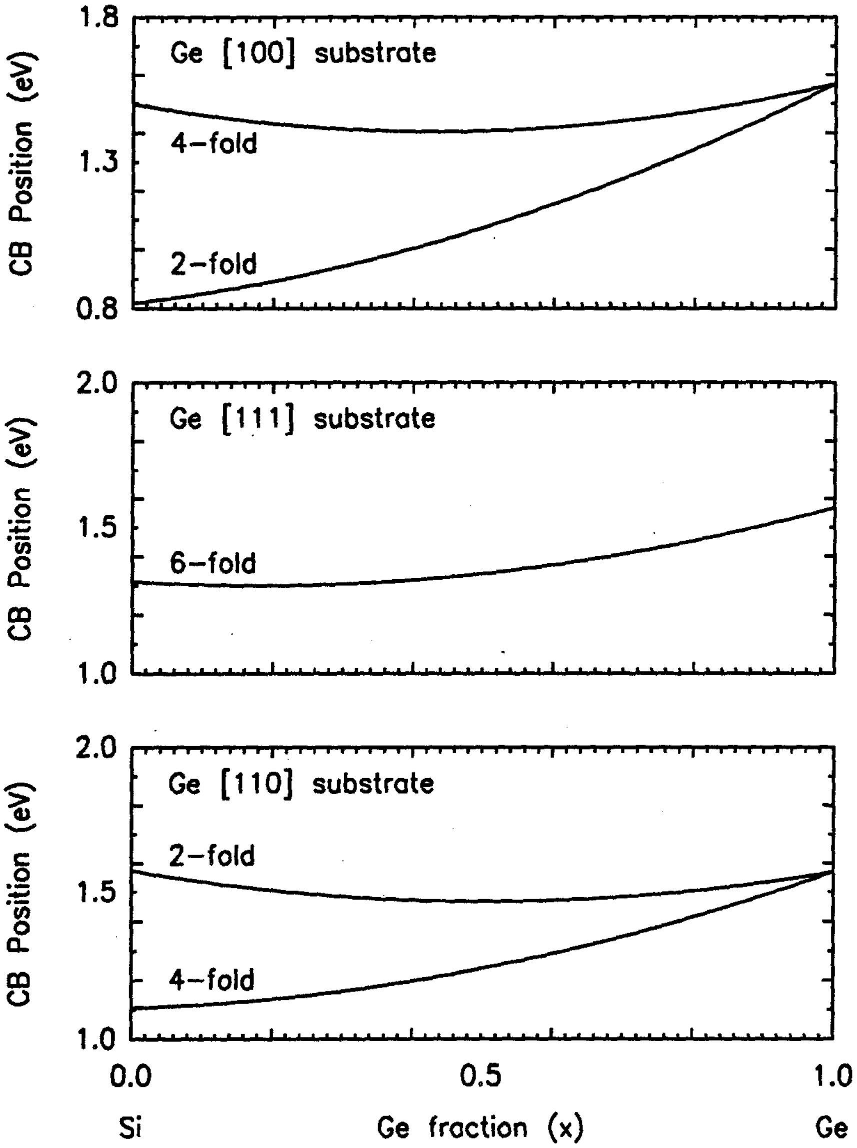

Figure 3.5: The variation of the conduction band positions of the strain split Δ conduction valleys of coherently strained $Si_{1-x}Ge_x$ epilayers grown on Ge buffer-layers. The results are presented for [100], [111], and [110] growth orientations.

as a function of strain; our calculations of the strain dependence of the band-edge positions are in close agreement with those of Van de Walle and Martin.[22, 27] A more detailed discussion of strain effects in $Si_{1-x}Ge_x$/Si superlattices is given in Section 2.3.[32]

The position of the conduction band-edge depends on the distribution of strain in the epilayer. We assume that the entire superlattice structure is coherently strained to the buffer-layer; this assumption is valid if the epitaxial layers do not exceed the critical thickness for pseudomorphic growth.[33, 34] In order to satisfy this condition, we have limited our structures to contain only layers thinner than 60 monolayers, and the maximum difference in alloy concentration that we allow across an interface is 60%, corresponding to a lattice-mismatch of less than 2.4%.

Figs. 3.4 and 3.5 show the strain split Δ conduction band minima for $Si_{1-x}Ge_x$ epilayers grown on Si and Ge buffer-layers, respectively. The zero of energy is the position of the unstrained valence band maximum of Si. For growth on [100] buffer-layers, the conduction bands are split into two-fold longitudinal and four-fold transverse valleys. For [111] growth, the six-fold degeneracy of the Δ conduction band minima is not broken. For [110] growth, the conduction bands are again split into two-fold transverse valleys, and four-fold valleys tilted 45 ° to the growth axis.

3.3 Favorable Band Alignments

In this chapter, we consider four detailed examples of intersubband absorption in $Si_{1-x}Ge_x$/Si superlattices. The first and second examples are intersubband absorption coefficients at parallel incidence in [100] oriented $Si_{1-x}Ge_x$/Si superlattices. The third and fourth examples are intersubband absorption coefficients at normal incidence in [111] and [110] oriented $Si_{1-x}Ge_x$/Si superlattices. In this section we describe the reasons for selecting these configurations, and explain how the most favorable band alignments can be obtained by consideration of the strain effects.

3.3.1 Parallel Incidence

We have selected two examples to illustrate the difference in the nature of the intersubband absorption properties of the two-fold and four-fold electrons for superlattices grown in the [100] direction. The two-fold electrons are confined by large conduction band offsets favoring large, intersubband matrix elements. However, they also have a large effective mass, favoring smaller absorption coefficients. On the other hand, the four-fold electrons have a small effective mass favoring large absorption coefficients, while they are not confined by large conduction band offsets, thus, giving rise to small matrix elements. In a given situation, whether the two-fold electrons or the four-fold electrons are more favorable for intersubband absorption cannot be determined without further calculation. In our analysis, we have selected representative situations corresponding to each of these cases.

The first case we examine is the absorption from two-fold longitudinal electrons in [100] $Si_{1-x}Ge_x$/Si superlattices. Fig. 3.5, shows that the ground state will be the two-fold valleys for superlattices consisting of Si-rich well layers, and Ge-rich barrier layers, coherently strained to a Ge-rich [100] buffer-layer. The variation of the two-fold band-edge position as a function of the alloy composition is quite large for the [100] growth direction, making it easy to achieve large conduction band offsets.

The second case of interest is the absorption from four-fold transverse electrons in [100] $Si_{1-x}Ge_x$/Si superlattices. From Fig. 3.4, we see that the four-fold states would be lowest when the superlattice consists of Si-rich well layers and Ge-rich barrier layers, coherently strained to a Si-rich [100] buffer-layer. However, it is difficult to achieve a significant conduction band offset for these four-fold states. In order to obtain the maximum barrier heights, the composition of the well layer should be at the minimum of the band-bowing region ($\approx$ 30% Ge concentration) of the four-fold conduction band of Fig. 3.4.

3.3.2 Normal Incidence

The next two cases were selected to illustrate the difference in the nature of the intersubband absorption properties of the [111] and [110] orientations. These two orientations have slightly different effective masses (smaller mass in the [111] orientation), and slightly different conduction band offsets (larger offset in the [110] orientation). Thus, in a given situation, whether the [111] orientation or the [110] orientation is more favorable for intersubband absorption cannot be determined without further calculation. In our analysis, we have selected representative situations from each of these orientations.

The third case we study is that of [111] $Si_{1-x}Ge_x$/Si superlattices. The six-fold degeneracy of the Δ conduction band minima is not broken for growth in the [111] direction. In order to achieve the maximum barrier heights, we pick a well layer close to the minimum of the slight band bowing region of Fig. 3.5 ($\approx$ 20% Ge concentration), and a Ge-rich barrier layer ($\approx$ 80% Ge concentration). The choice of the buffer-layer is not critical since strain effects shift all the valley positions equally.

The fourth case we consider is that of [110] oriented $Si_{1-x}Ge_x$/Si superlattices. For [110] growth, strain effects split the conduction bands into two-fold and four-fold components. In this case, however, the four-fold states are ellipsoids oriented at 45° to the growth axis, and the two-fold states are transverse ellipsoids. The four-fold states are the more interesting ones, showing the possibility of absorption at normal incidence. A four-fold ground state can be achieved in a structure in which Si-rich well layers and Ge-rich barrier layers are grown coherently strained to a Ge-rich buffer-layer as indicated in Fig. 3.5.

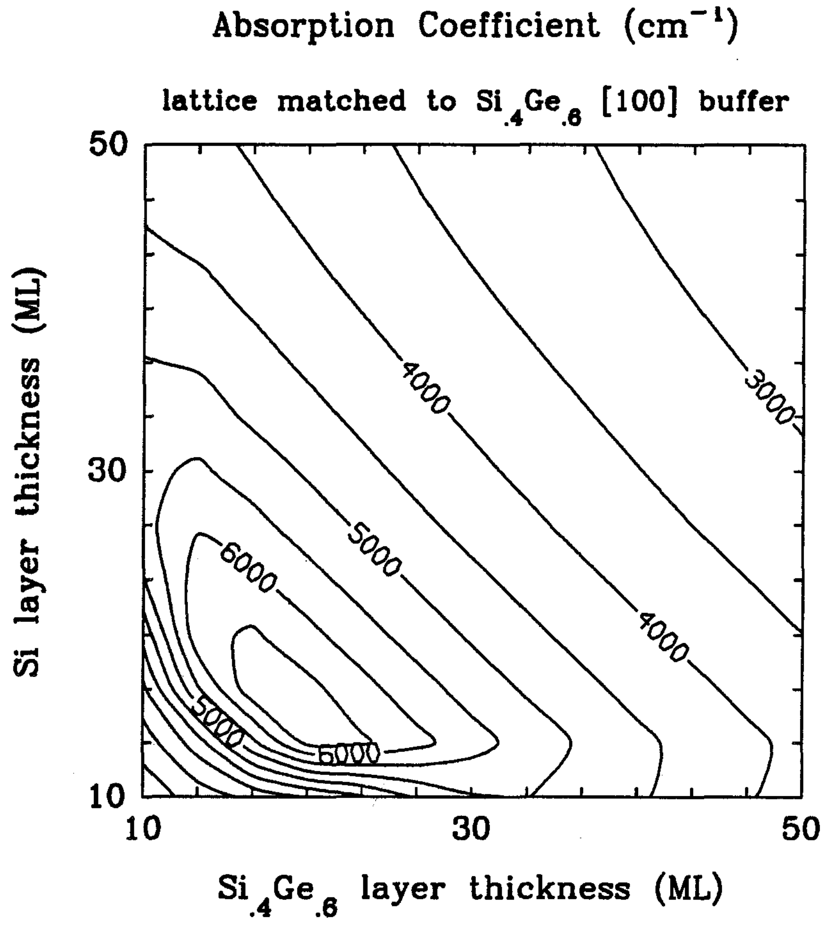

Figure 3.6: Absorption coefficients for light at parallel incidence for a [100] Si/Si$_{0.4}$Ge$_{0.6}$ superlattice. In this case, the two-fold longitudinal conduction valleys are in the ground state. The superlattice is assumed to be coherently strained to a Si$_{0.4}$Ge$_{0.6}$ buffer-layer. The contour lines show the variation of the absorption coefficient as a function of the Si well thickness and the Si$_{0.4}$Ge$_{0.6}$ barrier thickness. The layer thicknesses are measured in monolayers, denoted by ML in the figure.

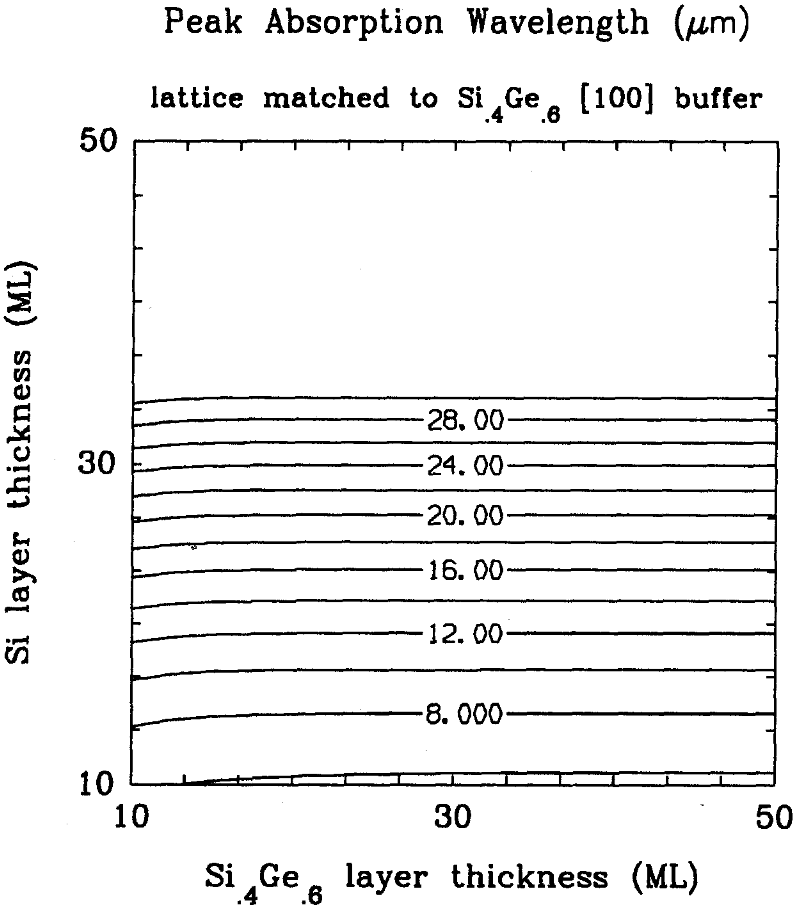

Figure 3.7: Peak absorption wavelengths for light at parallel incidence for a [100] Si/$Si_{0.4}Ge_{0.6}$ superlattice. In this case, the two-fold longitudinal conduction valleys are in the ground state. The superlattice is assumed to be coherently strained to a $Si_{0.4}Ge_{0.6}$ buffer-layer. The contour lines show the variation of the peak-absorption wavelength as a function of the Si well thickness and the $Si_{0.4}Ge_{0.6}$ barrier thickness. The layer thicknesses are measured in monolayers, denoted by ML in the figure.

3.4 Peak Absorption Coefficient and Wavelength

In this section, we present the intersubband absorption coefficients, and the peak-absorption wavelengths of $Si_{1-x}Ge_x$/Si superlattices, for the four representative cases selected in the above section.

3.4.1 [100] Direction; Two-Fold Valleys

In Fig. 3.6 and 3.7, we show the intersubband absorption coefficient for [100] $Si_{1-x}Ge_x$/Si superlattices calculated using Equation 3.3. The structure we consider is a superlattice with Si well layers and $Si_{0.4}Ge_{0.6}$ barrier layers coherently strained to a $Si_{0.4}Ge_{0.6}$ buffer-layer. This band alignment has the two-fold longitudinal electrons in the ground state. The results are presented for the absorption of light at parallel incidence to the superlattice, since normally incident light cannot be absorbed in this configuration. The $Si_{0.4}Ge_{0.6}$ buffer-layer was chosen to push the four-fold valleys higher in energy compared to the two-fold valleys. This choice for the buffer-layer limits the maximum overall thickness for a coherently strained superlattice, since a $Si_{0.4}Ge_{0.6}$ /Si superlattice in its freestanding configuration will have a different in-plane lattice constant than a $Si_{0.4}Ge_{0.6}$ buffer-layer. If we pick a buffer-layer that was lattice-matched to the freestanding lattice constant of the superlattice, then much thicker superlattices can be considered. However, the separation between the two-fold and four-fold levels would then be smaller, and the four-fold states may interfere with the absorption of the two-fold states. Fig. 3.6 shows that fairly good absorption can be achieved for barrier and well widths of about 20 monolayers. The apparent decrease in absorption at large layer thicknesses is an artifact of the method we present in the results. Because we have assumed a constant doping concentration per superlattice unit cell (constant sheet-doping concentration), as the unit cell size of the superlattice increases, the effective bulk-doping concentration decreases, reducing the absorption. In Fig. 3.7 we show the peak-absorption wavelength in μm for transitions from the first to the second conduction subbands. The wavelength range of interest for atmospheric communications (8-14 μm) occurs for Si well thicknesses of 12-20 monolayers. As seen in Fig. 3.7, the quantum well level separations are determined mainly by the well thicknesses, not by the barrier thicknesses, since the barrier heights are fairly large and the masses of the longitudinal electrons are large ($\approx .98m$).

3.4.2 [100] Direction; Four-Fold Valleys

In Figs. 3.8 and 3.9, we show the intersubband absorption coefficients, and peak-absorption wavelengths, respectively, for [100] $Si_{1-x}Ge_x$/Si superlattices, when the four-fold transverse valley electrons are in the ground state. Results are presented for parallel incidence, since absorption at normal incidence does not occur. We have considered a $Si_{0.7}Ge_{0.3}$ well layer and a $Si_{0.2}Ge_{0.8}$ barrier layer coherently strained to a $Si_{0.7}Ge_{0.3}$ buffer-layer. A higher concentration of Ge in the barrier layer would not be desirable, since above $\approx$ 85% Ge concentration the conduction band minimum of $Si_{1-x}Ge_x$ alloys changes from a Si-like Δ-minimum to a Ge-like L-minimum.[22] The $Si_{0.7}Ge_{0.3}$ buffer-layer was chosen to push the two-fold valleys as high in energy as possible compared to the four-fold valleys. Although a buffer-layer lattice-matched to the freestanding $Si_{0.7}Ge_{0.3}$ /$Si_{0.2}Ge_{0.8}$ superlattice could be more appropriate for thick superlattices, however, the smaller two-fold / four-fold splitting might significantly influence the absorption from the four-fold valleys. The peak-absorption coefficients for four-fold electrons occur at wavelengths of 20-30 μm for the layer thickness range shown in Fig. 3.9. This makes the absorption from four-fold electrons less attractive than the absorption from the two-fold electrons for detection in the atmospheric window. However, this configuration is ideal for detection of larger wavelengths ($\lambda > 20\mu m$) with absorption coefficients in excess of

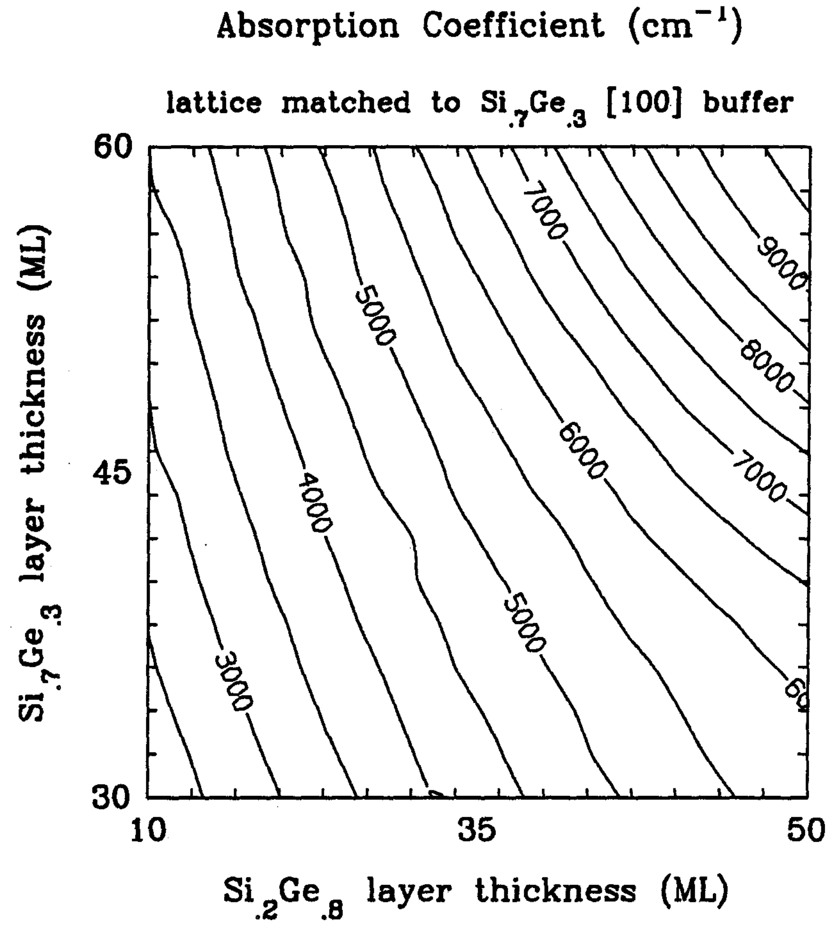

Figure 3.8: Absorption coefficients for light at parallel incidence for a [100] $Si_{0.7}Ge_{0.3}$ /$Si_{0.2}Ge_{0.8}$ superlattice. In this case, the four-fold transverse conduction valleys are in the ground state. The superlattice is assumed to be coherently strained to a $Si_{0.7}Ge_{0.3}$ buffer-layer. The contour lines show the variation of the absorption coefficient as a function of the $Si_{0.7}Ge_{0.3}$ well thickness and the $Si_{0.2}Ge_{0.8}$ barrier thickness. The layer thicknesses are measured in monolayers, denoted by ML in the figure.

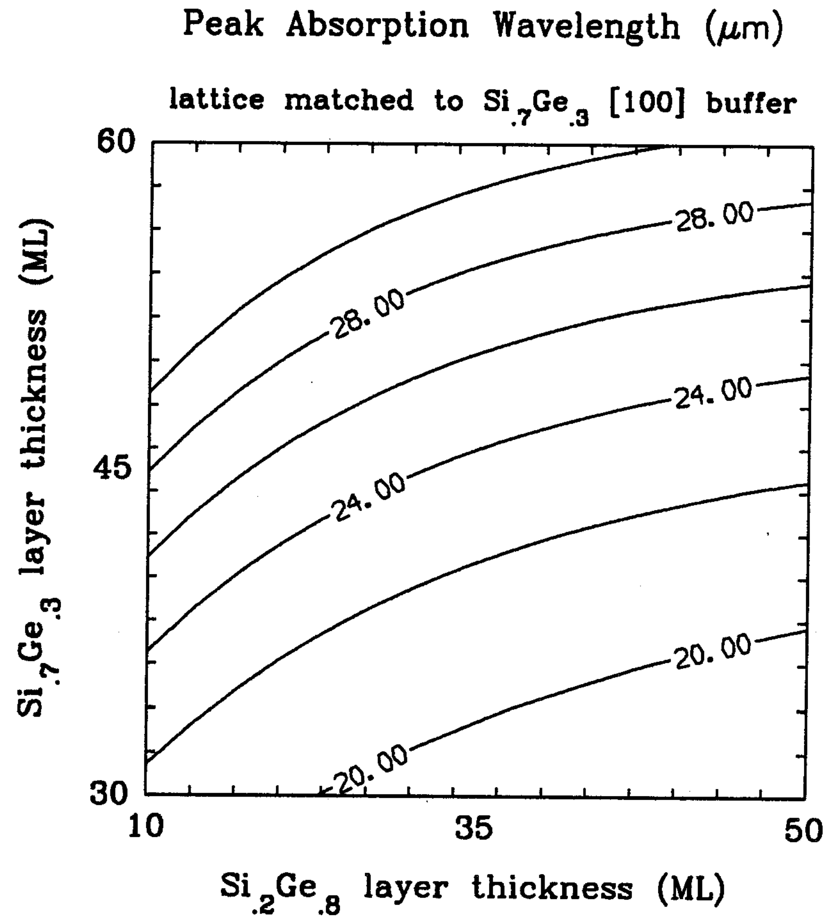

Figure 3.9: Peak absorption wavelengths for light at parallel incidence for a [100] $Si_{0.7}Ge_{0.3}$ /$Si_{0.2}Ge_{0.8}$ superlattice. In this case, the four-fold transverse conduction valleys are in the ground state. The superlattice is assumed to be coherently strained to a $Si_{0.7}Ge_{0.3}$ buffer-layer. The contour lines show the variation of the peak-absorption wavelength as a function of the $Si_{0.7}Ge_{0.3}$ well thickness and the $Si_{0.2}Ge_{0.8}$ barrier thickness. The layer thicknesses are measured in monolayers, denoted by ML in the figure.

10^4 cm^{-1}. The qualitative features of the contour lines in Fig. 3.8 are quite different from those in Fig. 3.6 because the small barrier heights and the small effective masses influence the absorption coefficients significantly. The optical matrix elements are still increasing as a function of the well-layer thickness at 60 monolayers for four-fold electrons, and the decrease in absorption occurs at much larger layer thicknesses than for the two-fold case. The smaller effective masses of the four-fold states ($\approx .19m$) result in slightly larger absorption coefficients for four-fold electrons than for two-fold electrons. As illustrated in Fig. 3.3, it is also possible to obtain an increase in the absorption coefficient as the peak wavelength is increased.

Our analysis of the absorption properties of the two-fold and four-fold electrons for [100] oriented $Si_{1-x}Ge_x/Si$ superlattices shows that two-fold electrons are more suitable for applications in the 8-14 μm range. The potential increase in the absorption that could have been achieved with four-fold electrons because of smaller effective masses is outweighed by the decrease in the optical matrix elements that was due to smaller conduction band offsets and poor confinement of the envelope functions. We also find that because of poor carrier confinement, it is quite difficult to push the peak-absorption wavelength of the four-fold valleys up to the 8-14 μm range.

3.4.3 [111] Direction; Six-Fold Valleys

The absorption coefficient and peak-absorption wavelength of [111] $Si_{1-x}Ge_x/Si$ superlattices are shown in Figs. 3.10 and 3.11, respectively. In Fig. 3.10, we show the absorption coefficient for normally incident light. These results are for normal illumination. The structures are [111] $Si_{1-x}Ge_x/Si$ superlattices with $Si_{0.8}Ge_{0.2}$ well layers and $Si_{0.2}Ge_{0.8}$ barrier layers grown coherently strained to a [111] $Si_{.5}Ge_{.5}$ buffer-layer. There is no preferred azimuthal polarization direction for the absorption of normally incident light in this case. This growth direction preserves the six-fold

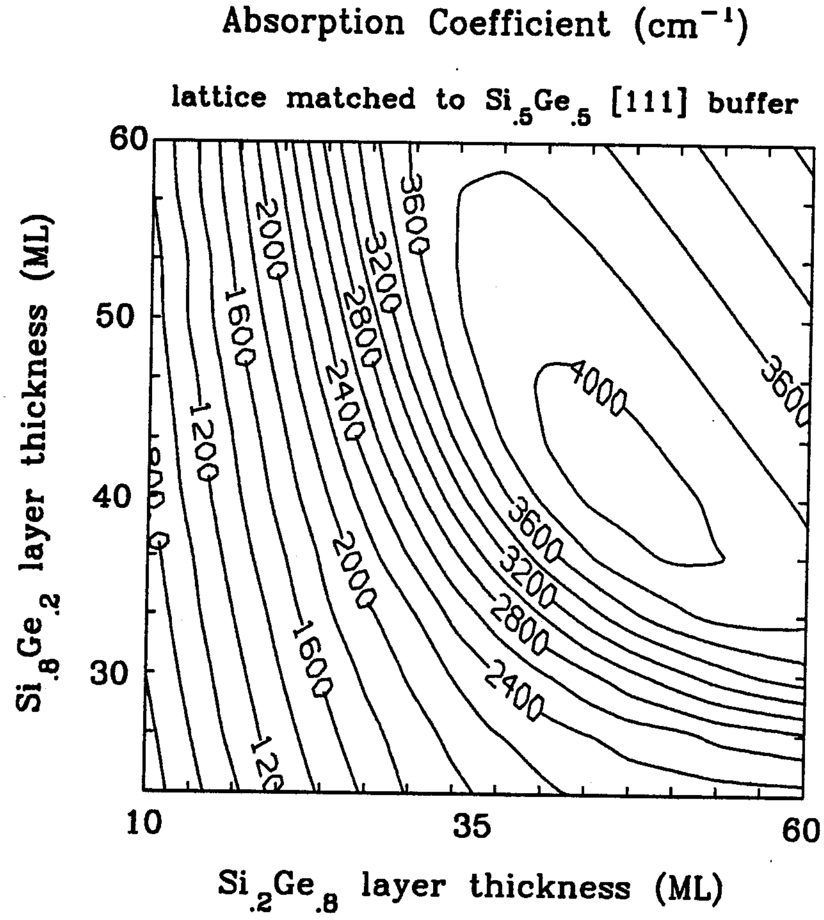

Figure 3.10: Absorption coefficients for light at normal incidence for a [111] $Si_{0.8}Ge_{0.2}$ /$Si_{0.2}Ge_{0.8}$ superlattice. In this case, the six-fold degenerate Δ conduction valleys are in the ground state. The superlattice is assumed to be coherently strained to a $Si_{.5}Ge_{.5}$ buffer-layer. The contour lines show the variation of the absorption coefficient as a function of the $Si_{0.8}Ge_{0.2}$ well thickness and the $Si_{0.2}Ge_{0.8}$ barrier thickness. The layer thicknesses are measured in monolayers, denoted by ML in the figure.

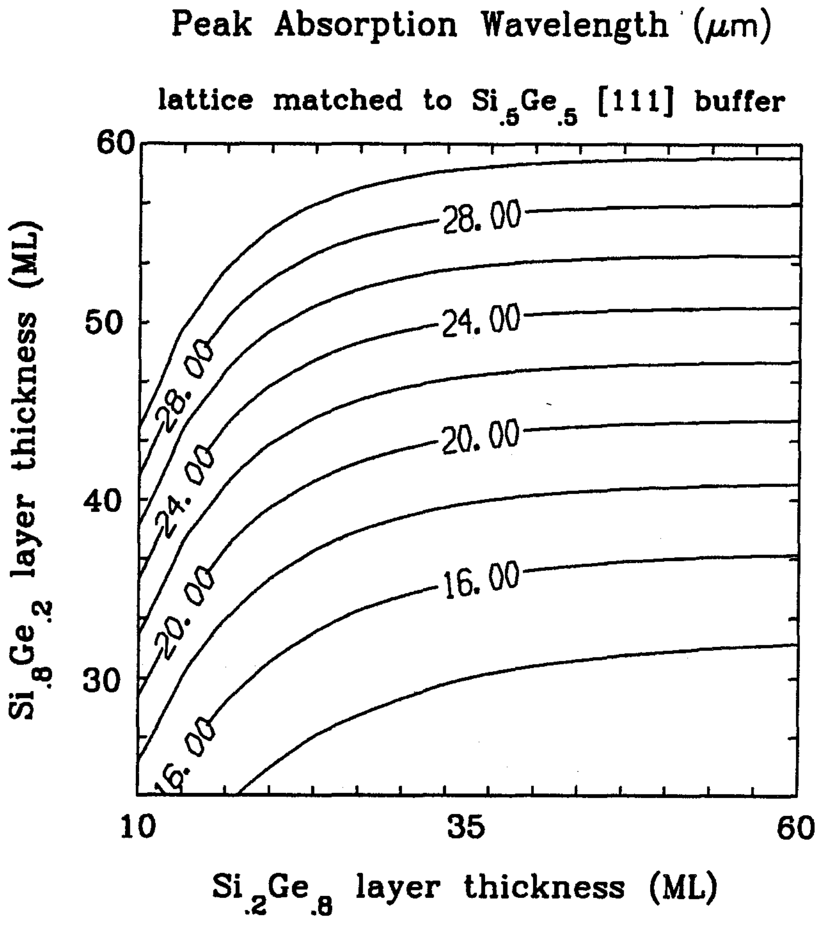

Figure 3.11: Peak absorption wavelengths for light at normal incidence for a [111] $Si_{0.8}Ge_{0.2}$ /$Si_{0.2}Ge_{0.8}$ superlattice. In this case, the six-fold degenerate Δ conduction valleys are in the ground state. The superlattice is assumed to be coherently strained to a $Si_{.5}Ge_{.5}$ buffer-layer. The contour lines show the variation of the peak-absorption wavelength as a function of the $Si_{0.8}Ge_{0.2}$ well thickness and the $Si_{0.2}Ge_{0.8}$ barrier thickness. The layer thicknesses are measured in monolayers, denoted by ML in the figure.

degeneracy of the Δ conduction valleys, and electrons from all six valleys contribute to the absorption. The choice of the buffer-layer is not critical in this case, and we have therefore considered a $Si_{.5}Ge_{.5}$ buffer-layer, quite closely lattice-matched to the freestanding $Si_{0.2}Ge_{0.8}$ /$Si_{0.8}Ge_{0.2}$ superlattice. The obvious advantage of considering such a buffer-layer is the ability to grow thicker coherently strained structures.[35] The contour plot of the absorption coefficient shown in Fig. 3.10 is qualitatively similar to an intermediate case between Fig. 3.6, and Fig. 3.8; the peak in Fig. 3.10 occurs at a larger layer thickness than in Fig. 3.6, but at a smaller layer thickness than where the peak in Fig. 3.8 would be (not shown in figure). This is because the barrier heights and the effective masses in the growth direction for Fig. 3.10, lie in between the values for Fig. 3.6 and Fig. 3.8. The peak-absorption wavelengths of Fig. 3.11 occur more closely to the 8-14 μm range than in Fig. 3.9, making the [111] $Si_{1-x}Ge_x$/Si superlattices more useful than [100] $Si_{1-x}Ge_x$/Si superlattice with four-fold electrons for 8-14 μm infrared applications. Fig. 3.10 shows that a peak-absorption coefficient of 4000 cm^{-1} can be easily achieved for moderate sheet-doping concentrations of 10^{12} cm^{-2}.

3.4.4 [110] Direction; Four-Fold Valleys

Results of the absorption coefficient and peak-absorption wavelength for normally incident light for [110] $Si_{1-x}Ge_x$/Si superlattices are shown in Fig. 3.12 and 3.13, respectively. These results correspond to [110] superlattices with $Si_{0.8}Ge_{0.2}$ well layers and $Si_{0.2}Ge_{0.8}$ barrier layers grown coherently strained to a [110] $Si_{0.2}Ge_{0.8}$ buffer-layer. In these superlattices, the ground state consists of the four-fold conduction valleys that are oriented at 45° to the growth axis. There is a preferred azimuthal direction to the absorption, with peak-absorption occurring for light polarized along the $[1\bar{1}0]$ azimuthal direction, and zero absorption occurring for light polarized along the [001] azimuthal direction. The matrix elements are slightly larger

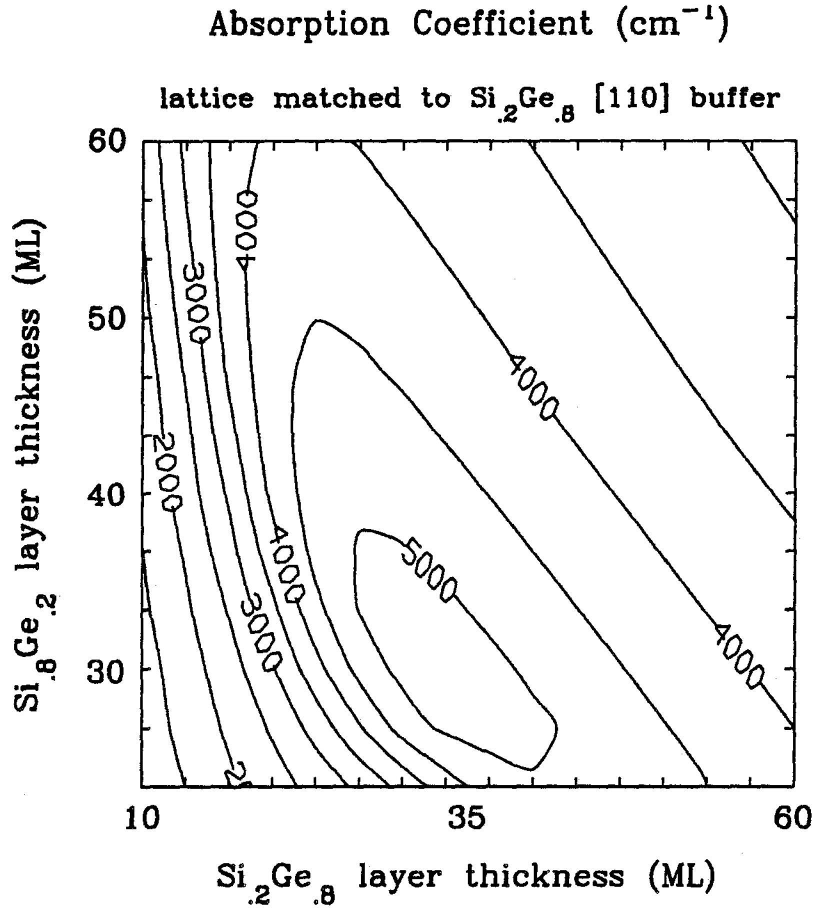

Figure 3.12: Absorption coefficients for light at normal incidence for a [110] $Si_{0.8}Ge_{0.2}$ /$Si_{0.2}Ge_{0.8}$ superlattice. In this case, the four-fold valleys that are oriented at 45 °to the growth axis are in the ground state. The superlattice is assumed to be coherently strained to a $Si_{0.2}Ge_{0.8}$ buffer-layer. The contour lines show the variation of the absorption coefficient as a function of the $Si_{0.8}Ge_{0.2}$ well thickness and the $Si_{0.2}Ge_{0.8}$ barrier thickness. The layer thicknesses are measured in monolayers, denoted by ML in the figure.

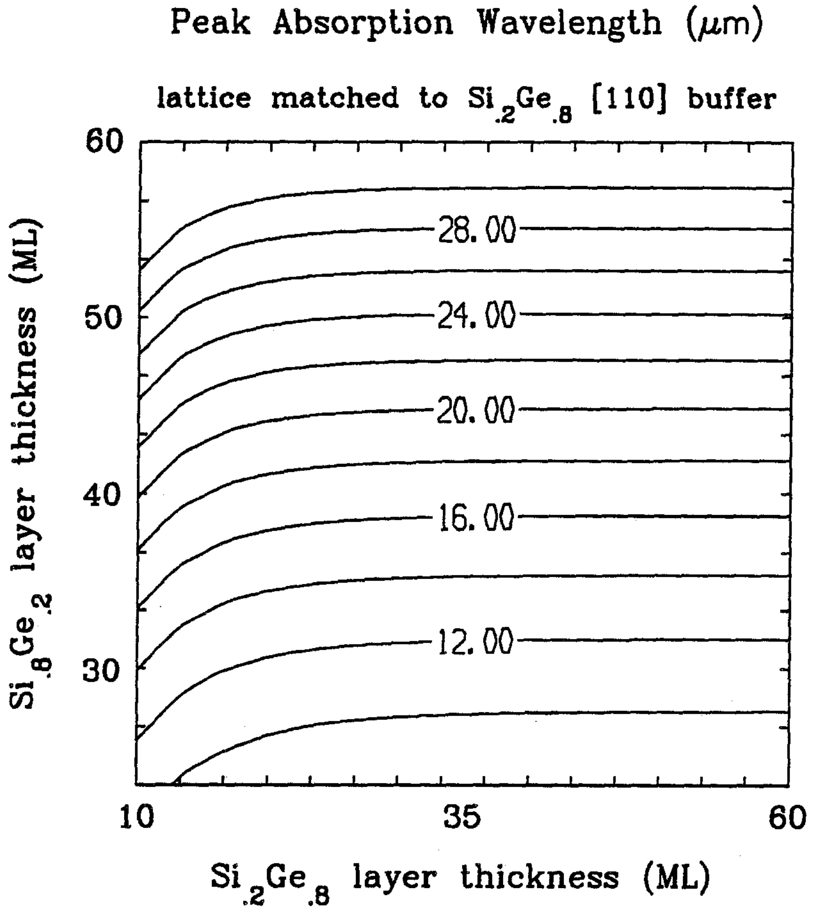

Figure 3.13: Peak absorption wavelengths for light at normal incidence for a [110] $Si_{0.8}Ge_{0.2}$ /$Si_{0.2}Ge_{0.8}$ superlattice. In this case, the four-fold valleys that are oriented at 45 $^{\circ}$to the growth axis are in the ground state. The superlattice is assumed to be coherently strained to a $Si_{0.2}Ge_{0.8}$ buffer-layer. The contour lines show the variation of the peak-absorption wavelength as a function of the $Si_{0.8}Ge_{0.2}$ well thickness and the $Si_{0.2}Ge_{0.8}$ barrier thickness. The layer thicknesses are measured in monolayers, denoted by ML in the figure.

than for the [111] $Si_{1-x}Ge_x/Si$ superlattices because of the larger [110] four-fold conduction band offsets, which give rise to larger intersubband matrix elements. The $Si_{0.2}Ge_{0.8}$ buffer-layer was chosen to push the two-fold valleys higher in energy compared to the four-fold valleys. For this choice of the buffer-layer, the maximum overall thickness for a coherently strained superlattice will be limited by the critical thickness for strain relaxation.[33, 34, 35] If, on the other hand, we pick a buffer-layer that was lattice-matched to the freestanding lattice constant of the superlattice, then much thicker superlattice layers can be considered. However, the separation between the four-fold and two-fold levels would be smaller; the two-fold states could then interfere with the absorption of the four-fold states and reduce the efficiency of detection at normal incidence. Fig. 3.12 shows that an absorption coefficient of 5000 cm^{-1} can be easily achieved for moderate sheet-doping concentrations of 10^{12} cm^{-2}. The absorption shown in Fig. 3.12 is qualitatively similar to that in Fig. 3.6. The peak wavelength of absorption also occurs in the 8-14 μm region, making [110] oriented superlattices good candidates for detection in the atmospheric window.

3.5 Conclusions

We have calculated intersubband absorption strengths for [100], [111], and [110] oriented $Si_{1-x}Ge_x/Si$ superlattices. We have shown that the absorption strengths obtained in all three of these directions are comparable to those found in [100] $Al_xGa_{1-x}As/GaAs$ superlattices. Absorption in [111] and [110] $Si_{1-x}Ge_x/Si$ superlattices is superior to that in [100] $Al_xGa_{1-x}As/GaAs$ superlattices because normally incident light can be absorbed. We find that it is possible to achieve absorption coefficients of about 5000 cm^{-1} for normally incident radiation in the 8-14 μm region by using [110] oriented $Si_{1-x}Ge_x/Si$ superlattices with sheet-doping concentrations of 10^{12} cm^{-2}. $Si_{1-x}Ge_x/Si$ superlattices are particularly suitable for longer-wavelength detection ($\lambda > 14\mu$m), and thus offers an attractive alternative to extrinsic Si detectors, with the additional advantage of wavelength tunability.

References

[1] J. N. Schulman and T. C. McGill, *Appl. Phys. Lett.* **34**, 663 (1979).

[2] H. Sakaki, L. L. Chang, R. Ludeke, C. A. Chang, G. A. Sai-Halasz, and L. Esaki, *Appl. Phys. Lett* **31**, 211 (1977).

[3] D. L. Smith and C. Mailhiot, *J. Appl. Phys.* **62**, 2545 (1987).

[4] C. Mailhiot and D. L. Smith, *J. Vac. Sci. Technol. A* **7**, 445 (1989).

[5] L. C. West and S. J. Eglash, *Appl. Phys. Lett.* **46**, 1156 (1985).

[6] D. D. Coon, and R. P. G. Karunasiri, *Appl. Phys. Lett.* **45**, 649 (1984).

[7] E. L. Dereniak, and D. G. Crowe, in, *Optical Radiation Detectors* , Wiley, New York (1984).

[8] B. F. Levine, K. K. Choi, C. G. Bethea, J. Walker, and R. J. Malik, *Appl. Phys. Lett.* **51**, 934 (1987).

[9] B. F. Levine, K. K. Choi, C. G. Bethea, J. Walker, and R. J. Malik, *Appl. Phys. Lett.* **50**, 1092 (1987).

[10] K. K. Choi, B. F. Levine, C. G. Bethea, J. Walker, and R. J. Malik, *Appl. Phys. Lett.* **50**, 1814 (1987).

[11] B. F. Levine, C. G. Bethea, G. Hasnain, J. Walker, and R. J. Malik, *Appl. Phys. Lett.* **53**, 296 (1988).

[12] L. Esaki, and H. Sakaki, *IBM Tech. Disclosure Bull.* **20**, 2456 (1977).

[13] D. K. Ferrey, in *Gallium Arsenide Technology*, Sams, Indianapolis, IN (1985).

[14] M. A. Kinch and A. Yariv, *Appl. Phys. Lett.* **55**, 2093 (1989).

[15] K. W. Goossen, S. A. Lyon, and K. Alavi, *Appl. Phys. Lett.* **53**, 1027 (1988).

[16] C. I. Yang and D. S. Pan, *J. Appl. Phys.* **64**, 1573 (1988).

[17] C. I. Yang, D. S. Pan, and R. Somoano, *J. Appl. Phys.* **65**, 3253 (1989).

[18] E. R. Brown and S. J. Eglash, *Phys. Rev. B* **41**, 7559 (1990).

[19] E. Kasper and J. C. Bean in, *Silicon Molecular Beam Epitaxy* , Chemical Rubber, Boca Raton, FL (1987).

[20] R. People, *Phys. Rev. B* **32**, 1405 (1985).

[21] R. People, and J. C. Bean, *Appl. Phys. Lett.* **48**, 538 (1986).

[22] C. G. Van de Walle, and R. M. Martin, *Phys. Rev. B* **34**, 5621 (1986).

[23] F. Bassani, in *Electronic States and Optical Transitions in Solids*, Pergammon, New York, NY (1973).

[24] J. M. Luttinger and W. Kohn, *Phys. Rev.* **97**, 869 (1955).

[25] M. Cardona and F. H. Pollack, *Phys. Rev.* **142**, 530 (1966).

[26] Y. Rajakarunanayake and T. C. McGill, *Phys. Rev. B* **40**, 3051 (1989).

[27] C. G. Van de Walle, and R. M. Martin, *J. Vac. Sci. Technol. B* **3**, 1256 (1985).

[28] E. T. Yu, E. T. Croke, T. C. McGill, and R. H. Miles, *Appl. Phys. Lett.* **56**, 569 (1990).

[29] H. Hesagawa, *Phys. Rev.* **129**, 1029 (1963).

[30] J. C. Hensel and G. Feher, *Phys. Rev.* **129**, 1041 (1963).

[31] C. Herring, and E. Vogt, *Phys. Rev.* **101**, 944 (1956).

[32] Y. Rajakarunanayake and T. C. McGill, *J. Vac. Sci. Technol. B* **4**, 799 (1989).

[33] R. People and J. C. Bean, *Appl. Phys. Lett.* **47**, 322 (1985).

[34] J. C. Matthews and A. E. Blakeslee, *J. Cryst. Growth* **27**, 118 (1974).

[35] R. H. Miles, T. C. McGill, S. Sivananthan, X. Chu, and J. P. Faurie, *J. Vac. Sci. Technol. B* **5**, 1263 (1987).

Part II

II-VI Structures

Chapter 4

Band Alignment of Wide-Gap II-VI Superlattices

4.1 Introduction

In this chapter, we investigate the band alignment of wide band gap $Zn_{1-x}Cd_xTe$-ZnTe and $ZnTe_{1-x}Se_x$-ZnTe superlattices by optical spectroscopy, and determine the valence band offsets in ZnSe-ZnTe and CdTe-ZnTe heterojunctions. We make use of the band alignments of these heterojunctions to engineer heterostructures that are attractive for visible light-emitters.

4.1.1 Background and Motivation

The major motivation behind current research in wide band gap II-VI semiconductors is to develop optoelectronic devices such as light-emitting diodes (LEDs) and semiconductor lasers,[1, 2] that can perform in the blue/green region of the spectrum. The II-VI semiconductors such as ZnSe and ZnTe are ideal candidates for this task by virtue of their wide band gaps. In Fig. 1.3 we have illustrated the wavelength response of the human eye versus the band gaps of several II-VI semiconductors to provide a background on which semiconductors are suitable for visible light-emitter applications. Two particularly important wide-gap II-VIs are ZnSe and ZnTe, which have low-temperature band gaps of 2.82 eV and 2.39 eV, respectively. However, difficulties associated with obtaining selective doping in both *n*- and *p*-type material have limited the usefulness of these semiconductors in device applications.[3] To date, possibilities for *p*-*n* homojunctions from these materials seem quite slim, although there are a few recent reports that indicate limited success.[4, 5] Further details on the homojunction approach to obtaining minority carrier injection from II-VI semiconductors will be discussed in Chapter 5.

Heterojunction Approach

In this chapter we will emphasize the heterojunction approach as an alternative to homojunctions.[2] Recent advances in wide band gap II-VI semiconductor growth by molecular beam epitaxy (MBE)[6] and metal-organic chemical vapor deposition (MOCVD)[7] have enabled the fabrication of a wide variety of interesting heterostructures, with the additional flexibility of engineering the band-edge positions. The heterojunction approach has opened up new avenues for obtaining minority carrier injection,[8] since it is usually possible to control at least one conductivity type in many wide band gap II-VI semiconductors; for example, ZnSe can be easily doped *n*-type but not *p*-type, while ZnTe can be easily doped *p*-type, but not *n*-type, raising the possibility of *n*-ZnSe/*p*-ZnTe[9] heterojunctions. The heterojunction approach has also enabled the possibility of combining wide-gap semiconductors with smaller band gap materials such as CdTe, which are dopable in both *n*- and *p*-types; CdTe has a low-temperature band gap of 1.6 eV, and serves as a quantum well material for structures made from wider band gap materials such as ZnTe.

Although it is possible to combine several *n*-type semiconductors with other *p*-type semiconductors to obtain *p*-*n* junctions, this is not a sufficient condition for minority carrier injection.[10] This is because the value of the valence and conduction band offsets play a crucial role in determining the effectiveness of minority carrier injection. Basic considerations of the minority carrier injection efficiency across a p-n heterojunction have been illustrated earlier by McCaldin.[10, 11] The band offsets obtained in this work would be useful in evaluating the merits of wide-gap II-VI heterojunctions based on ZnSe, ZnTe and CdTe.

4.1.2 Summary of Results

The results of this chapter can be divided into three main parts. The first part is the study of the band structure of II-VI superlattices. The second part is the optical investigation of the band offsets of CdTe-ZnTe and ZnSe-ZnTe heterojunctions. The third part is the theoretical analysis of the band alignment of II-VI quaternaries for heterojunction light-emitters.

Band Structure of II-VI Superlattices

We have investigated the band structure of II-VI strained-layer superlattices within the framework of an 8-band $\vec{k} \cdot \vec{p}$ theory. With this procedure, we are able to account adequately for the strain-induced effects and quantum confinement effects in these superlattices. We study the band gap variation of several superlattices as functions of the layer thicknesses and band offsets. We also investigate the prospects for customizing the band gaps of ZnSe-ZnTe superlattices throughout the visible spectrum by variation of the layer thicknesses.

Optical Investigation of the Band Offsets

We have performed low-temperature photoluminescence measurements on MBE-grown $Zn_{1-x}Cd_xTe$-ZnTe and $ZnTe_{1-x}Se_x$-ZnTe superlattices, and have investigated their band offsets by fitting the optical band gaps by $\vec{k} \cdot \vec{p}$ theory. We find that the average valence band offset of the CdTe-ZnTe system is quite small (-50 ± 160 meV) with the valence band-edge of CdTe lying lower than that of ZnTe. Thus, in $Zn_{1-x}Cd_xTe$-ZnTe superlattices, the holes are confined mostly by strain effects; the heavy-holes and the electrons are confined in the smaller band gap Cd-rich layers (type I band alignment), while the light holes are confined in the wider band gap Zn-rich layers (type II band alignment). On the other hand, we find that the valence band offset of the ZnSe-ZnTe system is quite large (-907 ± 120 meV), with the valence band edge of ZnSe lying lower than that of ZnTe. In this situation, the band alignment is type II for both light and heavy holes. Given these values, we investigate the possibilities for minority carrier injection in II-VI heterostructures made from ZnSe, ZnTe and CdTe. We also investigate the band bowing in the $ZnTe_{1-x}Se_x$ alloys, and determine the components of bowing in the conduction and valence bands separately.

Theoretical Considerations of II-VI Quaternaries

We have also theoretically surveyed the possibilities for minority carrier injection from heterojunctions made of II-VI quaternary alloys. We consider the possibility of engineering favorable light-emitter structures that optimize the parameters such as wide band gaps, favorable band offsets, lattice-match and dopability. We find that it should be possible to achieve minority carrier injection in quaternary alloys and to obtain band gaps in the blue/green region of the spectrum by engineering heterostructures with proper choices of alloy compositions. These results are very promising for fabricating blue/green light-emitters from the wide band gap II-VI materials.

4.1.3 Outline of Chapter

In Section 4.2 of this chapter, we discuss the strain induced effects in the band structure of lattice-mismatched superlattices, and briefly describe the theoretical $\vec{k} \cdot \vec{p}$ formalism used to calculate their band structure. In Section 4.3 we fit the experimental band gaps obtained by low-temperature photoluminescence measurements with $\vec{k} \cdot \vec{p}$ theory to obtain the valence band offsets. In Section 4.4 we have theoretically extended the analysis of the band alignments of Section 4.3 to determine favorable possibilities for wide band gap heterostructure light-emitters based on $\mathrm{Zn}_{1-x}\mathrm{Cd}_x\mathrm{Te}_{1-y}\mathrm{Se}_y$ and $\mathrm{Zn}_{1-x}\mathrm{Mn}_x\mathrm{Te}_{1-y}\mathrm{Se}_y$ quaternaries. Section 4.5 concludes the chapter.

4.2 Band Structure of II-VI Superlattices

In this section, we discuss the theoretical formalism for calculating the band structure of strained-layer superlattices, and present detailed results for ZnSe-ZnTe superlattices to illustrate the effects of strain on the band structure.

4.2.1 $\vec{k} \cdot \vec{p}$ Method

The bulk band structure of the constituent materials is calculated using Kane's eight-band $\vec{k} \cdot \vec{p}$ model. This is a well-known form for the $\vec{k} \cdot \vec{p}$ Hamiltonian of a zincblende semiconductor (including the spin-orbit interaction), written in the Kramer basis set ($|J, M_J\rangle$ representation).[12] Here J is the total angular momentum, and M_J is the axial angular momentum. The formal details of the $\vec{k} \cdot \vec{p}$ technique were explained in our discussion of Si/Ge superlattices in Section 2.2. We have taken an approach identical to that of Wu[13] in calculating the properties of wide band gap II-VI superlattices; the details of the calculations and the derivations of the Hamiltonian matrices will not be reproduced in this thesis since a more complete account is given in the thesis by Wu[13]. Once the strained bulk band structure is known, then the superlattice band structure can be found by the application of the complex band structure technique explained in Section 2.2. In our calculations, we have used the boundary conditions, that the zone-center components of the wavefunctions are conserved across a heterojunction interface, and the probability current is conserved across the interface. The justification for these boundary conditions is given in Section 1.6.

Material parameters used in the calculations are enumerated in Table 4.1. In Table 4.1, a_0 is the lattice constant, E_0 is the band gap, and Δ_0 is the spin-orbit splitting. The Luttinger parameters of the valence bands are given by γ_1, γ_2, γ_3, κ and q.[14] To preserve the isotropy of the bulk energy bands, we have replaced the values of γ_2 and γ_3 listed in Table 4.1 by their average value, and set q=0. The quantities C_{11}, C_{12} and C_{44} are the elastic coefficients of the materials. The strain effects are taken into account by the deformation potentials at the zone-center, which are denoted by a, b, c and d.[19]

4.2.2 Band Offsets and Strain Effects

The large lattice-mismatch that exists between CdTe-ZnTe (≈+6.2%) and ZnSe-ZnTe (≈-7.1%) makes strain effects play an important role in determining the band alignments. The negative sign on the lattice-mismatch indicates that ZnSe has a smaller lattice constant than ZnTe, while the opposite is true for CdTe. The most prominent effect of strain on the band structure of the constituent materials is to split the valence band degeneracy between the heavy-hole and the light-hole. In the layer that is under uniaxial compression, the heavy-hole bands shift higher in energy, while in the layer that is under uniaxial tension, light-hole bands shift higher in energy. The $\vec{k} \cdot \vec{p}$ method is well suited for the calculation of strain effects, since

Parameter		ZnSe	ZnTe	CdTe
Lattice constant (Å)	a_0	5.669	6.104	6.481
Band gap 5K (eV)	E_g	2.82	2.39	1.60
Spin orbit energy (eV)	Δ	0.43	0.92	0.91
Squared P-Matrix Element (eV)	E_P	24.2	19.1	20.7
Luttinger parameter	γ_1	3.77	3.74	5.29
Luttinger parameter	γ_2	1.24	1.07	1.89
Luttinger parameter	γ_3	1.67	1.64	2.46
Luttinger parameter	κ	0.64	0.42	1.27
Luttinger parameter	q	0.02	0.05	0.05
Deformation potential (eV)	a	1.35	1.35	1.23
Deformation potential (eV)	b	-1.20	-1.78	-1.18
Deformation potential (eV)	c	-2.82	-2.7	-2.2
Deformation potential (eV)	d	-3.81	-4.58	-4.83
Elastic constant (10^{10} Nm^{-2})	C_{11}	8.10	7.13	5.35
Elastic constant (10^{10} Nm^{-2})	C_{12}	4.88	4.07	3.68
Elastic constant (10^{10} Nm^{-2})	C_{44}	4.41	3.12	1.99

Table 4.1: Table of material parameters used in the $\vec{k} \cdot \vec{p}$ calculations for wide band gap II-VI semiconductors ZnSe, ZnTe and CdTe. The parameters $\gamma_1, \gamma_2, \Gamma_3, \kappa, q, \Delta$, and E_p were taken from Reference[14] . The deformation potentials were obtained from References[15] and[16] . The elastic constants were taken from Reference[17]

the simple transformation of replacing quadratic terms $k_i k_j$ in the $\vec{k} \cdot \vec{p}$ Hamiltonian by ϵ_{ij}, and replacing the reciprocal mass parameters by deformation potentials takes care of strain effects systematically.[18, 19]

Our calculations indicate that the energy shifts produced by a large lattice-mismatch $\approx$6-7% can influence band-edge positions by $\approx \pm$ 200 meV. However, for an accurate description of the band structure of strained-layer superlattices, it is necessary to know the degree of strain relaxation in the overall structure as well as in the individual layers.[20] In our calculations we have assumed that the overall structures have relaxed to the freestanding superlattices, since the total thicknesses of our samples (2000-2500 Å) are usually thicker than the critical thicknesses for pseudomorphic growth given by models such as Matthews and Blakeslee.[21]-[25] On the other hand, we have assumed that the individual layers are below the critical thickness for strain relaxation. Thus, we can model the band structure of our strained-layer superlattices as that of freestanding superlattices. A freestanding superlattice is a structure in which the in-plane lattice constant is determined by minimizing the elastic free energy of the layers. These assumptions are consistent with experimental results on strain relaxation in superlattices by Miles et al.[20, 26] However, in our calculations we find that the superlattice band gaps are fairly insensitive (within $\pm$ 20 meV) to the particular assumption that the overall superlattice is modeled as a freestanding superlattice. Further details on the strain effects in lattice-mismatched heterostructures were given in Section 1.5.

Previous Results for Band Offsets

The previous values of the valence band offset reported for the ZnSe-ZnTe system span over a wide energy range. Harrison and Tersoff[27] predict a value for the valence band offset of -290 meV, while experimental measurements by Katnani and Margaritondo yielded a value of -430 meV.[28] In Fig. 1.7 we show the relative

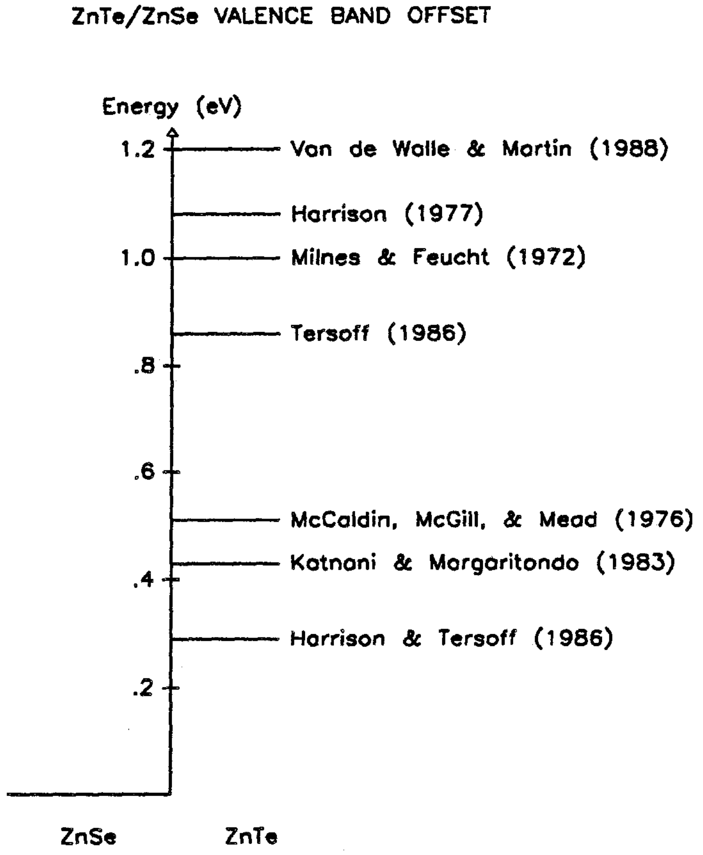

Figure 4.1: The band offset of ZnSe-ZnTe heterojunctions according to several theoretical predictions and experimental measurements. The relative position of the ZnTe valence band-edge is plotted with respect to that of ZnSe; the values shown are Harrison and Tersoff (1986);[27] Katnani and Margaritondo (1983);[28] McCaldin, McGill and Mead (1976);[29] Tersoff (1986);[30] Milnes and Feucht (1972);[31] Harrison (1977);[32] and Van de Walle and Martin (1988).[33]

alignment of the energy bands, assuming a valence band offset of -1080 meV, consistent with the prediction by Harrison.[32] Our previous estimate on the band offset of this system, based on the ZnSe-ZnTe superlattices grown by Kobayashi[34] et al. was -975 meV.[18, 35] The large range of energy spanned by these predictions is illustrated in Fig. 4.1.

On the other hand, the previous results on the CdTe-ZnTe system seem to indicate that the valence band offset is small. The theoretical predictions by Harrison[32] for this system yield a value of 180 meV while Harrison and Tersoff[27] place the valence band offset at -30 meV. The x-ray photoelectron measurements by Tran Minh Duc et al.[36] yielded -100 ± 60 meV. The common anion rule of McCaldin et al.[29] predicts a valence band offset of zero.

Since strain effects move the band-edges around, the effective valence band offset in a strained-layer superlattice is different from the unstrained offset, and depends on the particular strain distribution in the structure. Thus, it is more meaningful to describe the value of the valence band offset as the difference between the valence bands of the two materials before strain is introduced, and to include the strain effects with the $\vec{k} \cdot \vec{p}$ method. The valence band offset so defined has the advantage of being independent of strain and layer thicknesses, and is an input parameter to the $\vec{k} \cdot \vec{p}$ theory. This is the quantity that is illustrated as the difference between the dashed lines of Fig. 1.7. We can determine the best fit for the valence band offset by reading off the value that corresponds to the theoretical band gap that agrees best with the experimental band gap. It is also possible to obtain the error bars for a given uncertainity in the experimental gaps, by reading off the corresponding change in the valence band offset.

4.2.3 Theoretical Results for ZnSe-ZnTe Superlattices

To illustrate the results of band structure calculations, we have selected the ZnSe-ZnTe superlattice as a representative example. In Fig. 1.7, we have shown the relative alignments of the energy bands for the Harrison[32] value of the valence band offset of 1.080 eV. This value of the band offset was chosen purely for illustrative purposes to discuss the effects of strain on the bulk band structures of ZnSe and ZnTe. The band structures of ZnSe and ZnTe shown in Fig. 1.7 were calculated assuming that the magnitude of the strain in each layer was equal to that of a freestanding 15 Å-15 Å superlattice. As described earlier, by a freestanding superlattice we mean a configuration in which the in-plane lattice constant is chosen to minimize the elastic free energy of the structure.

The band structures shown in Fig. 1.7 correspond to the strained bulks in the [100] direction with $k_{||} = 0$. We have shown the band structure only up to a quarter of the distance to the Brillouin zone edge along the growth direction of the superlattice. ZnSe layers in the superlattice are under tensile strain, which has the effect of reducing the band gap of this material. Thus the valence bands of ZnSe move up and the conduction bands move down with respect to their unstrained positions. In addition, the degeneracy of the heavy-hole and light-hole band is removed by the uniaxial strain. The dashed lines indicate the original positions of the band-edges. In the superlattice of Fig. 1.7, the ZnSe light-hole bands are shifted up in energy by 157 meV, while the heavy-hole bands shift down in energy by 37 meV. The conduction bands of ZnSe are also lowered by 78 meV for this case. On the other hand, the ZnTe layers of the superlattice are under compressive strain. This causes the conduction bands to move up, and the valence bands to move down with respect to their unstrained positions, increasing the band gap of this material. The heavy-hole and the light-hole bands are also split about their average position because of uniaxial terms. In Fig. 1.7, the ZnTe heavy-hole moves up by 118 meV, the light-hole moves down by 135 meV, and the conduction band moves up by 85 meV. We also see that the spin-orbit, split-off bands play a more important role in ZnSe than in ZnTe because they are closer to the light-hole band in ZnSe.

In Fig. 4.2 we have shown the dependence of the band gap on the valence band offset for strained, freestanding superlattices. Because of the large range of valence band offsets reported for this system, we have presented results for a wide range of values. As the valence band offset gets larger, the band gap of the superlattice decreases. This is due to the fact that the superlattice valence band is largely determined by the ZnTe heavy-hole bands while the superlattice conduction band is determined by ZnSe conduction bands. For a type II band alignment that exists in this superlattice, an increase in the valence band offset brings the heavy-hole band of ZnTe and the conduction band of ZnSe closer to each other, reducing the superlattice band gap. We have shown three representative superlattices corresponding to layer thicknesses of 10 Å-10 Å, 15 Å-15 Å, and 20 Å-20 Å. The larger band gap is observed for the superlattice with the smallest period. This is due to the enhancement of the two dimensional confinement of the wavefunctions of the superlattice as the layer thicknesses get smaller. This result shows that it is possible to obtain the band offset of the superlattice directly by a measurement of the superlattice band gap.

Figure 4.3 shows a contour plot of the superlattice band gap as a function of the ZnSe and ZnTe layer thicknesses, based on a valence band offset of -0.907 eV, where the ZnSe valence band-edge lies lower than that of ZnTe. This value of the valence band offset is in agreement with our experimental investigations, reported in Section 4.3. In Fig. 4.3 the trend is to obtain smaller band gaps as either the ZnSe or the ZnTe layer thickness is increased. Since the ZnSe layer acts as the barrier material for the heavy-hole band, the effect it has on the valence band is quite small. Thus, changes of the band gap as layer thicknesses are varied in a direction parallel to the ZnSe axis come mainly from the motion of the conduction band. On the other

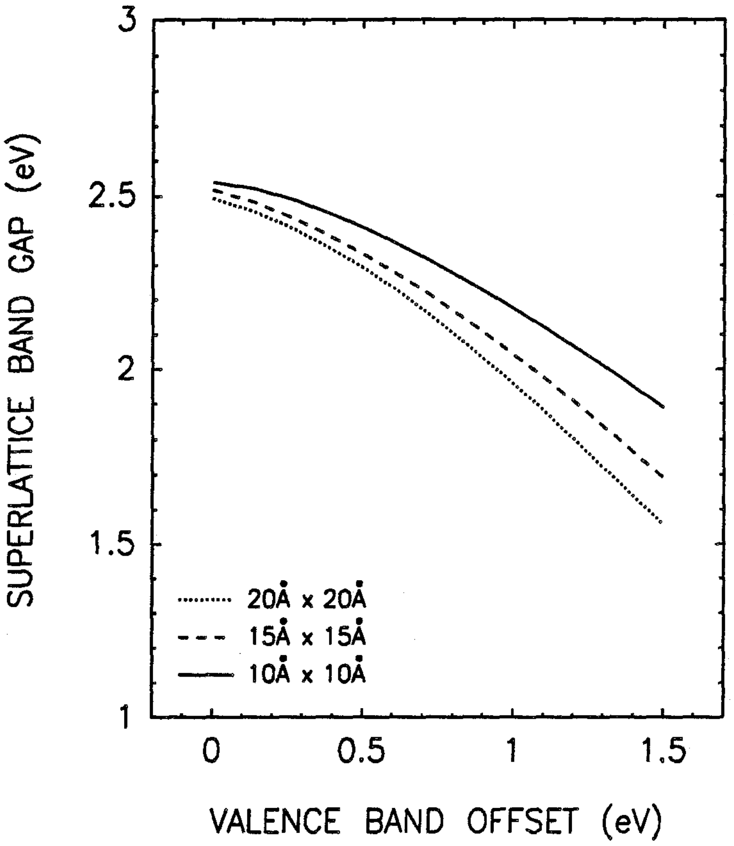

Figure 4.2: Band gap of a few representative ZnTe-ZnSe superlattices versus the valence band offset $E_V^{ZnTe} - E_V^{ZnSe}$. Notice that the band gap decreases as the valence band offset is increased. Structures were assumed to be coherently strained with an in-plane lattice constant determined by minimizing the elastic free energy of the superlattice (i.e, the freestanding limit).

hand, ZnTe acts as the barrier material for the conduction band. Thus, changes of the band gap as layer thicknesses are varied in a direction parallel to the ZnTe axis are derived mainly from the motion of the heavy-hole band. This figure also shows that for superlattices of a given period (d_{ZnSe}+d_{ZnTe}=const.), as we scan from the ZnSe side to the ZnTe side of the contour plot, the superlattice band gap bows. This type of bowing is characteristic of type II superlattices.

4.3 Optical Investigation of the Band Offsets

In this section, we investigate the band alignments of $ZnTe_{1-x}Se_x$-ZnTe and $Zn_{1-x}Cd_xTe$-ZnTe superlattices by optical spectroscopy. The first step in our procedure is to determine optically the superlattice band gap. This has been done by obtaining the energy positions of near band gap low-temperature photoluminescence peaks associated with the free excitons, and then adding the exciton binding energies obtained by theoretical calculations. For the purpose of this work, we have not considered the variation of the exciton binding energy as a function of the well widths. However, a detailed account of the exciton binding energies of $Zn_{1-x}Cd_xTe$-ZnTe and $ZnTe_{1-x}Se_x$-ZnTe superlattices is given by Liu and McGill.[37] Another source of uncertainity could be introduced at this step by the fact that the dominant photoluminescence peaks may be associated with substantially deeper centers than free excitons. The effects of such a systematic error in our analysis on the validity of our conclusions is discussed in Section 4.3.3, along with the discussion of the photoluminescence spectra. The second step in our procedure is to compare the experimentally obtained superlattice band gaps to the theoretical predictions of the band gap as a function of the valence band offset, to obtain the best fit for the valence band offset. The final values we report for the band offsets are averages over a series of samples.

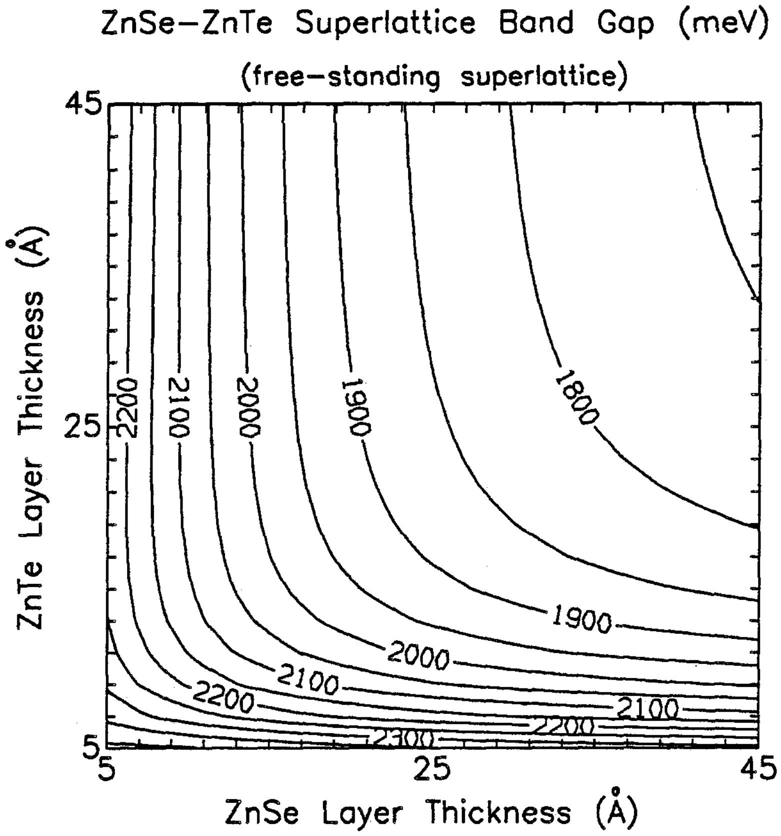

Figure 4.3: Contour plot of the ZnSe-ZnTe superlattice band gap at $5K$ as a function of the layer thicknesses of ZnSe and ZnTe within a single superlattice period. The valence band offset is assumed to be -0.907 eV, where the ZnSe valence band-edge lies lower than that of ZnTe. The strain distribution corresponds to that of a free-standing superlattice. The contour interval is 50 meV.

4.3.1 Band Alignment Considerations

To illustrate the difference in sensitivity between type I and type II band alignments to optical determination of the band offset, we show the band diagram of a type II superlattice in Fig. 4.4. In this figure, the superlattice band gap is denoted by E_g^{SL}, and the band gaps of the constituent materials are denoted by a E_{g1} and E_{g2}, respectively. The valence band offset and conduction band offset are ΔE_V and ΔE_C, while the quantum confinement energies in the valence and conduction bands that are due to the superlattice potential are denoted ΔE_{qv} and ΔE_{qc}, respectively. From the band diagram of Fig. 4.4, we can obtain the following expressions:

$$\Delta E_V = E_{g2} - E_M, \tag{4.1}$$

$$\Delta E_C = E_{g1} - E_M, \tag{4.2}$$

where

$$E_M = E_g^{SL} - \Delta E_{qc} - \Delta E_{qv}. \tag{4.3}$$

By performing photoluminescence measurements on the superlattices, we can obtain E_g^{SL}. The quantum confinement energies ΔE_{qv} and ΔE_{qc} for superlattices with thick layers are only weak functions of the barrier heights (band offsets), and can be calculated by assuming a guess value for the band offsets. These confinement energies are mostly dependent on the well widths, and the value of the effective mass in the wells. Thus, we can obtain the value E_M from Equation 4.3, with the knowledge of E_g^{SL} from experiment, and ΔE_{qv}, ΔE_{qc} from theory. It is then possible to obtain the valence and conduction band offsets from Equations 4.1 and 4.2, if the band gaps E_{g1} and E_{g2} of the constituent layers are known. One can iterate this procedure to obtain self-consistency (agreement with the initial guess and the final value for the offset). Notice that simple explicit expressions for the band offsets as in Equations 4.1 and 4.2 cannot be written in terms of the superlattice band gaps

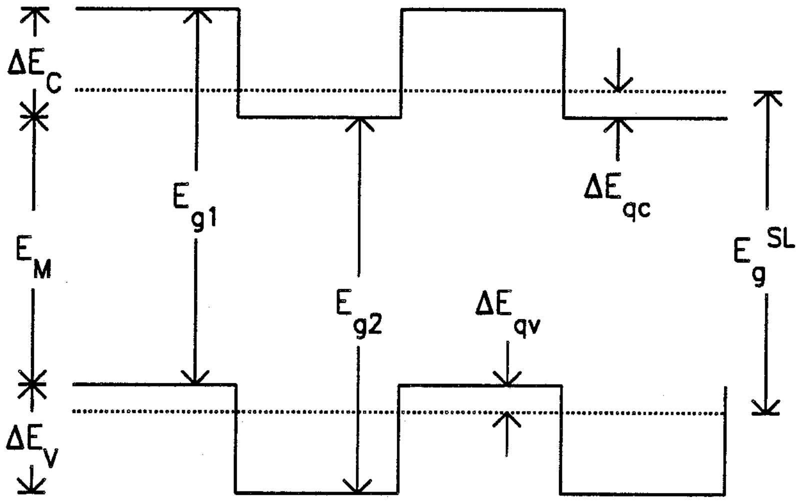

Figure 4.4: A schematic band diagram of a type II superlattice. The superlattice band-edges are denoted by the dashed lines, while the bulk band-edges of the constituent materials are denoted by solid lines

if the band alignment is type I; for a type I superlattice, band offsets occur only implicitly in the expression for the superlattice band gap.

Band Gap Bowing

This optical technique is also well suited for determining the individual bowing parameters of valence band and conduction band positions separately if the ternary alloys have a large band gap bowing as in the case of $\mathrm{ZnTe}_{1-x}\mathrm{Se}_x$ alloys. The band gap of the $\mathrm{ZnTe}_{1-x}\mathrm{Se}_x$ ternary alloys at 5K, with a Se composition x is given by the following formula:[38]

$$E_g(x) = 2.82x + 2.39(1-x) - 1.23x(1-x), \tag{4.4}$$

where $E_g(x)$ is measured in (eV). We report the value for the valence band offset as a function of x for the whole alloy composition range.

4.3.2 Samples

Two series of samples were grown on thick ZnTe buffer-layers ($\approx 2\mu m$) for the purpose of investigating strain effects and determining the band offsets of CdTe-ZnTe and ZnSe-ZnTe systems. The ZnTe buffer-layers themselves were grown on III-V substrates. The details of the growth of II-VI epitaxial layers on III-V buffer-layers is described in the work of Phillips et al.[39, 40] The growth temperature of all superlattices was 270 °C . The growth was from elemental Zn, Te, Se sources, and a CdTe compound source. The measured source temperatures were Zn (270 °C), Te (323 °C), CdTe (480-520 °C) and Se (160-170 °C). Typical growth rates were 0.3 μm/hr, and the total thicknesses of the superlattices were 2200 Å on the average. We have considered several superlattices with alloy compositions and layer thicknesses given in Table 4.2. The superlattice periods were determined for a few samples by x-ray measurements, and in other samples they were estimated from the growth-rate data. The alloy compositions were always determined by electron microprobe measurements, and compared with photoluminescence measurements and x-ray measurements where available.

Table 4.2 shows a list of the samples used for the two studies. For the determination of the ZnSe-ZnTe offset over the whole alloy composition range, we have studied four superlattice samples and two alloy buffer-layers. On the other hand, for the determination of the CdTe-ZnTe band offset, we have considered a series of seven superlattice samples and two alloy buffer-layers.

4.3.3 Photoluminescence

The photoluminescence of the samples was obtained for temperatures between 5-100 K. We used either 1.0 mW of 4880 Å line of an Argon ion laser, or 1.0 mW of 3250 Å line of a He-Cd UV laser for above band gap pumping. The photoluminescence was spectrally dispersed by a SPEX-1269 spectrometer and detected by a photomultiplier tube with a GaAs photocathode cooled to -20 °C .

$Zn_{1-x}Cd_xTe$-ZnTe Superlattices

In Fig. 4.5(a) and 4.5(b), we compare the photoluminescence for a $Cd_{.22}Zn_{.78}Te$-ZnTe 62 Å $\times 100$ Å superlattice and a ZnTe epilayer grown on GaSb substrates. The full width at half maximum (FWHM) of the superlattice peak is about 5-6 meV, indicating high crystal quality. The band-edge of the superlattice is red shifted from the ZnTe band gap, because of the Cd-rich well layers. The ZnTe buffer-layer shows a strong, bound exciton line, indicating very good material quality. We find that the photoluminescence intensity of $Zn_{1-x}Cd_xTe$-ZnTe superlattices is stronger than ZnTe buffer-layers by ≈ 2 orders of magnitude, consistent with observations by others.[20] We have assigned the superlattice peaks to the heavy-hole free exciton.

$ZnTe_{1-x}Se_x$-ZnTe Samples

$ZnTe_{1-x}Se_x$ Alloys and superlattices		Se conc.	Buffer layer	Layer thickness	PL peak
Sample #	Sample description	(x)		(Å)	(meV)
II-49	ZnTe-$ZnTe_{1-x}Se_x$ SL	0.39	ZnTe	20(75 × 75)	1950
II-56	$ZnTe_{1-x}Se_x$ epilayer	0.14	ZnTe	1 μm	2210
II-59	$ZnTe_{1-x}Se_x$ epilayer	0.39	ZnTe	1 μm	2125
II-70	ZnTe-$ZnTe_{1-x}Se_x$ SL	0.14	ZnTe	20(75 × 75)	2170
II-73	ZnSe-$ZnTe_{1-x}Se_x$ SL	0.95	ZnSe	20(75 × 75)	2740
II-84	ZnSe-ZnTe SL	1.00	ZnTe	56(20 × 20)	1980

$Zn_{1-x}Cd_xTe$-ZnTe Samples

$Zn_{1-x}Cd_xTe$ Alloys and superlattices		Cd conc.	Buffer layer	Layer thickness	PL peak
Sample #	Sample description	(x)		(Å)	(meV)
II-29	ZnTe-$Zn_{1-x}Cd_xTe$ SL	0.22	ZnTe	20(100 × 62)	2211
II-33	ZnTe-$Zn_{1-x}Cd_xTe$ SL	0.34	$Zn_{.9}Cd_{.1}Te$	20(100 × 50)	2075
II-35	ZnTe-$Zn_{1-x}Cd_xTe$ SL	0.34	ZnTe	8(200 × 100)	2065
II-36	ZnTe-$Zn_{1-x}Cd_xTe$ SL	0.34	ZnTe	8(300 × 25)	2165
II-37	ZnTe-$Zn_{1-x}Cd_xTe$ SL	0.22	ZnTe	8(300 × 25)	2274
II-41	ZnTe-$Zn_{1-x}Cd_xTe$ SL	0.10	ZnTe	20(100 × 50)	2308
II-43	ZnTe-$Zn_{1-x}Cd_xTe$ SL	0.22	ZnTe	20(100 × 62)	2192
II-66	$Zn_{1-x}Cd_xTe$ epilayer	0.34	ZnTe	1 μm	2118
II-67	$Zn_{1-x}Cd_xTe$ epilayer	0.14	ZnTe	1 μm	2212

Table 4.2: Table of $ZnTe_{1-x}Se_x$-ZnTe and $Zn_{1-x}Cd_xTe$-ZnTe samples used in the optical investigations of the band alignments.

By comparing the photoluminescence energy shifts for a series of seven superlattice samples, we were able to obtain the valence band offset. From our data on the alloy superlattice samples, we have extrapolated to the binary CdTe-ZnTe values by using a linear extrapolation. The best fit for the valence band offset of CdTe-ZnTe we find is (-50 ± 160 meV), where the CdTe valence band-edge lies lower than that of ZnTe.

For the case of the $Zn_{1-x}Cd_xTe$-ZnTe system, we find that it is difficult to obtain the value of the valence band offset by the optical technique described here. It is easy to understand this shortcoming by considering a type I superlattice. In this case, the superlattice band gap is quite insensitive to the band offsets since electrons and holes sense very little of the top of the barrier. Thus, it is difficult to convert a measurement of the superlattice band gap to a corresponding value for the valence band offset; small uncertainities in the band gaps become amplified into large uncertainities in the band offsets. On the other hand, this technique works remarkably well if the band alignment is type II. We find that the $Zn_{1-x}Cd_xTe$-ZnTe situation lies at the boundary of the validity range of this method (intermediate between type I and type II). Therefore, we find that it is quite difficult to obtain an upper bound to the valence band offset, although it is easier to obtain a lower bound.

$ZnTe_{1-x}Se_x$-ZnTe Superlattices

In Fig. 4.6(a) and 4.6(b), the photoluminescence spectra of $ZnTe_{1-x}Se_x$-ZnTe superlattices for Se alloy compositions of x=.39 and x=.14 are shown. The photoluminescence of the superlattices is significantly red-shifted from the corresponding bulk alloys, indicating a type II band alignment. The photoluminescence line widths are 20-40 meV, with increased line widths for the higher Se composition sample. These are the first reported $ZnTe_{1-x}Se_x$-ZnTe superlattices grown by MBE, and much of the nature of the photoluminescence and physics of the interfaces is only poorly understood. Nevertheless, for the purpose of obtaining the band offsets, we have assigned the photoluminescence peaks to the band-edges.

The results we obtain for the offsets of $ZnTe_{1-x}Se_x$-ZnTe samples are shown in Fig. 4.7. We have plotted the valence band position of the $ZnTe_{1-x}Se_x$ alloy, compared to the valence band position of ZnTe. The error bars correspond to the experimental uncertainities in the samples and the uncertainties in the theoretical parameters. The upper curve with the conduction band position was generated by adding the band gap to the valence band position. The results indicate that the component of bowing in the valence band is quite small, and a linear interpolation for the valence band offset is justified even in the presence of large band gap bowing.

However, since the nature of the photoluminescence from $ZnTe_{1-x}Se_x$-ZnTe superlattices is not completely understood, there can be a systematic discrepancy in the band offsets we obtain, that is not taken into account in the error bars. If the photoluminescence of the superlattices lie 100-150 meV below band gap, analogous to the situation in the $ZnTe_{1-x}Se_x$ alloys[39], then our results for the offsets should also be modified by approximately the same amount. This type of correction would always reduce the magnitude of the valence band offset we quote here. However, further investigations of the growth and photoluminescence from these novel superlattices are necessary to better understand the band offsets.

4.3.4 Discussion of Experimental Results

The results of our investigations indicate that the valence band offset for the CdTe-ZnTe system is quite small (-50 ± 160 meV), with the valence band-edge of CdTe lying lower than that of ZnTe. In this case, a n-CdTe/p-ZnTe heterojunction would have the possibility of hole injection. Thus, recombination could occur in the smaller band gap CdTe layer. This band alignment is not very promising for obtaining green light-emission from ZnTe. Our results on the ZnSe-ZnTe system

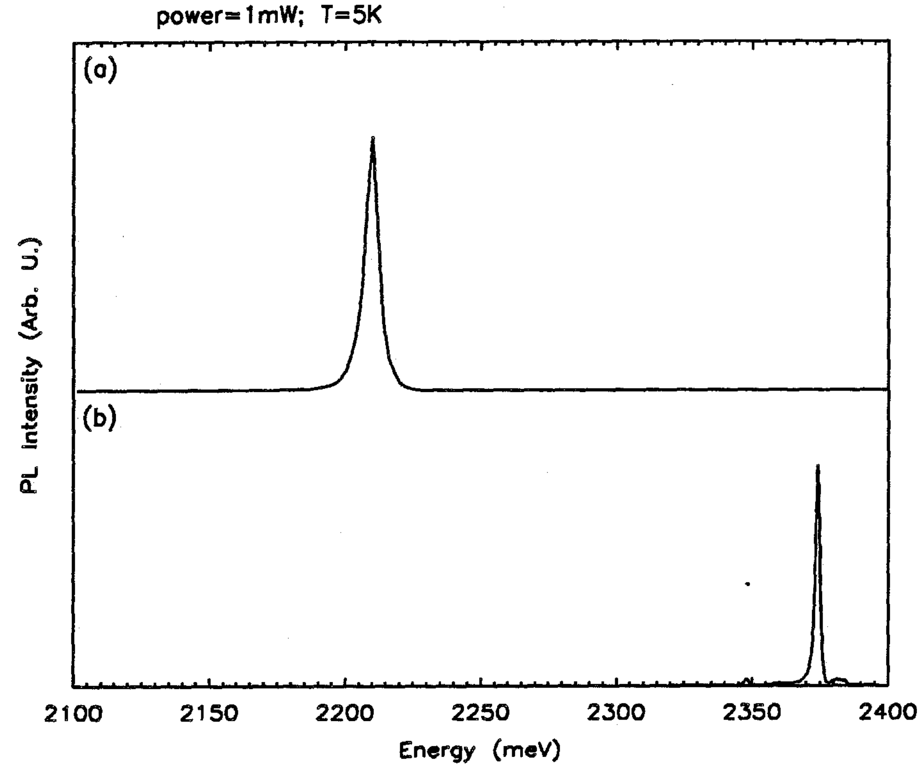

Figure 4.5: Photoluminescence of a $Cd_{.22}Zn_{.78}Te$-ZnTe 62 Å × 100 Å superlattice (a), and a ZnTe epilayer grown on a GaSb buffer-layer (b).

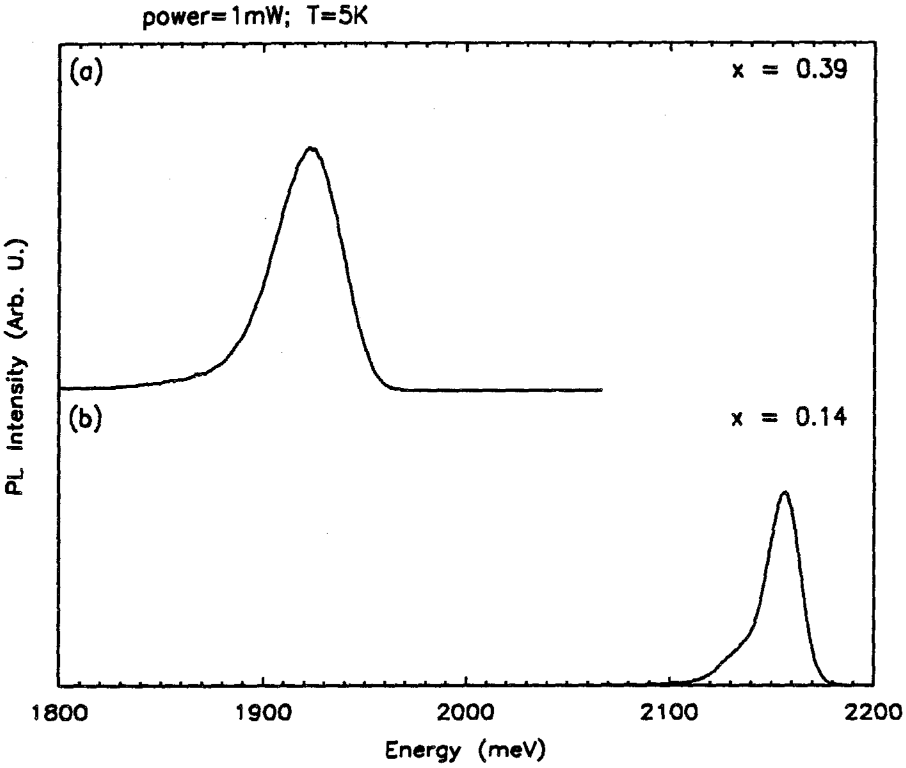

Figure 4.6: Photoluminescence of $ZnTe_{1-x}Se_x$-ZnTe superlattices. The spectra correspond to 75A × 75A superlattices, with Se fractions x as indicated in the figure.

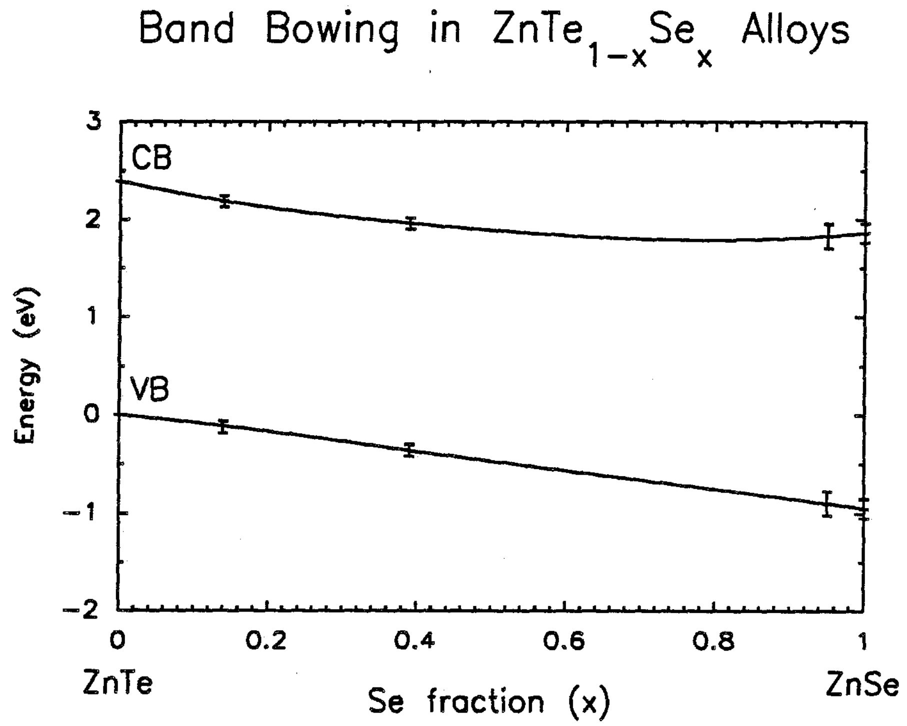

Figure 4.7: Valence band positions of ZnTe$_{1-x}$Se$_x$ alloys obtained by fitting the photoluminescence data by $\vec{k} \cdot \vec{p}$ theory. Notice that the bowing component in the valence band is quite small. The conduction band positions were plotted by adding the band gaps to the valence band positions.

suggest that the valence band offset is quite large (-907 ± 120 meV), with the valence band-edge of ZnSe lying lower than that of ZnTe. A heterojunction between n-ZnSe/p-ZnTe would be a poor candidate for minority carrier injection since both electrons and holes are blocked by the large band offsets.

Although the heterojunctions between the binaries are not very promising according to our results, there are interesting possibilities that arise in the ternaries, and the quaternaries. We have done the preliminary investigations of the band offsets of $Zn_{1-x}Cd_xTe$ and $ZnTe_{1-x}Se_x$ ternaries. We find that the common anion rule is obeyed quite well for the $Zn_{1-x}Cd_xTe$-ZnTe ternary, while a linear interpolation of the valence band offset between ZnSe and ZnTe is justified for $ZnTe_{1-x}Se_x$ ternaries. However, heterojunctions consisting of $Cd_xZn_{1-x}Se_yTe_{1-y}$ quaternaries seem to offer promise for band gap engineering, to obtain wide band gaps in the blue/green region of the spectrum and efficient minority carrier injection, with the additional benefits of improved lattice-match.

4.4 Theoretical Considerations of II-VI Quaternaries

The results of the band alignments of the II-VI ternary alloys such as $Zn_{1-x}Cd_xTe$ and $ZnTe_{1-x}Se_x$ investigated in Section 4.3 show only limited possibilities for minority carrier injection. In this section we have theoretically extended our analysis to II-VI quaternaries with Cd and Mn cations alloyed with $ZnTe_{1-x}Se_x$ ternaries, to overcome some of the limitations of the ternaries, and to obtain optimized light-emitting structures.

4.4.1 Basic Issues

The main reason that motivates the consideration of quaternary alloys, despite the additional complexity in the growth of these materials, is the increased flexibility to tailor material properties such as band-edge positions. The use of quaternaries can enhance the dopability range of ternaries, offer wider band gaps, obtain separate confinement of light and carriers, and provide nearly lattice-matched structures.

To optimize the parameters for efficient light-emission, we consider the simple geometries shown in Fig. 4.8 for heterojunction light-emitters. Although there are several other considerations such as the requirement of ohmic contacts and techniques for efficient extraction of light, that are important from the device design point of view, for the purpose of this chapter we have limited our attention mostly to the issues of dopability, band alignments, availability of wide band gaps, and lattice-match. The light-emitting structures shown in Fig. 4.8 consist of two major parts. The first part is the doped injector region (denoted by N and P). The second part is the radiator region (quantum well denoted I). The radiator region is chosen to have valence and conduction band-edge positions such that the carriers in the n and p regions can easily drop into the quantum wells, and recombine efficiently. The two diagrams of Fig. 4.8 show that it is possible to achieve favorable light-emitting structures with either type I, or type II band alignments.

Dopability

To determine the doping possibilities for n- and p-type material, we have made the assumption that the dopability of semiconductors is related to the absolute positions of the band-edges. This is quite a reasonable assumption that seems to hold true empirically for many semiconductors and dopants.[8] We present the following theoretical argument for the justification of this assumption. However, a further discussion of this assumption will be given in Section 5.2. Dopants usually induce states in either the band gaps or the allowed energy bands (valence and conduction bands) of semiconductors. For instance, if an n-type dopant induces a state in the conduction band, or if a p-type dopant induces a state in the valence band, then the

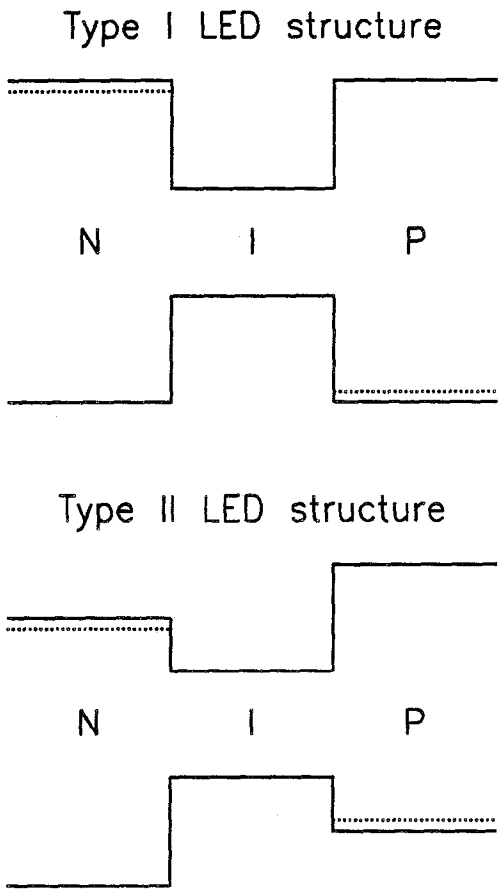

Figure 4.8: Type I and type II light-emitter structures. The injector regions are the wider band gap n- and p-type cladding layers (denoted by N and P), while the radiator region is the smaller band gap quantum well region (denoted by I). The conduction and valence band offsets of these structures help to confine the carriers in the quantum wells. Both type I and type II band alignments between n and p layers can be used effectively to obtain efficient light-emitting heterostructures.

resulting material has a shallow donor or acceptor level, respectively. However, if the state induced by the dopant lies deep within the band gap of the semiconductor, then the material has poor electrical properties, and is considered undopable in the usual terminology. The basic assumption is that from semiconductor to semiconductor the states induced by the dopants do not change their energy positions very much on an absolute energy scale, while the band-edge positions can change in energy significantly.[41] For instance, a shallow donor in a given semiconductor can be a deep impurity in another semiconductor, depending on the conduction band-edge position. Given this premise, we have explicitly assumed that the absolute positions of the band-edges of a material can determine its dopability.

In the case of ZnSe and ZnTe, ZnTe can be easily doped p-type while ZnSe cannot be doped easily p-type. Consistent with our picture, we argue that the p-type dopability of a $\mathrm{ZnTe}_{1-x}\mathrm{Se}_x$ ternary alloy should be related to its valence band-edge position. Similarly, the n-type dopability of a $\mathrm{ZnTe}_{1-x}\mathrm{Se}_x$ ternary alloy should be related to its conduction band-edge position. Thus, determining the bowing in the valence and conduction bands provides important information about the dopability of the ternary alloys. To invoke our prescription of dopability, material band-edges have to be lined up on an absolute energy scale. Theories such as Harrison,[32] Harrison and Tersoff[27] provide such scales, however, with large discrepancies with experimental results. In this section we have used the experimental band offset values we obtained from our optical investigations to determine the band lineup of $\mathrm{ZnTe}_{1-x}\mathrm{Se}_x$ and $\mathrm{Zn}_{1-x}\mathrm{Cd}_x\mathrm{Te}$ ternaries.

However, it should be kept in mind that this criterion for determining dopability is rather empirical, and its validity may depend on specific factors such as which dopants, which semiconductors, and which band alignments are considered. In the following analysis, we have used particular thresholds for the conduction band and valence band-edge positions to determine the n- and p-type dopability limits of the quaternaries; these thresholds were picked to agree reasonably with the limited experimental data available on the dopability of the ternary alloys.[42]

Interpolation Scheme for Quaternaries

In most calculations of this section, the physical properties of quaternary alloys are determined by a bilinear interpolation scheme between the properties of the four binaries given by

$$\begin{aligned} F(Zn_{1-x}Cd_xTe_{1-y}Se_y) &= (1-x)(1-y)F(ZnTe)+(1-x)(y)F(ZnSe) \\ &\quad +(x)(1-y)F(CdTe)+(x)(y)F(CdSe). \end{aligned} \tag{4.5}$$

Here, F is a property of the material such as its lattice constant, and x and y denote the Cd alloy fraction and the Se alloy fraction, respectively. In the case of parameters that depend nonlinearly on the alloy compositions, (e.g., band gap bowing), we have performed an interpolation, taking into account the appropriate nonlinearities. Our experimental results for the valence band offsets of $\mathrm{Zn}_{1-x}\mathrm{Cd}_x\mathrm{Te}$ and $\mathrm{ZnTe}_{1-x}\mathrm{Se}_x$ alloys showed that a linear interpolation for the valence band offset was justified for ternary alloys.

4.4.2 $\mathbf{Zn}_{1-x}\mathbf{Cd}_x\mathbf{Te}_{1-y}\mathbf{Se}_y$ System

In this section, we present the results for lattice constant, and the band-edge positions for $\mathrm{Zn}_{1-x}\mathrm{Cd}_x\mathrm{Te}_{1-y}\mathrm{Se}_y$ quaternary alloys, and discuss the possibility for a type II light-emitting heterostructure as in Fig. 4.8. In Fig. 4.9, we show the lattice-matched contour lines for $\mathrm{Zn}_{1-x}\mathrm{Cd}_x\mathrm{Te}_{1-y}\mathrm{Se}_y$ quaternaries. In device design, it is desirable to have the n- and p-type injector layers lattice-matched to each other, to minimize the detrimental effects from dislocations. Notice that in the case of $\mathrm{Zn}_{1-x}\mathrm{Cd}_x\mathrm{Te}_{1-y}\mathrm{Se}_y$ quaternaries, lattice-match lines are roughly parallel to the CdSe-ZnTe diagonal of Fig. 4.9.

In the Figs. 4.10, 4.11 and 4.12 we show the conduction band positions, valence band positions, and the band gaps of the $Zn_{1-x}Cd_xTe_{1-y}Se_y$ quaternary alloys, respectively. All data for the band gaps correspond to 5K values. The band lineups are calculated according to the results of our optical investigations, with ZnSe-ZnTe and CdTe-ZnTe valence band offsets of -907 and -50 meV, respectively. We have assumed that the common anion rule is obeyed by CdSe-ZnSe heterojunctions.

In Fig. 4.10 we have assumed that the n-type doping is not possible for material with conduction band-edges above $\approx$+100 meV, higher than the conduction band-edge of ZnSe. The dark region of Fig. 4.10 indicates the n-type dopable region. Notice that according to our criteria most of the quaternary is n-type dopable, with the exception of a small area near the ZnTe corner of Fig. 4.10. The large bowing in the contour lines of Fig. 4.10 result from the fact that we have assigned all of the bowing to the conduction bands, consistent with our experimental results.

Similarly, we have assumed that the p-type doping is not possible for material with valence band-edges lower than $\approx$600 meV below the valence band edge of ZnTe. The dark region of Fig. 4.11 indicates the p-type dopable region. Notice that according to our criteria, the region of the quaternary that is p-type dopable has a Te fraction above $\approx$35% as shown in Fig. 4.11. In the valence band positions, there is only a very small component of bowing. The thresholds for determining dopability were picked to encompass the dopability data of the $ZnTe_{1-x}Se_x$ alloys given by Aven and Garwacki.[42]

The intersection of the dark regions of Figs. 4.10 and 4.11 shows the quaternaries where p-n junctions are allowed. Although this is a significant fraction of the alloy composition space, however, if we limit the band gaps to above 2.10 eV (light-emission above yellow), then the region of interest shrinks to a small area near the middle of the $ZnTe_{1-x}Se_x$ ternary alloys with small Cd fractions. In Fig. 4.12 we present the band gap of the quaternary as a function of the alloy composition. The

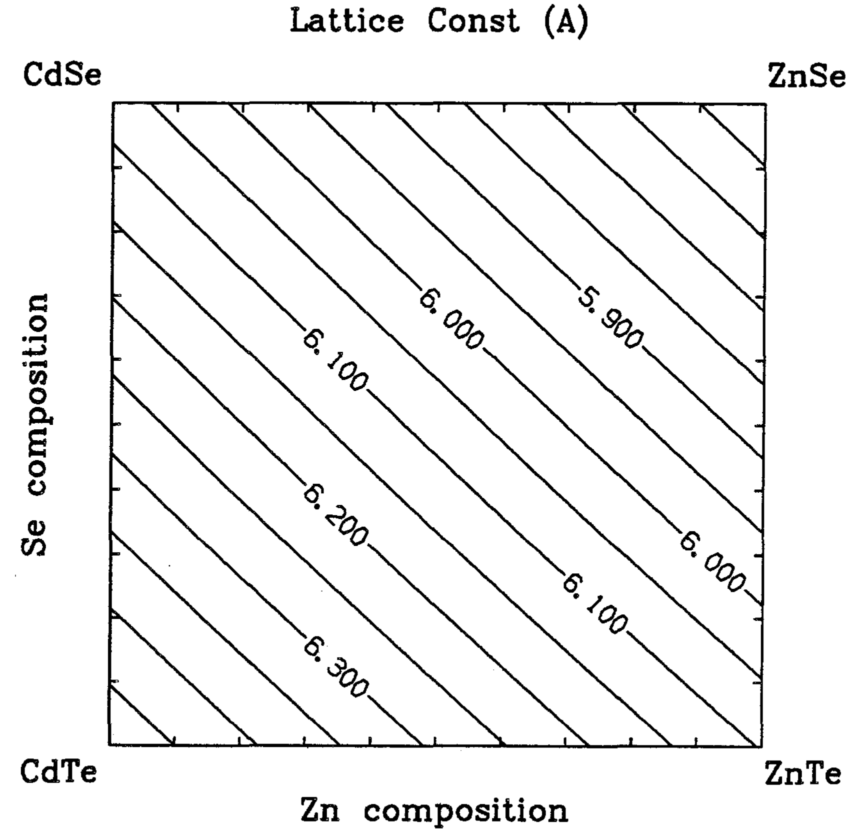

Figure 4.9: Contour plot of the lattice constant of $Zn_{1-x}Cd_xTe_{1-y}Se_y$ quaternary alloys. The lattice constants are given in Angstroms. The contour lines with equal lattice constant lie approximately parallel to the CdSe-ZnTe diagonal.

region with band gaps above 2.1 eV is shaded in light-gray. One possible way to pick the N, P, and I regions of a type II LED structure is shown in Fig. 4.12. It is possible to pick a combination of n and p layers that are lattice-matched to each other for quaternary heterostructures. However, the band alignment for $\mathrm{Zn}_{1-x}\mathrm{Cd}_x\mathrm{Te}_{1-y}\mathrm{Se}_y$ quaternaries makes it necessary to pick the I (quantum well) layer with a slightly larger lattice constant than the cladding layers ($\approx$1% lattice-mismatch), to obtain a favorable band diagram for a type II LED structure as shown in Fig. 4.8; it is not possible to obtain a type I LED structure that is suitable for green light-emission within $\mathrm{Zn}_{1-x}\mathrm{Cd}_x\mathrm{Te}_{1-y}\mathrm{Se}_y$ alloys.

Conclusions About $\mathrm{Zn}_{1-x}\mathrm{Cd}_x\mathrm{Te}_{1-y}\mathrm{Se}_y$ Quaternaries

Given the band alignment considerations, we have shown that it may be possible to achieve a type II heterojunction light-emitter. However, it is difficult to achieve band gaps above the range $\approx$2.1 eV (at room temperature) within the $\mathrm{Zn}_{1-x}\mathrm{Cd}_x\mathrm{Te}_{1-y}\mathrm{Se}_y$ quaternaries. Thus, this quaternary is of only limited usefulness for blue/green applications, although it offers excellent possibilities for yellow, orange and red light-emitting application. However, in interpreting these conclusions it should be kept in mind that we have made several empirical assumptions about dopability, and that there is still a fair amount of uncertainity about the band offsets that can change these conclusions.

4.4.3 Other II-VI Quaternary Systems

The limitation of not being able to achieve wide band gaps in the blue green region of the spectrum with $\mathrm{Zn}_{1-x}\mathrm{Cd}_x\mathrm{Te}_{1-y}\mathrm{Se}_y$ quaternaries can be overcome by replacing Cd with a different cation. We have chosen Mn as a candidate for studying the possibilities of a quaternary system with a wider band gap; the effect of alloying

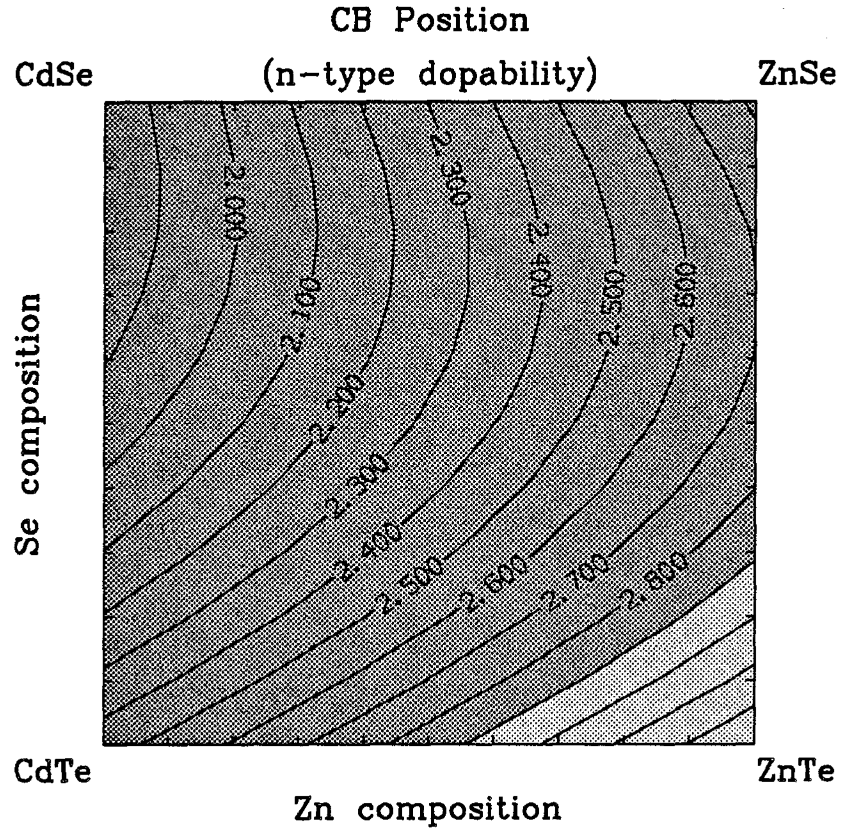

Figure 4.10: Contour plot of conduction band-edge of $Zn_{1-x}Cd_xTe_{1-y}Se_y$ quaternary alloys. In the figure, the dark region indicates the n-type dopable compositions. The energy positions are measured in eV, with respect to the valence band-edge of ZnSe. We have taken the n-type dopable region to be below 2.9 eV. The contour lines are curved because there is a large bowing in the conduction band positions.

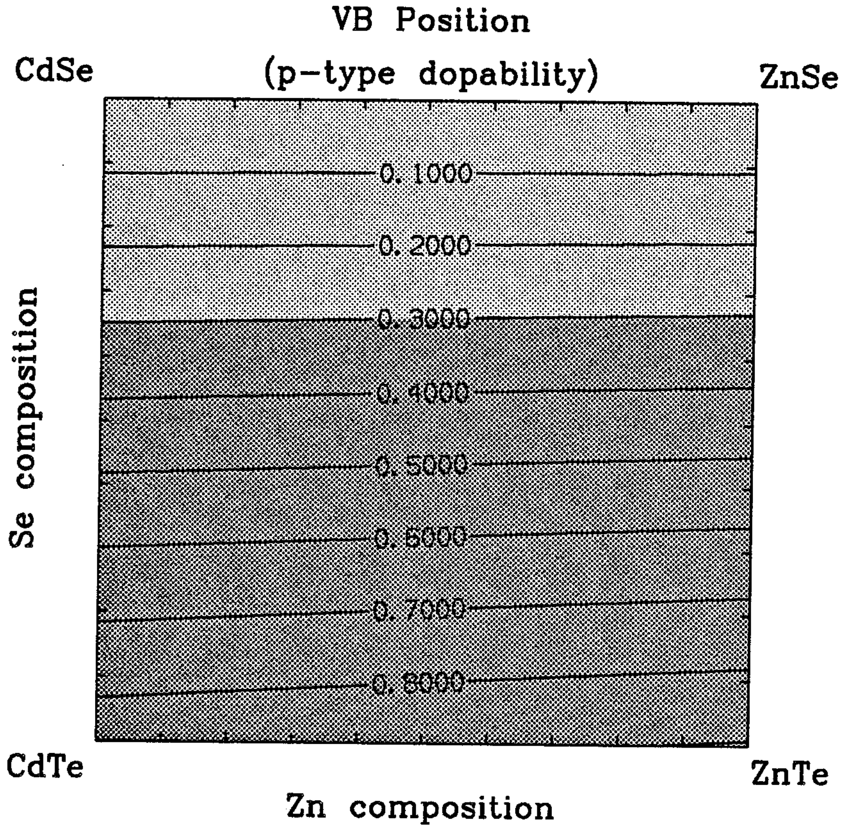

Figure 4.11: Contour plot of valence band-edge of $Zn_{1-x}Cd_xTe_{1-y}Se_y$ quaternary alloys. In the figure, the dark region indicates the p-type dopable compositions. The energy positions are measured in eV, with respect to the valence band-edge of ZnSe. We have taken the p-type dopable region to be above 0.3 eV. The contour lines are nearly straight lines because there is only a small component of bowing in the valence band positions.

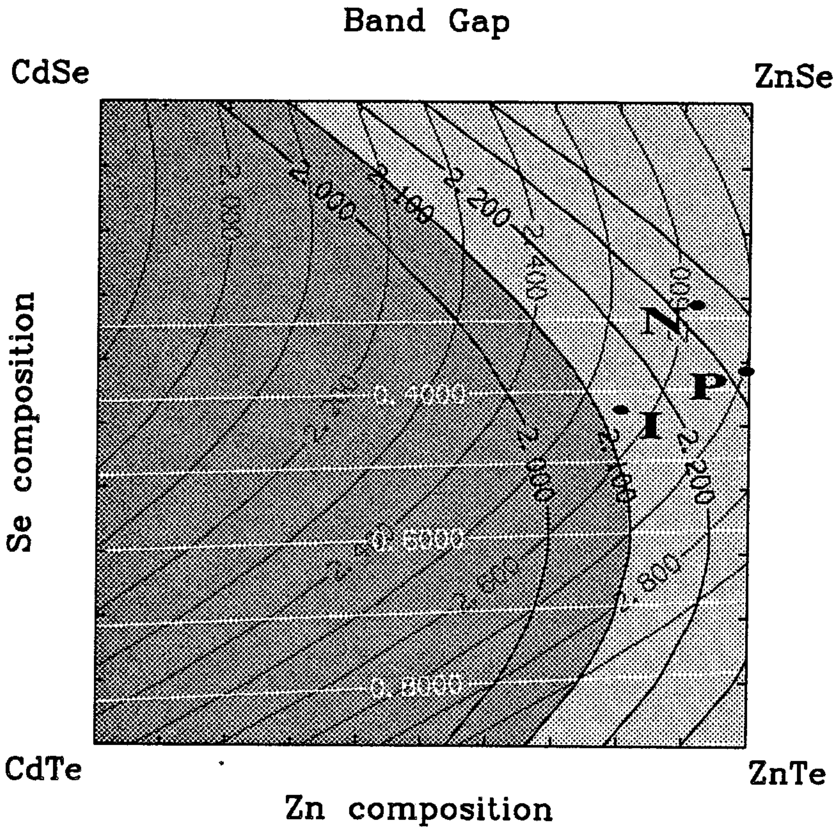

Figure 4.12: Band alignment of $Zn_{1-x}Cd_xTe_{1-y}Se_y$ quaternaries. The black contours denote the band gap of the alloy in eV. The light-gray region shows material with band gaps above 2.1 eV, suitable for wide band gap applications. The conduction and valence band positions are denoted by the gray and white contour lines, respectively. A possible set of layer compositions for a type II light-emitting structure is indicated by the points N, P, and I.

Mn to $Zn_{1-x}Cd_xTe$ ternaries usually increases the band gaps. We present the lattice constant, and band-edge positions for $Zn_{1-x}Mn_xTe_{1-y}Se_y$ quaternary alloys. In Fig. 4.13, we show the lattice-matched contour lines for $Zn_{1-x}Mn_xTe_{1-y}Se_y$ quaternaries. As in the $Zn_{1-x}Cd_xTe_{1-y}Se_y$ system, it is desirable to have the n- and p-type injector layers lattice-matched to each other, to minimize the detrimental effects from dislocations.

The band alignment results we present for the $Zn_{1-x}Mn_xTe_{1-y}Se_y$ system are very similar to the the case of the $Zn_{1-x}Cd_xTe_{1-y}Se_y$ system. Therefore, we present only the contour plot corresponding to Fig. 4.12, with all the information about the valence band positions, conduction band positions and the band gaps. All data for the band gaps correspond to 5K values. The values for the MnTe and MnSe band gaps were either estimated or extrapolated from the limited data available for these materials. The band lineups are calculated according to the results of our optical investigations, with a ZnSe-ZnTe valence band offset of -907 meV. We have assumed that the common anion rule is obeyed by MnSe-ZnSe, and MnTe-ZnTe heterojunctions.

In Fig. 4.14 we have assumed that the n-type doping is not feasible for material with conduction band-edges above ≈+100 meV higher than the conduction band-edge of ZnSe. The gray contour lines of Fig. 4.14 indicate the n-type dopable region. Notice that according to our criterion, only a small fraction of the quaternary near the ZnSe corner is n-type dopable. The large bowing in the band gap contour lines and the conduction band-edge contour lines of Fig. 4.14 result from the fact that we have assigned all of the bowing to the conduction bands, consistent with our experimental results.

Similarly, we have assumed that the p-type doping is not feasible for material with valence band-edges lower than ≈600 meV below the valence band edge of ZnTe. The white contour lines of Fig. 4.14 indicate the p-type dopable region. Notice that

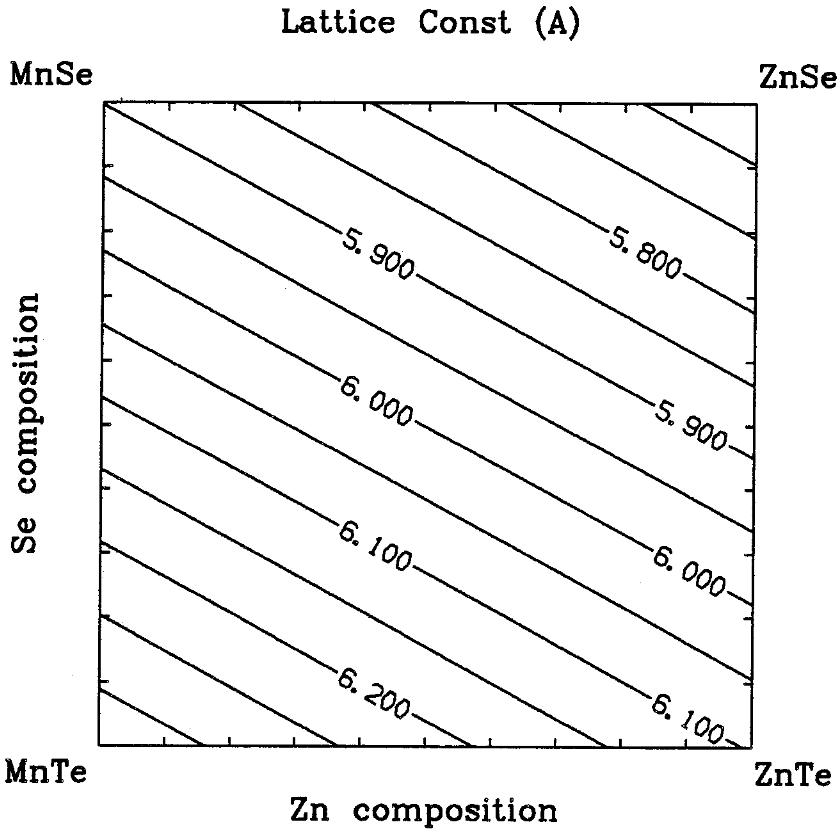

Figure 4.13: Contour plot of the lattice constant of $Zn_{1-x}Mn_xTe_{1-y}Se_y$ quaternary alloys. The lattice constants are given in Angstroms.

according to our criteria, the region of the quaternary that is p-type dopable, has a Te fraction above ≈35% as shown in Fig. 4.14. In the valence band positions there is only a very small bowing effect. The thresholds for determining dopability were picked to encompass the dopability data of the $ZnTe_{1-x}Se_x$ alloys given by Aven and Garwacki.[42]

The intersection region of the gray contour lines, and the white contour lines of Fig. 4.14 show the $Zn_{1-x}Mn_xTe_{1-y}Se_y$ quaternaries where p-n junctions are allowed. Although this is only a small region of the alloy composition space, however, it is possible to achieve band gaps above 2.3 eV (for light-emission in the blue/green region). In Fig. 4.14 we present the band gap as a function of the alloy composition. The region with band gaps above 2.3 eV is shaded in light-gray. One possible way to select the N, P, and I regions of a type I LED structure that has almost lattice-matched layers is shown in Fig. 4.14. In this case we have picked the N and P layers from the same composition.

Conclusions About $Zn_{1-x}Mn_xTe_{1-y}Se_y$ Quaternaries

Given the band alignment considerations, we have shown that it may be possible to achieve a type I heterojunction light-emitter. It is possible to achieve band gaps above the range ≈2.3 eV (at room temperature) within the $Zn_{1-x}Mn_xTe_{1-y}Se_y$ quaternaries, making this quaternary of great usefulness for blue/green applications, although it offers only a limited region where dopability may be possible. However, in interpreting these conclusions it should be kept in mind that we have made several empirical assumptions about dopability, and there is still a fair amount of uncertainity about the band offsets that can change these conclusions.

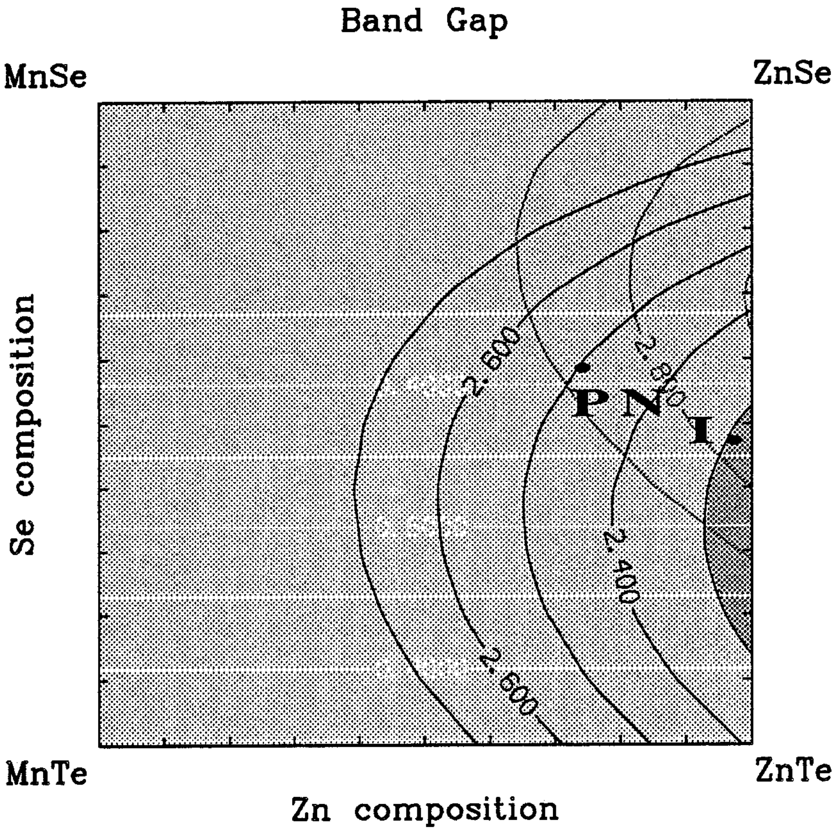

Figure 4.14: Band alignment of $Zn_{1-x}Mn_xTe_{1-y}Se_y$ quaternaries. The black contours denote the band gap of the alloy in eV. The light-gray region shows material with band gaps above 2.3 eV. The conduction and valence band positions are denoted by the gray and white contour lines, respectively. The band alignments are measured in eV. with respect to the valence band-edge of ZnSe. A possible set of layer compositions for a type I light-emitting structure is indicated by the points N, P, and I. The N and P layers were chosen to be identical.

4.5 Conclusions

In this chapter, we have shown that the heterojunction approach can be successfully employed to obtain wide band gap light-emitters capable of efficient minority carrier injection. In particular, we find that heterojunctions made of quaternary alloys offer excellent flexibility to obtain the desired properties such as wide band gaps, favorable band lineups for minority carrier injection, and lattice match. Although the long standing problems associated with doping wide band gap semiconductors in both n- and p-type have yet to be solved, we have shown that modern heteroepitaxial techniques can be successfully applied to circumvent some of these problems.

References

[1] M. Kobayashi, N. Mino, M. Konagai, and K. Takahashi, *Surf. Sci.* **174**, 550 (1986).

[2] M. Kobayashi, N. Mino, H. Katagiri, R. Kimura, M. Konagai, and K. Takahashi, *Appl. Phys. Lett.* **48**, 296 (1986).

[3] F. A. Kroger, in *The Chemistry of Imperfect Crystals*, North Holland, Amsterdam (1973).

[4] T. Yasuda, I. Mitsuishi, and H. Kukimoto, *Appl. Phys. Lett.* **52**, 57 (1987).

[5] J. Nishijawa, K. Hon, Y. Okuno and F. Sakurai, *J. Appl. Phys.* **57**, 2210 (1985).

[6] T. Yao in, *The Technology and Physics of Molecular Beam Epitaxy* , (Plenum Press, New York, 1985).

[7] H. Mitsuhashi, I. Mitsuishi, and H. Kukimoto, *J. Cryst. Growth* **77**, 219 (1986).

[8] J. O. McCaldin, *J. Vac. Sci. Technol* , to be published (1990).

[9] M. Konagai, in *Growth and Optical Properties of Wide-Gap II-VI Low-Dimensional Semiconductors*, edited by T. C. McGill, C. M. Sotomayor Torres and W. B. Gebhardt, Plenum, New York (1989).

[10] J. O. McCaldin, in *Growth and Optical Properties of Wide-Gap II-VI Low-Dimensional Semiconductors*, edited by T. C. McGill, C. M. Sotomayor Torres and W. B. Gebhardt, Plenum, New York (1989).

[11] R. H. Miles, J. O. McCaldin, and T. C. McGill, *J. Cryst. Growth* **85**, 188 (1987).

[12] E. O. Kane, in *Semiconductors and Semimetals*, edited by R. K. Willardson and A. C. Beer, Academic, New York (1966).

[13] G. Y. Wu, in *Electronic Properties of II-VI Superlattices and III-V Tunnel Structures*, Thesis, California Institute of Technology (1988).

[14] P. Lawaetz, *Phys. Rev. B* **4**, 3460 (1971).

[15] D. L. Camphausen, G. A. N. Connell and W. Paul, *Phys. Rev. Lett.* **26**, 184 (1971).

[16] A. A. Kaplyanskii and L. G. Suslina, *Sov. Phys. Solid. State.* **7**, 1881 (1966).

[17] D. A. Berlincourt, H. Jaffe and L. R. Shiozawa, *Phys. Rev.* **129**, 1009 (1963).

[18] Y. Rajakarunanayake and T. C. McGill, *Phys. Rev. B.* **37**, 10212 (1988).

[19] G. L. Bir and G. E. Pikus, in *Symmetry and Strain-Induced Effects in Semiconductors*, Keter, Jerusalem (1974).

[20] R. H. Miles, in *Structural and Optical Properties of Strained-layer Superlattices*, Thesis, California Institute of Technology (1988).

[21] J. H. Van der Merwe, *J. Appl. Phys.* **34**, 123 (1963).

[22] C. A. B. Ball and J. H. Van der Merwe, in *Dislocations in Solids*, ,edited by F. R. N. Nabarro, North Holland, Amsterdam (1983).

[23] J. W. Matthews, in *Epitaxial Growth*, edited by J. W. Matthews, Academic Press, New York (1968).

[24] J. W. Matthews and A. E. Blakeslee, *J. Cryst. Growth* **27**, 118 (1974).

[25] R. People and J. C. Bean, *Appl. Phys. Lett.* **47**, 332 (1985).

[26] R. H. Miles, T. C. McGill, S. Sivananthan, X. Chu, and J. P. Faurie, *J. Vac. Sci. Technol.* **B5**, 1263, (1987).

[27] W. A. Harrison and J. Tersoff, *J. Vac. Sci. Technol.* **B4**, 1068 (1986).

[28] A. D. Katnani and G. Margaritondo, *J. Appl. Phys.* **54**, 2522 (1983).

[29] J. O. McCaldin, T. C. McGill and C. A. Mead, *Phys. Rev. Lett.* **36**, 56 (1976).

[30] J. Tersoff, *Phys. Rev. Lett.* **56**, 2755 (1986).

[31] A. G. Milnes and D. L. Feucht, in *Heterojunctions and Metal-Semiconductor Junctions*, Academic Press, New York (1972).

[32] W. A. Harrison, *J. Vac. Sci. Technol.* **14**, 1016 (1977).

[33] C. G. Van de Walle and R. M. Martin, *J. Vac. Sci. Technol. B* **3**, 1256 (1985).

[34] M. Kobayashi, N. Mino, H. Katagiri, R. Kimura, M. Konagai, and K. Takahashi, *J. Appl. Phys.* **60**, 773 (1986).

[35] Y. Rajakarunanayake and T. C. McGill, *J. Vac. Sci. Technol.* **B6**, 1354 (1988).

[36] Tran Minh Duc, C. Hsu, and J. P. Faurie, *Phys. Rev. Lett.* **58**, 1127 (1987).

[37] Y. X. Liu and T. C. McGill, *unpublished* , (1990).

[38] A. Ebina, M. Yamamoto, and T. Takahashi, *Phys. Rev.* **B6**, 3786 (1972).

[39] M. C. Phillips, Y. Rajakarunanayake, J. O. McCaldin, D. H. Chow, D. A. Collins, and T. C. McGill, *Proc. SPIE.* , to be published (1990).

[40] Y. Rajakarunanayake, B. H. Cole, J. O. McCaldin, D. H. Chow, J. R. Söderström and T. C. McGill, *Appl. Phys. Lett.* **55**, 1217 (1989).

[41] H. P. Hjalmarson, in *Studies in the Theory of Solids*, Thesis, University of Illinois, Urbana-Champaign (1979).

[42] M. Aven and W. Garwacki, *J. Appl. Phys.* **38**, 2302 (1966).

Chapter 5

The Role of Electric Fields in Suppressing Self-Compensation

5.1 Introduction

Low-temperature growth techniques such as MBE and MOCVD offer the possibility of producing material in thermodynamically metastable states. The development of techniques to control such metastability can lead to semiconductors with novel physical properties. As an example of such a technique, we show how the application of external electric fields during growth of wide band gap II-VI semiconductors can lead to a suppression of the self-compensation processes.

5.1.1 Background and Motivation

The general motivation behind the current study of II-VI semiconductors is to develop blue/green optoelectronic devices. This has remained a challenging problem, however, that is due in large part to the difficulties in achieving both n- and p-type doping in a single wide band gap II-VI semiconductor. In Chapter 4 we investigated the use of heterojunctions to provide carrier injection as an alternative to solving the selective doping problem for II-VI materials. We showed that the heterojunction approach could be successfully applied to circumvent doping problems and to achieve blue/green light-emission in II-VI quaternary heterostructures. In this chapter, we specifically address the problems of doping II-VI semiconductors, and propose approaches to control directly the factors that limit dopability.

Background on II-VI Doping

Extensive work in the 1960's suggested that self-compensation processes in wide band gap II-VI semiconductors occur through various defect complexes.[1] It was postulated that at high-temperatures the defect complexes and the original dopants reached thermodynamic equilibrium, producing donors and acceptors roughly equal in number, so that the resulting material had very poor electrical properties.[2, 3, 4] However, the actual degree of compensation depends on the choice of material as well as on the choice of dopant species. For instance, ZnTe could be easily doped *p*-type but compensated strongly when *n*-type doping was attempted, while ZnSe could be doped *n*-type but compensated strongly when *p*-type doping was attempted.

Work done in the 1970's however, suggested that extrinsic impurities in the wide-gap II-VI materials were responsible for the inability to achieve selective doping.[5] -[10] Impurities such as Cu were thought to induce deep impurity states in the band gaps of these materials, thereby degrading the electrical properties of II-VI's.[11] It was quite difficult to separate species such as Cu from the Zn compounds in bulk growth techniques used in the 1970's. The general conclusion of these studies was that if extrinsic impurities could be removed from the II-VI materials, the doping problems could be overcome.[6, 7]

Because of the extensive experimental evidence available to support both of these arguments, it seems reasonable to assume that both the extrinsic impurity problem and the intrinsic defect-associated compensation problem may have to be solved in some fashion before it is possible to achieve successful doping of the wide band gap II-VI's in both n- and p-types.

Implications of Novel Growth Techniques

Progress in heteroepitaxy in the 1980's has opened up several interesting possibilities for achieving selective doping in II-VI materials. II-VI MBE growth can be achieved at temperatures of 200-300 °C , much lower than bulk growth temperatures, which are usually in the range 1000-1200 °C . Experimental studies suggest that metastable regimes might exist at these low-temperatures, where the compensation processes associated with defect generation could be frozen out, or blocked by large kinetic barriers. Metastable growth techniques provide a promising approach for overcomming some of the difficulties associated with doping II-VI's. An additional advantage of these growth techniques is that it is possible to achieve high purity growth in an ultra high vacuum enclosure (such as MBE), making it is possible to minimize to incorporation of extrinsic species, such as Cu, into the II-VI epilayers.

Modern growth techniques have also allowed the introduction of new doping techniques such as planar doping[12] and modulation doping,[13] which may offer additional flexibility in doping II-VI heterostructures. Another recently developed growth technique, atomic layer epitaxy (ALE) allows the precise control of each monolayer of material grown, and may help to reduce self-compensation.[14]-[17] Finally, techniques such as photo-assisted molecular beam epitaxy (PAMBE) provide additional methods of controlling the growth and doping process in II-VI's.[18, 19] In this chapter we propose and investigate a new approach –electric field-assisted growth and doping of II-VI materials. We show that it is possible to achieve and control metastable material regimes by the application of external electric fields.

5.1.2 Summary of Results

In this chapter, we describe a technique for suppression of self-compensation processes in semiconductors – the application of external electric fields during crystal growth. We show that it is possible to enhance doping efficiency by kinetically burying uncompensated material produced metastably by the application of an electric field during growth by MBE. An obvious application of this technique is to improve the doping of wide band gap II-VI semiconductors, where selective doping in both n- and p-types is usually not feasible because of extensive self-compensation. In our calculations, the self-compensating species are modeled as charged, mobile species that are free to drift and diffuse under electric fields. In the case of MBE growth, we solve for the equilibrium of these species in a moving coordinate frame, and show that two important dimensionless parameters determine the effectiveness of suppressing self-compensation. The first dimensionless parameter that determines the doping profile is $D/\lambda v$, where D is the diffusion coefficient, λ is the Debye screening length, and v is the growth rate; the second dimensionless parameter is $qE\lambda/k_BT$, where q is the electron charge, E is the electric field, k_B is the Boltzmann constant, and T is the growth temperature. We have applied our analysis to the specific case of n-type doping in ZnTe, where we have assumed the self-compensating species to be A-centers[20, 21, 22]. The A-center is an acceptor complex with a donor and an adjacent cation vacancy, as shown in Fig. 5.1. Our results indicate that it should be possible to achieve n-type doped ZnTe through the application of substantial electric fields under otherwise normal MBE growth conditions. Theoretical results are presented for doping concentrations as functions of the growth rate and the applied electric field.

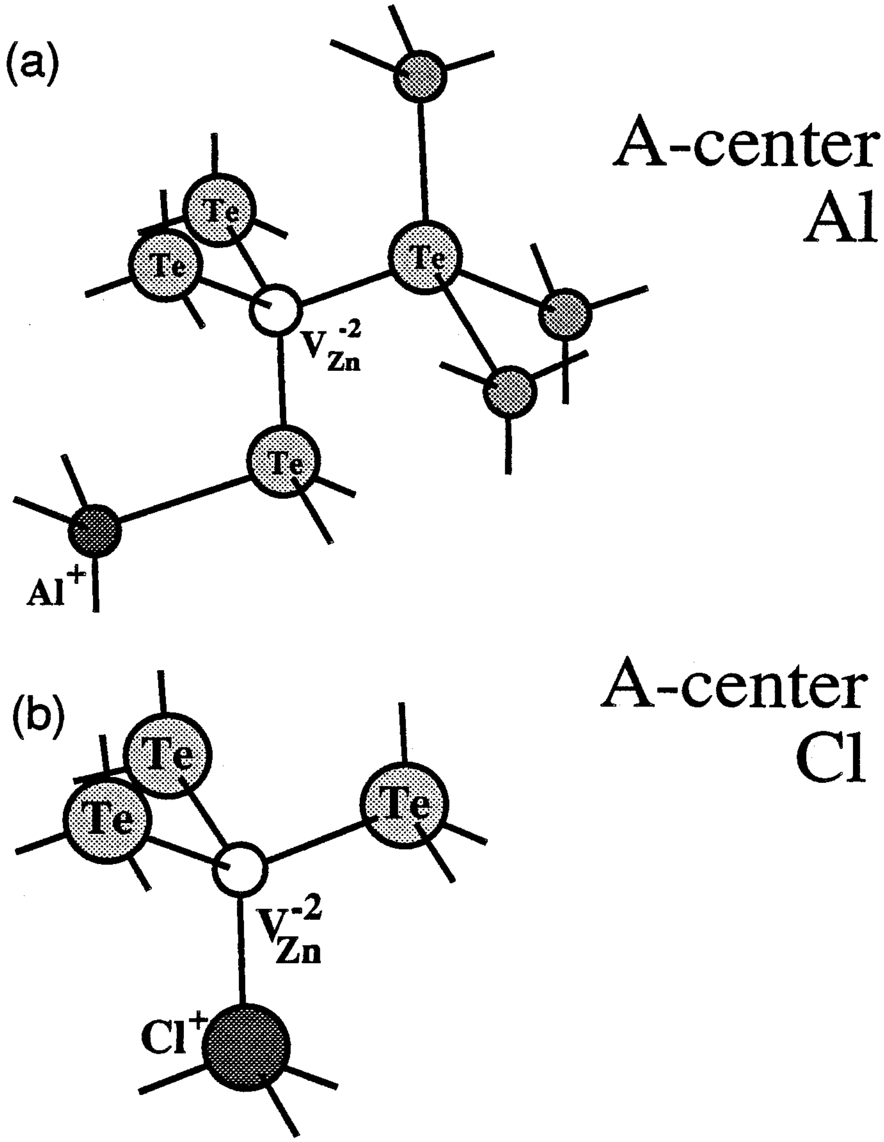

Figure 5.1: Schematic of two possible A-centers (donor-vacancy complexes) that can occur in a semiconductor such as ZnTe. The cation vacancy is denoted by V_{Zn}. In the case of doping on the cation lattice (Al), the vacancy resides on the next closest cation site. In the case of doping on the anion site (Cl), the vacancy resides on the nearest-neighbor cation site.

5.1.3 Outline of Chapter

In Section 5.2 we survey the reasons for the inability to dope wide band gap II-VI semiconductors, and discuss specific mechanisms that could limit dopability. In particular, we emphasize the compensation via vacancy-associated complexes such as A-centers. In Section 5.3 we discuss our approach to controlling the compensation process by applying external electric fields. We formulate and solve the equations governing the transport of compensating species during crystal growth under external electric fields. In Section 5.4 we describe the results for the doping efficiency obtained from the theoretical treatment of Section 5.3. Section 5.5 concludes the chapter.

5.2 Compensation in Wide-Gap II-VI Semiconductors

Narrow band gap semiconductors such as Si and GaAs can easily be doped either n- or p-type. However, it has not been easy to extend this success to doping the wider band gap II-VI materials. In the wider band gap II-VI's such as ZnSe and ZnTe, it is usually possible to achieve only one conduction type; ZnSe, for example can be doped only n-type while ZnTe can be doped only p-type. In this section we analyze the reasons for this inability to dope selectively wide band gap II-VI's from a general theoretical stand point. Many of the considerations of this section are presented as general arguments for the difficulties associated with doping II-VI's, based on empirical information and chemical trends. However, it should be kept in mind that the particular reason for the inability to dope a specific II-VI material may not be related to the reasons given here, and could change from material to material.

In a perfect II-VI crystal (such as zincblende ZnSe), a Group I element (e.g., Na) substituted on a cation site, or a Group V element (e.g., Sb) substituted on an anion site can act as an acceptor. Similarly, a Group III element (e.g., Al) substituted on a cation site, or a Group VII element (e.g., Cl) substituted on an anion site can act as a donor. However, substitutional incorporation is neither a necessary nor a sufficient criterion for obtaining shallow donor and acceptor levels that can lead to low resistivity n- or p-type material. We illustrate two ideas related to the inability to achieve selective doping in wide band gap II-VI's. In both these cases, we assume that the dopants are incorporated into appropriate substitutional sites, yet successful doping may not be possible. The first possibility we consider is that under certain conditions, shallow-deep transitions could prevent dopability. The second possibility is the formation of vacancy associated complexes that could prevent dopability. Although we have concentrated on these two issues, there are many other reasons quoted for the inability to dope II-VI's.[23]

5.2.1 Shallow-Deep Transitions

In general, dopants induce states in semiconductors, either within the band gap leading to deep traps, or within the allowed energy bands leading to shallow, hydrogenlike states. To better illustrate these two possibilities, let us consider a donor species such as Ga substituted on a cation site of a II-VI material such as ZnSe. In this case, there will be an (s-orbital like) Ga level induced in ZnSe, which can be occupied by up to two electrons (spin degeneracy). However, there will be only one occupying electron in this level because Ga has only one extra valence electron than Zn. If this donor level is induced within the conduction band of ZnSe, then the extra electron can drop from this level to the top of the conduction band (ionization). This electron at the conduction band-edge, and the ionized donor impurity can then further interact via the Coulomb interaction to form a hydrogenic donor atom, leading to the familiar shallow donor level near the conduction band-edge. However, the situation will be quite different if the original Ga donor level is induced below the conduction band-edge of ZnSe. In this case, the extra electron bound to the donor will not easily ionize. Furthermore, it will be able to trap an extra electron to the empty level that has been created within the band gap. In this situation, the donor not only fails to contribute its electron to the conduction band, but it can also act as a deep trap that can capture other conduction electrons to its empty state. Thus, these types of deep traps can have severely detrimental effects on the transport properties of semiconductors. A similar situation can occur for an acceptor state. However, the details are more complicated since there is a fundamental six-fold degeneracy to the (p-orbital like) levels in the valence band; in addition the spin-orbit interaction will complicate matters by splitting this degeneracy to give rise to a four-fold level near the valence band-edge region. Nevertheless, whether substitutional acceptors and donors act as electrically active species, or whether they act as deep traps will depend primarily on the position where the dopant level is induced, in relation to the appropriate band-edges.

Shallow-deep transitions are responsible for the inability to dope several semiconductors. This mechanism is illustrated in Fig. 5.2, adapted from the work of Hong and Dow.[24] Here we show that the position of the conduction band-edge can determine whether a substitutional donor is a shallow or a deep level. The main assumption here is that the position of the Ga level does not change much as Mn is alloyed with ZnSe. As the concentration of Mn increases, the conduction band-edge can move across the donor level, making it a deep level in $Zn_{1-x}Mn_xSe$, while it is a shallow donor in ZnSe. Extensive theoretical calculations indicate that these types of shallow-deep transitions should play an important role in determining the dopability of semiconductors.

As examples to illustrate the effects of shallow-deep transition in semiconductors, we consider two cases. Perhaps the best-known case of a shallow-deep transition occurs with N in $GaAs_{1-x}P_x$.[26, 27] Here N produces an isoelectronic deep level in the gap for $x > 0.2$. However, for $GaAs_{1-x}P_x$ alloys with smaller P content ($x < 0.2$),

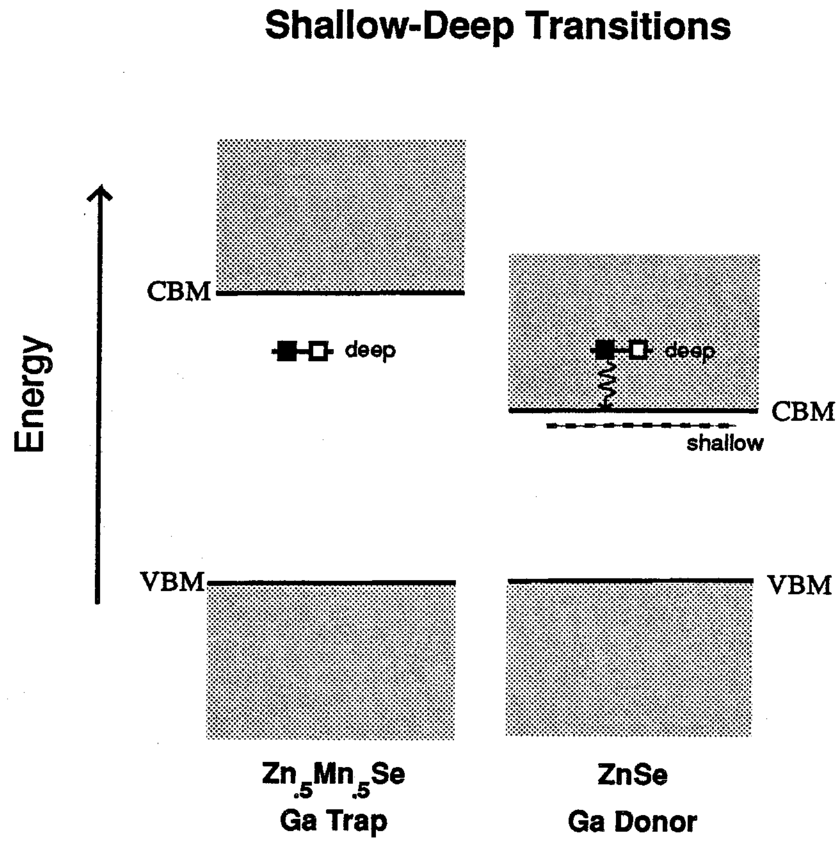

Figure 5.2: Band diagram of the shallow-deep transition in $Zn_{1-x}Mn_xSe$ alloys. In ZnSe, Ga is a shallow donor while in $Zn_{1-x}Mn_xSe$ ($x = 0.5$), it is a deep electron trap. These types of shallow-deep transitions can play a crucial role in determining the dopability of semiconductors. This idea is further discussed in Reference[24] .

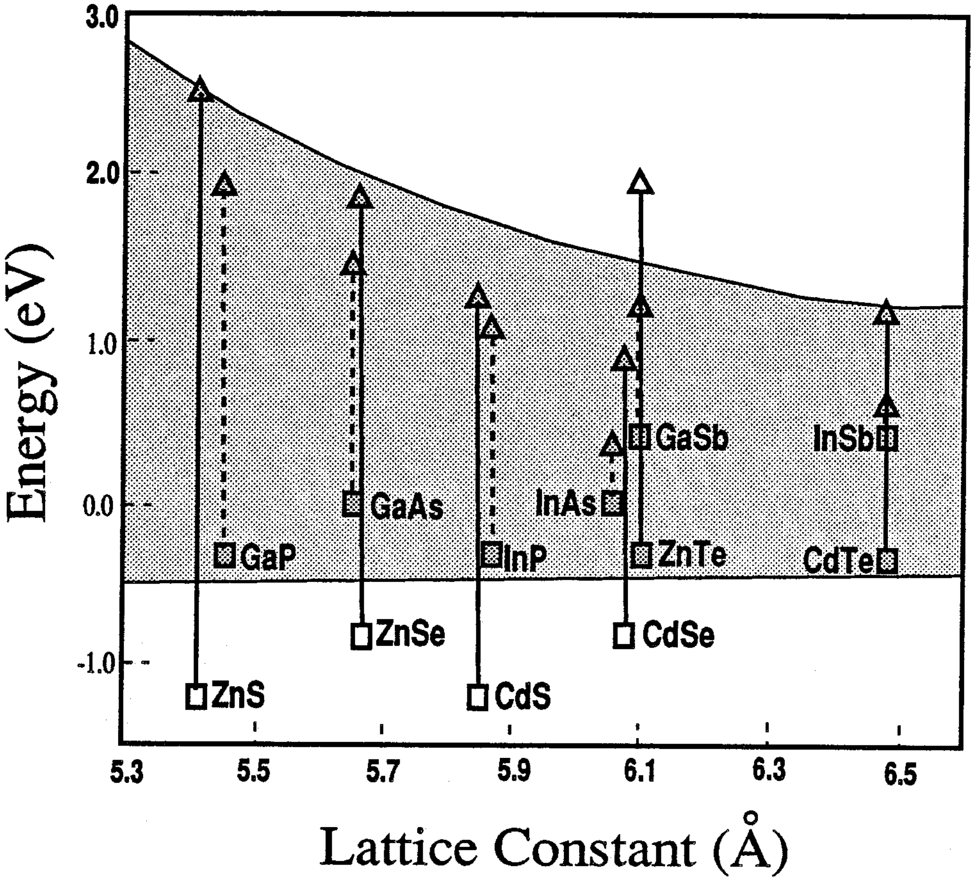

Figure 5.3: Semiconductor band alignment versus lattice constant. The positions of the band-edges have been determined using the band offset results of McCaldin et al.[25] The valence band-edges are denoted by squares, while conduction band-edges are denoted by triangles. The filled squares and triangles denote p- and n-type dopability, respectively. The shaded gray area is the general energy range where dopable material can be achieved. The II-VI band gaps are indicated by solid lines, while the III-V band gaps are indicated by dashed lines. Diagrams of this type are further discussed by McCaldin.[23]

this level moves above the conduction band-edge;[28]-[30] this is quite similar to the situation of Ga in $Zn_{1-x}Mn_xSe$ as illustrated in Fig. 5.2. The N isoelectronic states play an important role in the electrical and optical properties of $GaAs_{1-x}P_x$ alloys. As another prominent example of a shallow-deep transition, several researchers have argued that the DX-center in $Al_xGa_{1-x}As$ falls under this category.[31, 32] According to their theory, the DX-center is associated with a donor species such as Si, and descends from the conduction band of GaAs into the band gap of $Al_xGa_{1-x}As$ as x is increased. The DX-center is technologically important because it limits the fabrication of high electron mobility transistors (HEMTs). However, the origin of the DX-center itself is a topic of controversy, and the sole purpose of our mentioning it here is to illustrate that shallow-deep transitions can be quite common in semiconductors, and could play a profound role in determining electrical properties.

In Chapter 4 we analyzed the usefulness of II-VI quaternaries based purely on considerations of the band-edge positions. However, the validity of these assumptions can be loosely related to shallow-deep transitions in semiconductors. The main idea of the argument is that the levels induced by various dopants in semiconductors lie within certain energy bands of the band alignment diagram. If the conduction band of semiconductors occur too high in energy, then it becomes difficult to dope those semiconductors n-type, while if the valence bands of semiconductors occur too low in energy, then it becomes difficult to dope those semiconductors p-type. The various experimental data on dopability of semiconductors compiled by McCaldin[23] is shown in Fig. 5.3. Here, the absolute energy positions of the valence and conduction band are plotted based on the absolute energy scale suggested by the results of McCaldin et al.[25] The gray area indicates the n- and p-type dopable energy range. Although shallow-deep transitions are by no means the only factor that influences dopability of semiconductors, the experimental data of Fig. 5.3 is consistent with a picture where shallow-deep transitions play a crucial role.

5.2.2 Defect-Associated Complexes

Another major reason quoted for the inability to dope certain II-VI's is that many dopants can form alternate compensating species, rather than be incorporated substitutionally.[22] For instance, for n-type dopants in ZnTe, a donor can form either a simple substitutional, or it can form an A-center by the creation of a cation vacancy at an adjacent site. Depending on the specific thermodynamic conditions, the process of forming A-centers can compete with the process of simple substitutional doping. Analogous compensating complexes can also occur for p-type doping.[22] The Figs. 5.1(a) and 5.1(b) show two possible types of A-centers that can occur for Group III doping and Group VII doping of ZnTe, respectively. The energy difference between the A-center and the substitutional state will be the driving force for the compensation reaction. This can be estimated by considering the quantity $4B - 2E_g$, where B is the energy required to break a tetrahedral bond, and E_g is the band gap of the semiconductor. This expression results from the fact that to form an A-center it is necessary to break four bonds (to form the vacancy) and to change the charge state of the center by two units (convert $+e$ donors into $-e$ acceptors or, equivalently, moving two charges across the band gap). For structurally soft materials, such as wide band gap II-VI's, B is small, and E_g is large, so that $4B - 2E_g$ can be a negative number, indicating that it is thermodynamically favorable to form A-centers. In contrast, for structurally strong materials such as Si, with small band gaps, B is large, and E_g is small, so that $4B - 2E_g$ is typically a positive number. Thus, it is thermodynamically less favorable to form compensation complexes such as A-centers in Si.

In further agreement with this criterion, in materials such as CdTe, where the bond energies are small, but the band gaps are also small, it seems that the formation of A-centers can compete with the production of n-type material; specific conditions during growth can easily determine whether n-type or p-type material is produced. An annealing study done on CdTe[33] shows that it is possible to convert slightly *p*-type CdTe into *n*-type by heating in a Cd overpressure. Furthermore, reheating the CdTe in an enclosure without a Cd overpressure produces the original *p*-type material. These observations are consistent with the existence of cation vacancy associated complexes such as *A*-centers in CdTe.

n-Type ZnTe

Similarly, studies of ZnTe have shown that it has been possible to obtain *n*-type material at high-temperature; however, it has not been possible achieve *n*-type bulk ZnTe at low-temperature. Other reports indicate that it may be possible to obtain thin films of *n*-type ZnTe. This evidence suggests that the conduction band-edge of ZnTe is probably low enough for *n*-type dopability to be feasible with certain donors, and that the *n*-type doping problem is probably associated with the formation of compensating complexes such as *A*-centers. In this chapter, therefore, we have made the assumption that the solution to doping ZnTe *n*-type is to control the concentration of *A*-centers produced.

One possibility is to increase the partial pressure of the cations during the growth process, to suppress the cation vacancy formation, thereby suppressing *A*-centers. However, it is quite difficult to induce a large change in the Zn pressure within the parameter space allowed by growth processes such as MBE. Another possibility is to utilize atomic layer epitaxy (ALE) to grow cation layers with very little vacancy formation. This could also help to reduce the formation of *A*-centers. However, the approach taken in this chapter is more general, and attempts to control the metastable growth regimes by systematic approaches such as applying electric fields.

It is well-known that metastability can be controlled under certain circumstances. For instance, under low-temperature MBE growth conditions, it is possible to achieve MnTe in the cubic zincblende crystal structure, although the stable crystal structure obtained by high-temperature, bulk growth techniques is the hexagonal NiAs structure.[34] Recent attempts to dope ZnSe using Li suggest that p-type ZnSe can be obtained, although it may be metastable.[35, 36] We believe that low-temperature growth techniques may be the key to suppressing compensation phenomena in many of the wide band gap II-VI's. Many other techniques, such as photo assisted molecular beam epitaxy (PAMBE), have also been tried in an attempt to control these metastable growth regimes with external perturbations. Following the spirit of these approaches, in the next section we develop the electric field-assisted doping technique. We show that external electric fields applied during growth can significantly enhance the possibility of achieving n-type ZnTe.

5.3 Electric Field-Assisted Doping

In this section, we analyze the role of electric fields applied during epitaxial growth in suppressing compensation in semiconductors. We demonstrate that techniques such as the application of external electric fields should help to achieve and control metastability. The basic principle is that under electric fields, thermodynamic equilibrium is determined by the combined electro-chemical potential. Thus, material grown under these conditions could be frozen in metastable states when cooled down to room temperature, and the electric fields are turned off.

5.3.1 Basic Assumptions

In our analysis we consider the epitaxial growth of a semiconductor such as ZnTe, under an external electric field parallel to the growth direction. This epitaxial layer is assumed to be grown on a suitable buffer-layer using a growth technique such as MBE. Although there are nontrivial practical considerations that must be surmounted to achieve such electric fields within MBE growth chambers, for the purpose of this discussion we assume that it is a feasible task. The purpose of this analysis is to study how the compensation processes are altered by an external electric field.

We assume that during the growth process, there is a uniform density of n-type donors incorporated into the semiconductor. To simplify the analysis, we neglect any dependence of the donor-incorporation rate on the the applied electric field. We assume that under a zero electric field, the doping efficiency of the material is very poor; i.e., we assume that a large concentration of compensating species such as A-centers are formed such that the residual material has a roughly equal number of donors and acceptors, and that the Fermi level lies close to the midgap region. For the sake of simplicity, we assume that there is only one type of acceptor species responsible for the compensation, and that they are mobile, negative, and singly charged. This is the situation that corresponds to A-centers in ZnTe. For the rest of this discussion, we will refer to the compensating species as A-centers. However, the ideas developed in this section are quite general, and should apply for a variety of compensating species, as long as they obey the basic boundary conditions relevant for this analysis.

5.3.2 Boundary Conditions

One of the boundary conditions we assume in our analysis is that A-centers are formed only at the growth interface, and that they are free to drift and diffuse into the semiconductor. Under certain conditions, it may be possible to produce an interstitial and a residual vacancy deep inside the semiconductor;[22] however, we have ruled out such processes, assuming that they have a very large activation energy. Since the only sources of A-centers are at the growth interface, if the production rate of the A-centers at the growth interface can be suppressed, it should be possible to reduce the occurrence of these species in the bulk and obtain uncompensated material. If an external electric field is applied in a direction of positive band-bending for negatively charged species (the situation where the electric field points out of the semiconductor in the growth direction), then it should be possible to suppress the formation of A-centers at the growth interface. In this case, the combined electrochemical potential for the A-centers has to be considered; the resulting band-bending is very analogous to the band-bending of a semiconductor under bias, and arises purely from the electrostatic screening of the external field by the A-centers. In Fig. 5.4(a) we describe the anticipated band-bending diagram for the A-centers, in the moving coordinate frame of the growth front. We expect the depth profile of A-centers to be small near the growth interface, but increase inside the bulk to a steady-state value that is smaller than the donor concentration. This situation is illustrated in Fig. 5.4(b).

5.3.3 Theoretical Analysis

We denote the concentration of A-centers by N_A, and the current density of A-centers by J_A. Since we can assume that there are no sources of A-centers within the semiconductor, we can write the continuity equation

$$\frac{\partial J_A}{\partial x'} + \frac{\partial N_A}{\partial t'} = 0, \tag{5.1}$$

where the current can be expressed as

$$J_A = -D_A \frac{\partial N_A}{\partial x'} - \mu_A N_A E. \tag{5.2}$$

Here E is the electric field, and μ_A and D_A are the mobility and diffusion coefficient of A-centers, respectively. We have defined the mobility of the A-centers to be analogous to the electron mobility in semiconductors.[39] In writing the above equations we also assumed that the growth axis is the x-axis, and that there is no variation of the doping profile in the y and z directions. In the following analysis, most of the equations will be written in the coordinate frame of reference that moves with the growth front. We have reserved the independent variables x, and t for the moving

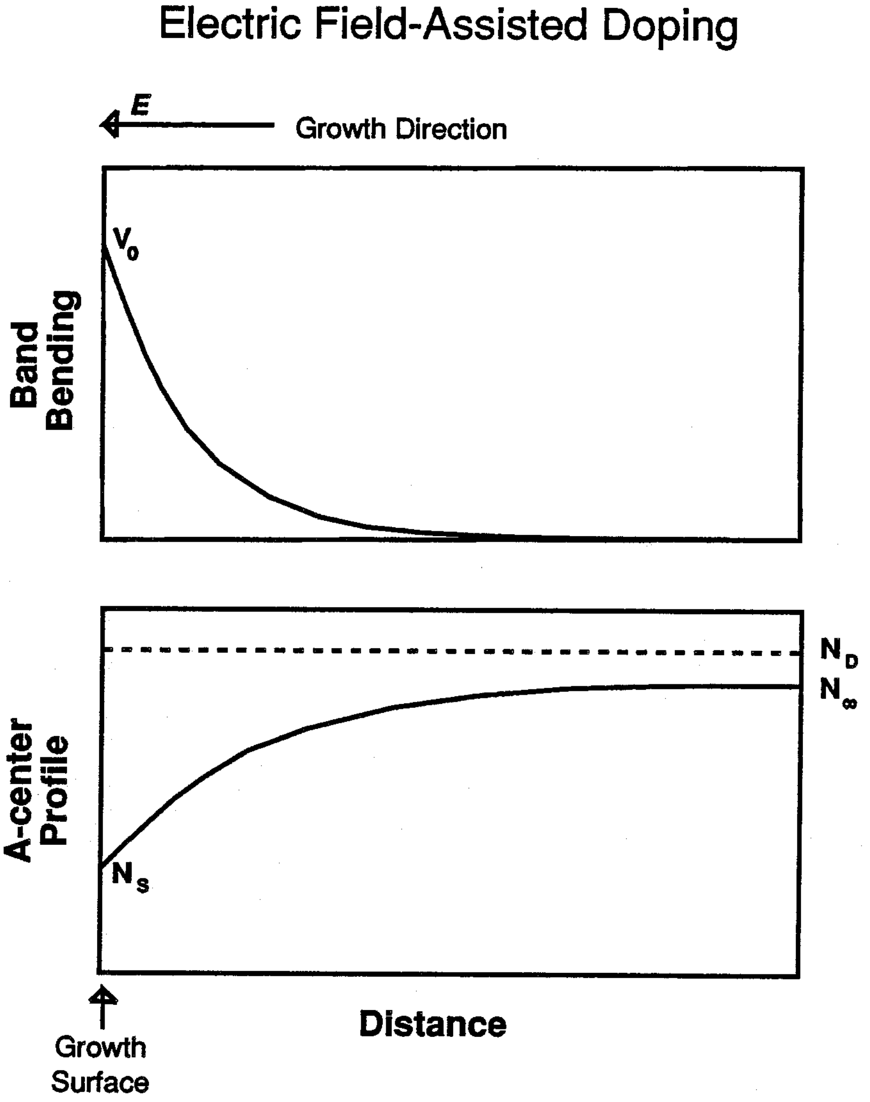

Figure 5.4: Schematic diagram showing the expected band-bending and the A-center profile for crystal growth under an external electric field. The distance is measured from the growth surface into the crystal. The growth surface is assumed to move at velocity v in the -x direction. The diagrams show the steady-state profiles in the moving coordinate frame.

coordinate system. To refer to the semiconductor's frame of reference, we reserve the independent variable x' and t'. This is the reason for the primes in Equations 5.1 and 5.2. It is possible to combine the above Equations 5.1 and 5.2 into the following second-order partial differential equation

$$\frac{\partial N_A}{\partial t'} = D_A \frac{\partial^2 N_A}{\partial x'^2} + \mu_A E \frac{\partial N_A}{\partial x'} + \mu_A \frac{\partial E}{\partial x'} N_A. \tag{5.3}$$

The most natural boundary conditions describing the stationary solution of the above equation under the appropriate conditions for epitaxial growth can be expressed in the moving coordinate frame that travels with the growth front. In the moving coordinate system, we expect the A-center concentration to reach a steady-state profile determined only by the initial conditions at the growth interface. In this coordinate system, we denote the independent variable by x and t. To incorporate these boundary conditions properly, it is necessary to convert the partial derivatives of Equation 5.3 into the moving coordinate frame. From the definitions of the quantities x and t,

$$x = x' + vt', \tag{5.4}$$

$$t = t', \tag{5.5}$$

we can derive the following relationships between the partial derivatives:

$$\frac{\partial N_A}{\partial x'} = \frac{\partial N_A}{\partial x}, \tag{5.6}$$

$$\frac{\partial^2 N_A}{\partial x'^2} = \frac{\partial^2 N_A}{\partial x^2}, \tag{5.7}$$

$$\frac{\partial N_A}{\partial t'} = \frac{\partial N_A}{\partial t} + v \frac{\partial N_A}{\partial x}. \tag{5.8}$$

In Equation 5.8 we have denoted the growth velocity by v. We have selected the positive direction of the x axis into the semiconductor so that in the coordinate frame of the crystal, the growth front travels in the -x direction at velocity v. Furthermore, if we use the relation that

$$E = -\frac{\partial \phi}{\partial x}, \tag{5.9}$$

where ϕ is the electrostatic potential, we can then define the potential V of a negatively charged species such as the A-center by $V = -\phi$. Using these relations in Equation 5.3, we obtain

$$\frac{\partial N_A}{\partial t} + v\frac{\partial N_A}{\partial x} = D_A\frac{\partial^2 N_A}{\partial x^2} + \mu_A\frac{\partial V}{\partial x}\frac{\partial N_A}{\partial x} + \mu_A\frac{\partial^2 V}{\partial x^2}N_A. \tag{5.10}$$

This equation has an additional convection term $(v\partial N_A/\partial x)$ in its left-hand side compared to Equation 5.3, because of the change into the moving coordinate system.

5.3.4 Stationary Solutions

To obtain the stationary solution, we set $\partial N_A/\partial t = 0$ in Equation 5.10, we can then rewrite Equation 5.10 as

$$\frac{\partial^2 N_A}{\partial x^2} + \left(\frac{\mu_A}{D_A}\frac{\partial V}{\partial x} - \frac{v}{D_A}\right)\frac{\partial N_A}{\partial x} + \left(\frac{\mu_A}{D_A}\frac{\partial^2 V}{\partial x^2}\right)N_A = 0. \tag{5.11}$$

The above differential equation is of the form,

$$\frac{d^2 N_A}{dx^2} + P(x)\frac{dN_A}{dx} + Q(x)N_A = 0, \tag{5.12}$$

where $P'(x) \equiv Q(x)$. The formal solution to equations of this form can be obtained by the method of adjoint operators as described by Morse and Feshbach[38]. The solution that does not diverge at infinity is

$$N_A = \mathcal{A}\ \exp^{\left(-\int^x P dx'\right)} \int^x \exp^{\left(\int^{x'} P dx''\right)} dx', \tag{5.13}$$

where, $\mathcal{A}$ is an arbitrary constant that will be determined later. The integrals in the above expression are indefinite integrals. In our case, the function $P(x)$ is given by

$$P(x) \equiv \frac{\mu_A}{D_A}\frac{\partial V}{\partial x} - \frac{v}{D_A}. \tag{5.14}$$

If we use the Einstein relation

$$\frac{\mu_A}{D_A} = \frac{q}{k_B T}, \tag{5.15}$$

to eliminate the mobility from Equation 5.14, we obtain the relation

$$\int P dx = \frac{qV}{k_B T} - \frac{vx}{D_A}, \tag{5.16}$$

where q is the magnitude of the electron charge. The Einstein relations are very general relationships that arise from the treatment of charged particles that obey Maxwell-Boltzmann statistics under thermal equilibrium considerations. Substituting Equation 5.16 into Equation 5.13, we obtain

$$N_A = \mathcal{A}\ \exp\left(-\frac{qV}{k_B T} + \frac{vx}{D_A}\right) \int^x \exp\left(\frac{qV}{k_B T} - \frac{vx'}{D_A}\right) dx'. \tag{5.17}$$

Further Assumptions

Until this point of the calculation it was not necessary to make any assumption about the form of the potential V. However, to proceed further than Equation 5.17 it is necessary to specify the form of V. An exact description of V requires a self-consistent solution of Equation 5.17 and Poisson's equation, given below

$$\frac{\partial^2 V}{\partial x^2} = \frac{q}{\epsilon}\left(N_D - N_A - n\right), \tag{5.18}$$

where N_D is the concentration of ionized donors incorporated into the semiconductor, and n is the concentration of free-electrons. For a first approximation we will assume that linear screening theory is valid, and the form of the potential V is specified by an exponential relationship of the form

$$V(x) \equiv V_0 \exp\left(-\frac{x}{\lambda}\right) = \lambda E_0 \exp\left(-\frac{x}{\lambda}\right). \tag{5.19}$$

Here λ is the screening length, and V_0 is the band-bending at the surface. We assume that V is measured from the chemical potential of the A-centers deep inside the semiconductor, where its value is selected to be zero. We have defined the absolute magnitude of the electric field near the semiconductor surface to be E_0. This electric field will usually point out of the semiconductor (in the $-x$ direction) under the conditions considered in this analysis. For now, we treat the screening length λ simply as a parameter in the equations, although in a later step of the analysis we will derive an explicit expression for λ similar to the Debye screening length. Linear screening is a good approximation if the condition $qV_0/k_BT \ll 1$ is satisfied. These substitutions into 5.17 yield

$$N_A = \mathcal{A}\ \exp\left(-\frac{q\lambda E_0}{k_BT}e^{-x/\lambda} + \frac{vx}{D_A}\right) \int^{x} e^{-vx'/D_A} \sum_{n=0}^{\infty} \frac{e^{-x'n/\lambda}}{n!} \left(\frac{q\lambda E_0}{k_BT}\right)^n dx'. \tag{5.20}$$

Here we have expanded the exponential inside the integral sign by the usual power series. If we perform the integrals of Equation 5.20, then we obtain

$$N_A = -\mathcal{A}\ \exp\left(-\frac{qV}{k_BT}\right) \sum_{n=0}^{\infty} \frac{\left(\frac{q\lambda E_0}{k_BT}\right)^n e^{-xn/\lambda}}{n!\left(\frac{v}{D_A} + \frac{n}{\lambda}\right)}. \tag{5.21}$$

We prefer to manipulate expression 5.21 because it is very easy to evaluate it numerically, although it is possible to obtain alternate analytic expressions. If we let $x \to \infty$ in Equation 5.21, we obtain

$$N_A(\infty) \equiv N_\infty = -\mathcal{A}\ \left(\frac{D_A}{v}\right). \tag{5.22}$$

Here, we have defined N_∞ as the concentration of A-centers deep inside the semiconductor. From the above relation, we can find the value of the arbitrary constant $\mathcal{A}$. Using N_∞, we can rewrite the Equation 5.21 for the doping profile as

$$N_A(x) = N_\infty \exp\left(-\frac{qV}{k_BT}\right) \left[\sum_{n=0}^{\infty} \frac{\left(\frac{q\lambda E_0}{k_BT}\right)^n e^{-xn/\lambda}}{n!\left(1 + \frac{nD_A}{v\lambda}\right)}\right]. \tag{5.23}$$

If we define the quantity in the square brackets of Equation 5.23 as a function F of the parameters $q\lambda E_0/k_BT$, $D/v\lambda$, and x/λ, then we can rewrite Equation 5.23 as

$$N_A(x) = N_\infty \exp\left(-\frac{qV}{k_BT}\right) F\left(\frac{q\lambda E_0}{k_BT}, \frac{D}{v\lambda}, \frac{x}{\lambda}\right). \tag{5.24}$$

Surface Boundary Conditions

At this point it is necessary to relate the concentration of A-centers at the surface to the doping concentration. We assume that under zero electric fields, complete compensation occurs. In this case, the concentration of A-centers at the surface N_S is equal to the uncompensated donor concentration N_D in the bulk. However, when the electric field is turned on, we assume that the concentration of A-centers at the surface will be suppressed by a Boltzmann factor with an activation energy equal to the band-bending at the surface. This is quite a reasonable assumption that would be valid if the A-centers at the surface obey Maxwell-Boltzmann statistics, and they are described by the chemical potential at equilibrium. This is a central assumption of our analysis, and is expressed mathematically by

$$N_S = N_D \exp\left(-\frac{qV_0}{k_B T}\right). \tag{5.25}$$

The combination of Equations 5.25, and 5.24 lead to an expression for the A-center profile in terms of the donor-incorporation rate N_D. With a little manipulation of the equations, this leads to the relation

$$N_A(x) \quad = \quad N_D \exp\left(-\frac{qV}{k_B T}\right) \left[\frac{F\left(\frac{q\lambda E_0}{k_B T}, \frac{D}{v\lambda}, \frac{x}{\lambda}\right)}{F\left(\frac{q\lambda E_0}{k_B T}, \frac{D}{v\lambda}, 0\right)}\right]. \tag{5.26}$$

5.3.5 Screening

At this point of our analysis, we will derive an explicit relationship for the screening length. If we simplify the Equation 5.23 for N_A, and retain only the first-order terms in the electric field E_0, then we obtain

$$N_A = N_\infty \left(1 - \frac{\frac{q\lambda E_0}{k_B T}}{1 + \frac{v\lambda}{D_A}}\right). \tag{5.27}$$

A similar relationship can be assumed for the electron concentration n,

$$n = n_\infty \left(1 - \frac{\frac{q\lambda E_o}{k_B T}}{1 + \frac{v\lambda}{D_e}}\right), \tag{5.28}$$

since electrons are also subjected to drift and diffusion. However, the diffusion coefficient for the electrons D_e is much larger than D_A for the A-centers, so in Equation 5.28 the term with $\lambda v/D_e$ can be neglected.

Now, substituting Equations 5.27 and 5.28 into the Poisson's Equation 5.18, we obtain

$$\frac{1}{\lambda^2} = \frac{q^2}{\epsilon k_B T}\left[\frac{N_\infty}{1+\frac{\lambda v}{D_A}} + N_D - N_\infty\right]. \tag{5.29}$$

To obtain the above equation, we used the relationship

$$N_D = N_\infty + n_\infty, \tag{5.30}$$

required by the charge neutrality condition deep inside the semiconductor. We can further simplify Equation 5.29 by substituting the expression for the Debye screening length given by

$$\lambda_D = \sqrt{\frac{\epsilon k_B T}{q^2 N_D}}. \tag{5.31}$$

If we define the dimensionless quantities $s \equiv \lambda/\lambda_D$, $\alpha \equiv q\lambda_D E_0/k_B T$ and $\beta \equiv D_A/\lambda_D v$, the screening parameter s can be expressed as

$$\frac{1}{s^2} = \frac{\beta + \alpha s^2}{\beta + s + \alpha s^2}. \tag{5.32}$$

From this relation, it is possible to obtain the correction to the screening length λ in the presence of electric fields, and moving coordinate frames. When $v \to 0$, then $\beta \to \infty$, and we obtain $s = 1$, in agreement with the classical Debye result.

5.4 Discussion of Results

In this section we present the results obtained for the electric field assisted doping, studied in the above section. First we will show results regarding the doping efficiency of the material grown by the electric field-assisted, doping technique. Second, we will show the compensation profiles calculated as a function of depth, to show that it is possible to obtain a reasonably uniform doping profile beyond a few screening lengths from the surface. The results presented correspond to the moving coordinate frame, and therefore indicate that arbitrarily thick layers of uncompensated material could be grown with this electric field assisted doping technique. We will also present results for the screening parameter s, to show that the classical Debye result is valid for the region of interest.

5.4.1 Doping Efficiency

In this section, we will present a plot of the doping efficiency $\eta = n_\infty / N_D$ as a function of the dimensionless parameters $D_A/\lambda_D v$ and $\lambda_D q E_0 / k_B T$. Here n_∞ is the electron concentration deep inside the bulk, and N_D is the incorporated donor concentration. Fig. 5.5 shows that it is quite possible to improve dramatically the doping efficiency by varying the parameter $\alpha \equiv \lambda_D q E_0 / k_B T$. This parameter can be further simplified using Equation 5.31 to give

$$\alpha \equiv E_0 \sqrt{\frac{\epsilon}{N_D k_B T}}. \tag{5.33}$$

We present results for the parameter α in the range [0.0-10.0]. It is possible to increase α by increasing the magnitude of the electric field E_0. Thus, the most straightforward way to improve the doping efficiency is to increase the strength of the external electric field. However, it is also possible to achieve a larger α by decreasing the temperature. This is reasonable, because the metastability is enhanced at lower temperature, and it is easier to achieve electric field enhanced doping at lower temperature. Furthermore, Equation 5.33 shows that an increase in the donor concentration also leads to a decrease in α.

There is only a small variation of the doping efficiency as a function of the parameter $D_A/\lambda_D v$. In Fig. 5.5 we have plotted the doping efficiency, assuming that the screening length is given by the Debye result. The results of Fig. 5.5 indicate

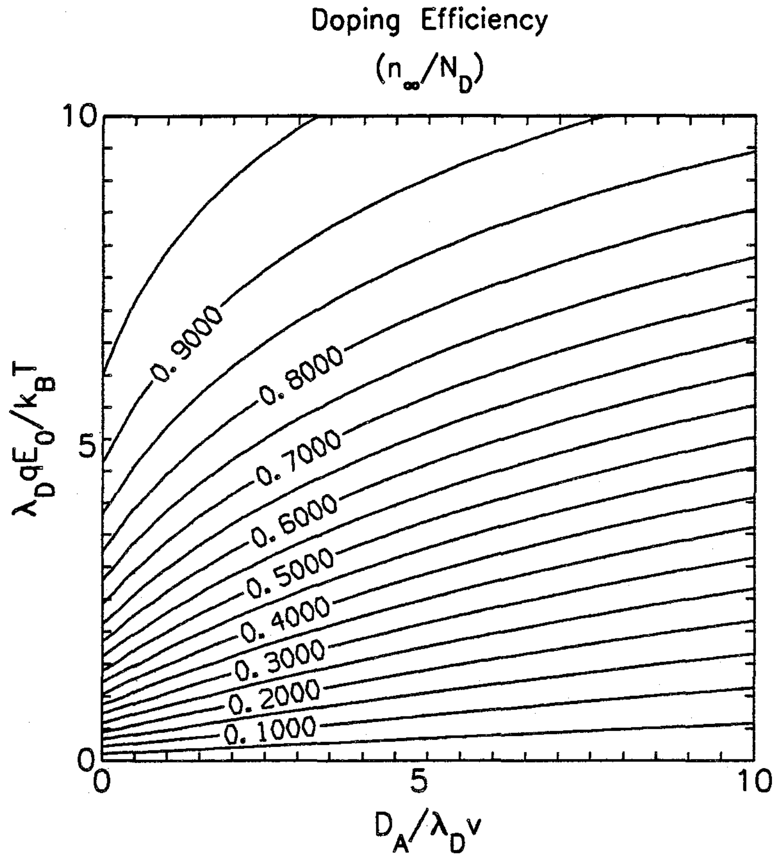

Figure 5.5: Contour plot of the doping efficiency as a function of the dimensionless parameters $\lambda_D q E_0 / k_B T$ and $D_A / \lambda_D v$. The doping efficiency can be significantly enhanced by increasing the electric field, while an increase in the growth rate produces only a slight enhancement of the doping efficiency. For the purpose of this plot, we assumed that the screening length is given by the Debye result.

that an increase in the growth velocity always increases the doping efficiency. This is quite reasonable, because faster growth helps to bury uncompensated material before the transport of A-centers can penetrate into the semiconductor. It seems that the parameter range of $D_A/\lambda_D v$ required to obtain a good doping efficiency in the epitaxial layer is $D_A/\lambda_D v$ <10.0.

5.4.2 Doping Profiles

In the next three figures, we have plotted the profile of $(N_D - N_A(x))/N_D$ for three different growth rates. We consider three cases - $D_A/\lambda_D v$ equal to .01, 1.0, and 100. - to illustrate the doping profile over a large range of parameter space.

Fast Growth Rates

For $D_A/\lambda_D v = 0.01$ growth occurs very fast compared to the diffusion/drift processes of A-centers. We have shown the results corresponding to this situation in Fig. 5.6. The boundary-layer in the A-center profile near the growth surface is much smaller than a screening length λ_D. Thus, we obtain an almost uniform profile of A-centers within the semiconductor. We show that it is possible to obtain an excellent doping efficiency at this growth rate if substantial electric fields (i.e., $\lambda_D q E_0/k_B T \approx 5$) are applied.

Moderate Growth Rates

For $D_A/\lambda_D v = 1.0$ growth occurs at a rate slow enough for the diffusion/drift processes of A-centers to compete with the rate at which uncompensated material gets buried. We have shown the results for this case in Fig 5.7. There is a boundary-layer region near the surface ($\approx$1-2 λ_D) where the concentration of A-centers is smaller than deep inside the semiconductor. The overall doping efficiency, however, is

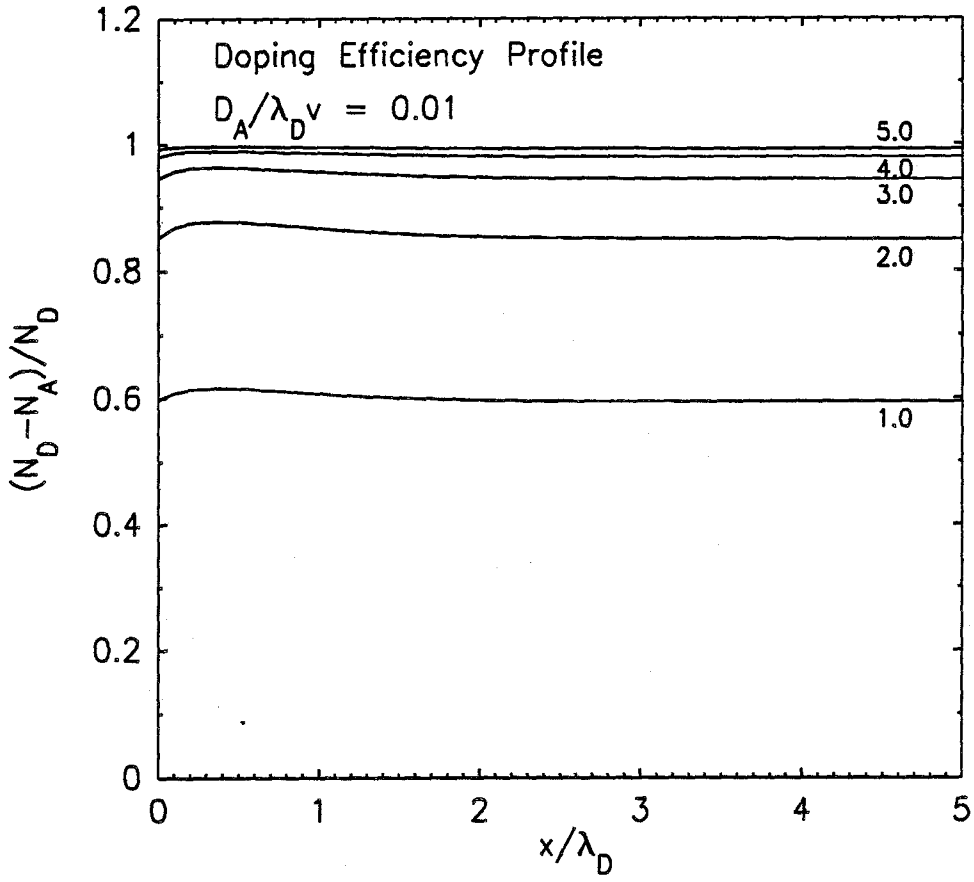

Figure 5.6: Doping profile $(N_D - N_A(x))/N_D$ is plotted as a function of the distance from the growth surface. The five curves labeled [1.0-5.0] correspond to the $\lambda_D q E_0/k_B T$ values for five different electric field strengths. This figure corresponds to a fast growth rate $D_A/\lambda_D v = 0.01$.

smaller than for the case of fast growth considered in Fig. 5.6. In this case it is still possible to obtain excellent doping efficiencies if large electric fields are applied.

Slow Growth Rates

For $D_A/\lambda_D v = 100.0$ growth occurs very slowly compared to the diffusion/drift processes of A-centers. We have shown the results corresponding to this situation in Fig. 5.8. We obtain a quite poor doping efficiency, and many of the advantages of the electric field-assisted doping are not fully realized at these slow growth rates. The boundary-layer near the surface extends deep into the crystal, and the eventual bulk doping efficiency achieved is quite poor. However, it is still possible to improve the doping efficiency slightly by increasing the electric field strength.

II-VI MBE Conditions

Although we have analyzed the results of the electric field-assisted doping technique in terms of dimensionless parameters, it is necessary to relate them to real physical situations such as the MBE growth of ZnTe to determine the feasibility of this technique. First we evaluate $D_A/\lambda_D v$. In the case of MBE, v can be about 1 monolayer per second. Assuming a doping concentration of 10^{18} cm^{-3}, the typical screening lengths are on the order of 100 Å. If we estimate the diffusion constant of A-centers by assuming that it is comparable to the self-diffusion coefficients in ZnTe at 300 °C ,[40] then we obtain $D_A \approx 10^{-14}$ cm^{2}s^{-1}, in this case the value of the parameter $D_A/\lambda_D v \approx 1$. This value of the diffusion coefficient is also similar to the value obtained by extrapolating the diffusivity data for CdTe given by Shaw.[41] The analysis of this chapter is therefore quite relevant for the n-type doping problem of ZnTe by electric field-assisted MBE. The typical electric field necessary to achieve substantial doping is determined by the parameter $\lambda_D q E_0/k_B T$. If the surface band-bending is 100 meV, and $k_B T$ is 50 meV ($\approx$ 300 °C), then the value

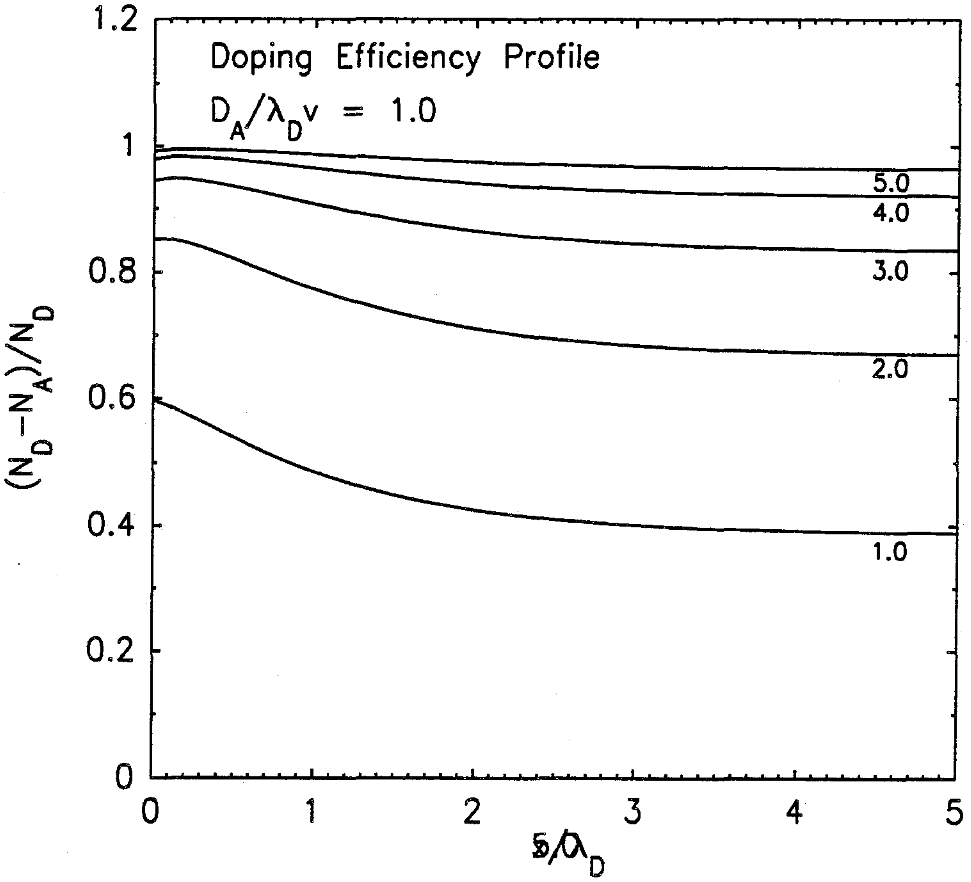

Figure 5.7: Doping profile $(N_D - N_A(x))/N_D$ is plotted as a function of the distance from the growth surface. The five curves labeled [1.0-5.0] correspond to the $\lambda_D q E_0 / k_B T$ values for five different electric field strengths. This figure corresponds to a moderate growth rate $D_A/\lambda_D v = 1.0$.

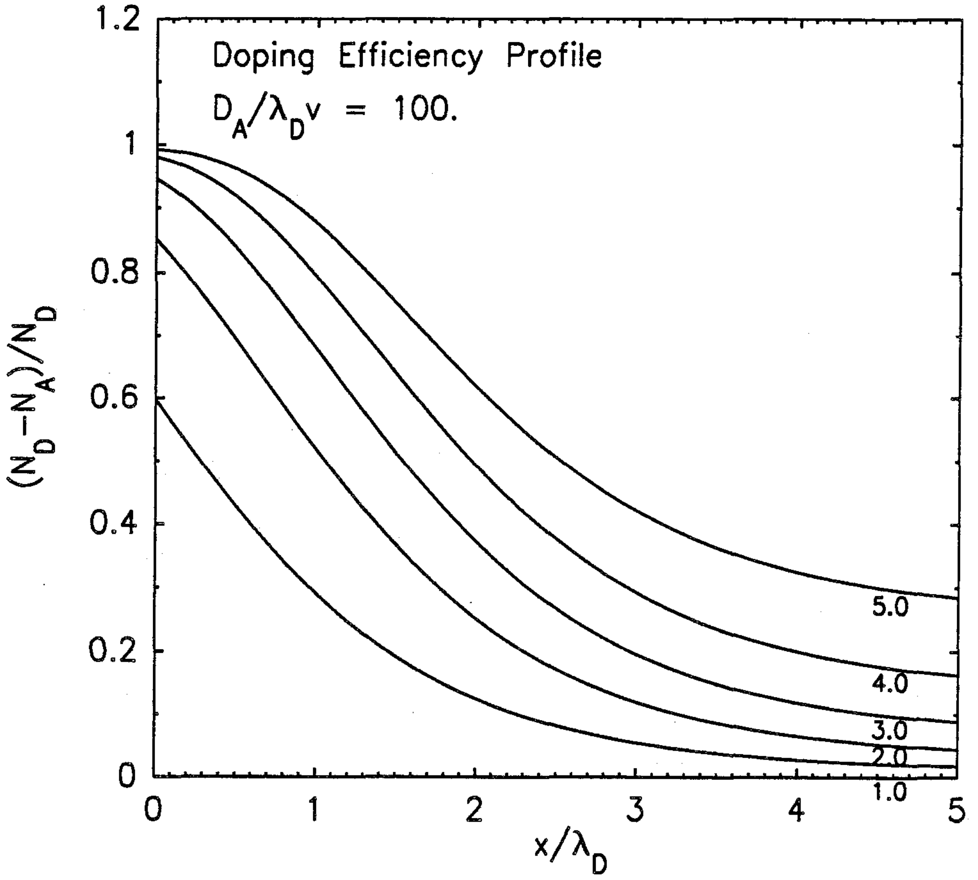

Figure 5.8: Doping profile; slow growth rates Doping profile $(N_D - N_A(x))/N_D$ is plotted as a function of the distance from the growth surface. The five curves labeled [1.0-5.0] correspond to the $\lambda_D q E_0/k_B T$ values for five different electric field strengths. This figure corresponds to a slow growth rate $D_A/\lambda_D v = 100.0$.

of this parameter is 2.0. This falls in the range where the electric field can play a substantial role, as shown in Fig. 5.5. However, the field required to produce 100 meV of band-bending within a screening length of 100 Å is about 10^5 Vcm^{-1}. Producing such a large electric field inside the semiconductor during growth would be quite difficult; however, even fields as low as 10^3 Vcm^{-1} could be employed to reduce the compensation process qualitatively.

5.4.3 Screening Length

In this section we present the results for the screening parameter s as a function of the two dimensionless parameters $D/\lambda_D v$ and $\lambda_D q E_0/k_B T$. In Equation 5.32 we defined this parameter s as the ratio between the screening length that is consistent with linear screening theory, and the classical Debye screening length. The results of Fig. 5.9 indicate that the Debye screening length is still a valid approximation for moving coordinate frames. However, deviations from the Debye result can occur for very fast growth and low electric fields, as shown in Fig. 5.9. The validity of the linear screening theory depends on the ability to neglect higher-order terms of the form $qV_0/k_B T$. However, the analysis of this chapter based on linear screening theory is quite adequate since very large electric fields are necessary to produce a situation where the linear screening approximation breaks down.

5.5 Conclusions

In this chapter, we performed theoretical calculations to show that it is possible to suppress the compensation processes in semiconductors by applying substantial electric fields during epitaxial growth. We expect that our analysis, and the proposed electric field-assisted doping technique could play an important role in the effort to overcome compensation and achieve selective doping in wide band gap II-VI

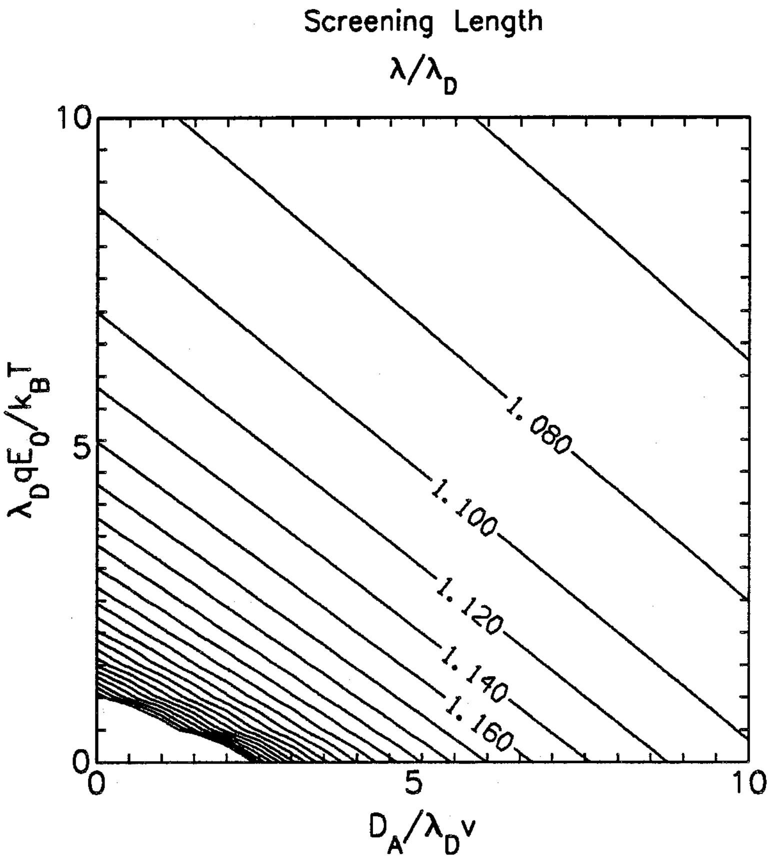

Figure 5.9: Contour plot of the screening parameter λ/λ_D that is determined self-consistently within the linearized screening approximation. The λ_D is the Debye screening length. This figure shows that for the parameter range of interest, the Debye screening model seems to be a good approximation. However, in this analysis we have ignored the nonlinear screening effects.

semiconductors.

References

[1] F. A. Kroger, in *The Chemistry of Imperfect Crystals*, North Holland, Amsterdam (1973).

[2] R. E. Halstead, *J. Phys. Chem. Solids* **22**, 109 (1965).

[3] M. R. Lorenz and B. Segall, *Phys. Lett.* **7**, 18 (1963).

[4] M. Aven and R. E. Halsted, *Phys. Rev.* **137**, 228A (1965).

[5] J. L. Pautrat, J. M. Fancou, N. Magnea, E. Molva and K. Saminadayar, *J. Cryst. Growth* **72**, 194 (1985).

[6] H. Venghaus and P. J. Dean, *Phys. Rev. B* **21**, 1596 (1980).

[7] P. J. Dean, *J. Lumin.* **21**, 75 (1979).

[8] W. M. Chen, B. Monemar, P. O. Holtz, Q. X. Zhao and H. P. Gislason, *Phys. Rev. B* **35**, 5714 (1987).

[9] P. O. Holtz, B. Monemar, H. P. Gislason and N. Magnea, *J. Lumin.* **35**, 245 (1986).

[10] N. Magnea, D. Bensahel, J. L. Pautrat, K. Saminadayar and J. C. Pfister, *Solid State Comm.* **30**, 259 (1979).

[11] J. Bittebierre and R. T. Cox, *Phys. Rev. B* **34**, 2360 (1986).

[12] J. L. Miguel, S. M. Shibli, M. C. Tamargo and B. J. Skromme, *Appl. Phys. Lett.* **53**, 2065 (1988).

[13] R. Dingle, H. L. Stormer, A. C. Gossard and W. Wiegmann, *Appl. Phys. Lett* **37**, 855 (1978).

[14] T. Yao and T. Takeda, *Appl. Phys. Lett.* **48**, 160 (1986).

[15] T. Yao, Y. Okada, S. Matsui and K. Ishida, *J. Cryst. Growth* **81**, 518 (1987).

[16] T. Yao, T. Minato and S. Maekawa, *J. Appl. Phys.* **53**, 4236 (1982).

[17] T. Yao and S. Maekawa, *J. Cryst. Growth* **53**, 423 (1981).

[18] S. Hwang, R. L. Harper, K. A. Harris, N. C. Giles, R. N. Bicknell, J. W. Cook, J. F. Schetzina, M. Chu, *J. Vac. Sci. Technol. A* **6**, 2821 (1988).

[19] N. C. Giles, R. N. Bicknell, R. L. Harper, S. Hwang, K. A. Harris, J. F. Schetzina, *J. Cryst. Growth* **86**, 348 (1988).

[20] M. Aven and B. Segall, *Phys. Rev.* **130**, 81 (1963).

[21] R. S. Title, G. Mandel, and F. F. Morehead, *Phys. Rev.* **136**, A300 (1964).

[22] R. S. Title, in *Physics and Chemistry of II-VI Compounds*, edited by M. Aven and J. S. Prener, North Holland, Amsterdam (1967).

[23] J. O. McCaldin, *J. Vac. Sci. Technol* , to be published (1990).

[24] R. Hong, and J. D. Dow, *Appl. Phys. Lett.* **54**, 2597 (1989).

[25] J. O. McCaldin, T. C. McGill and C. A. Mead, *Phys. Rev. Lett.* **36**, 56 (1976).

[26] D. J. Wolford, B. G. Streetman, W. Y. Hsu, J. D. Dow, R. J. Nelson and N. Holonyak Jr., *Phys. Rev. Lett.* **36**, 1400 (1976).

[27] D. J. Wolford, W. Y. Hsu, J. D. Dow and B. G. Streetman, *J. Lumin.* **18**, 863 (1979).

[28] P. Vogl, H. P. Hjalmarson and J. D. Dow, *J. Phys. Chem. Solids.* **44**, 365 (1983).

[29] H. P. Hjalmarson, P. Vogl, D. J. Wolford and J. D. Dow, *Phys. Rev. Lett.* **44**, 810 (1980).

[30] H. P. Hjalmarson, in *Studies in the Theory of Solids*, Thesis, University of Illinois, Urbana-Champaign (1979).

[31] D. J. Chadi and K. J. Chang, *Phys. Rev. Lett.* **61**, 873 (1988).

[32] S. Y. Ren, J. D. Dow and J. Shen, *Phys. Rev. B* **38**, 10677 (1988).

[33] S. Seto, A. Tanaka, Y. Masa, S. Dairaku, M. Kawashima,, *Appl. Phys. Lett.* **53**, 1524 (1988).

[34] S. M. Durbin, J. Han, O. Sungki, M. Kobayashi, D. R. Menke, and R. L. Gunshor, Q. Fu, N. Pelekanos, A. V. Nurmikko, D. Li, J. Gonsalves, and N. Otsuka, *Appl. Phys. Lett.* **55**, 2087 (1989).

[35] T. Yasuda, I. Mitsuishi, and H. Kukimoto, *Appl. Phys. Lett.* **52**, 57 (1987).

[36] J. Nishijawa, K. Hon, Y. Okuno and F. Sakurai, *J. Appl. Phys.* **57**, 2210 (1985).

[37] M. Aven and W. Garwacki, *J. Appl. Phys.* **38**, 2302 (1966).

[38] P. M. Morse and H. Feshbach, in *Methods of Theoretical Physics*, McGraw Hill, New York (1953).

[39] N. W. Ashcroft and N. D. Mermin, in *Solid State Physiscs*, Holt, Rinehard and Winston, Philadelphia (1976).

[40] H. H. Woodbury, in *Physics and Chemistry of II-VI Compounds*, edited by M. Aven and J. S. Prener, North Holland, Amsterdam (1967).

[41] D. Shaw, *J. Cryst. Growth* **86**, 778 (1988).